Field Effect Modulation of Ion Transport in Silicon-On-Insulator Nanopores and

Their Application as Nanoscale Coulter Counters

by

Punarvasu Joshi

A Dissertation Presented in Partial Fulfillment
of the Requirements for the Degree
Doctor of Philosophy

Approved November 2010 by the
Graduate Supervisory Committee:

Trevor J. Thornton, Co-Chair
Michael Goryll, Co-Chair
Marco Saraniti
Andreas Spanias

ARIZONA STATE UNIVERSITY

May 2011

ABSTRACT

In the last few years, significant advances in nanofabrication have allowed tailoring of structures and materials at a molecular level enabling nanofabrication with precise control of dimensions and organization at molecular length scales, a development leading to significant advances in nanoscale systems. Although, the direction of progress seems to follow the path of microelectronics, the fundamental physics in a nanoscale system changes more rapidly compared to microelectronics, as the size scale is decreased. The changes in length, area, and volume ratios due to reduction in size alter the relative influence of various physical effects determining the overall operation of a system in unexpected ways.

One such category of nanofluidic structures demonstrating unique ionic and molecular transport characteristics are nanopores. Nanopores derive their unique transport characteristics from the electrostatic interaction of nanopore surface charge with aqueous ionic solutions.

In this doctoral research cylindrical nanopores, in single and array configuration, were fabricated in silicon-on-insulator (SOI) using a combination of electron beam lithography (EBL) and reactive ion etching (RIE). The fabrication method presented is compatible with standard semiconductor foundries and allows fabrication of nanopores with desired geometries and precise dimensional control, providing near ideal and isolated physical modeling systems to study ion transport at the nanometer level.

Ion transport through nanopores was characterized by measuring ionic conductances of arrays of nanopores of various diameters for a wide range of concentration of aqueous hydrochloric acid (HCl) ionic solutions. Measured ionic conductances demonstrated two distinct regimes based on surface charge interactions at low ionic concentrations and nanopore geometry at high ionic concentrations. Field effect modulation of ion transport through nanopore arrays, in a fashion similar to semiconductor transistors, was also studied. Using ionic conductance measurements, it was shown that the concentration of ions in the nanopore volume was significantly changed when a gate voltage on nanopore arrays was applied, hence controlling their transport.

Based on the ion transport results, single nanopores were used to demonstrate their application as nanoscale particle counters by using polystyrene nanobeads, monodispersed in aqueous HCl solutions of different molarities. Effects of field effect modulation on particle transition events were also demonstrated.

To Maa and Pa.

I owe my success to you.

ACKNOWLEDGEMENTS

It is hard to say exactly when I started working on my PhD. It began somewhere when I was given a chance to work as an undergraduate student worker in Dr. Trevor J. Thornton's lab with graduate students performing myriad of strange verbs of science such as pipetting, etching and depositing. Initiated by this opportunity to work alongside graduate students, my metamorphosis into a PhD student was gradual and inconspicuous from day to day until it became an established reality, a reality which was continuously shaped and nurtured under the guidance of Dr. Trevor J. Thornton. This doctoral research is the outcome of that guided journey. Along with Dr. Thornton, Dr. Michael Goryll also played a pivotal role in helping me grow into a PhD student. This research would not have reached its fruition without the constant guidance of from Dr. Goryll and Dr. Thornton and I am thankful to them for guiding me in completion of this endeavor.

In understanding Nature's workings, research often leaves a student perplexed with questions which seem almost unsolvable. Dr. Marco Saraniti and Dr. Andreas Spanias, with their continuous presence in weekly group meetings, played an important role in breaking down those vexing questions to bite size pieces which I and my fellow graduate students could then work on. I would like to thank Dr. Saraniti and Dr. Spanias for their constant constructive input on research matters. I would also like to thank Dr. Leo Petrossian, Dr. Alex

TABLE OF CONTENT

LIST OF TABLES

LIST OF FIGURES

1. INTRODUCTION

1.1 Introduction

In the last few years, significant advances in nanofabrication technologies have led to the beginning of a new era where materials and structures are designed at a molecular level and then fabricated with control of composition and dimensions at molecular length scales. This drive to design, manipulate and build structures with dimensions in the molecular range has immensely contributed to advances in nanoscale analysis systems. Although, the direction of progress of nanoscale analysis systems or nanofluidic structures seems to follow the path of microelectronics, it differs in one important aspect from microelectronics that the fundamental physics in nanoscale analysis systems, changes more rapidly as the size scale is decreased. When a system is reduced in size the changes in length, area, and volume ratios alter, often in unexpected ways, the relative influence of various physical effects that determine the overall operation of a system. In the past, understanding of various transport processes was targeted at size scales where the continuum description of a fluid could be employed to understand the observed phenomena. Due to the confined geometries at the nanometer level as well as significant decrease in the mass and the volume of analytes and reagents used for analysis, the continuum assumption often presents an incomplete picture of the physical phenomena observed. Independent of the type of driving force, the novel attributes of nanofluidic structures ensure ionic and molecular transport

characteristics that are fundamentally different from those in larger micrometer and millimeter scale structures. One such category of nanofluidic structures demonstrating unique ionic and molecular transport characteristics are nanopores. The characteristics of ionic and molecular transport often observed in nanopores are pronounced influence of surface charge density, coupled and enhanced mass and ion transport, nanostructure size and shape, mobile phase ionic strength, large mass-to-charge ratio of ionic species in an ionic solution, ion depletion/enrichment, ion current rectification, and diminished background signals [1-21]. An important feature of these nanopores also is their high surface-to-volume ratio [4, 5, 21], leading to enhanced electrostatic interaction between ions in the bulk of the electrolyte solution filling the nanopore and charges on the inner surface of the nanopore itself. This interaction will completely dominate the transport of ions when the channel dimensions are comparable to the Debye screening length of the ionic solution [4, 5]. These myriad phenomena, point to a simple fact that the molecular characteristics can dominate the ionic and molecular transport behavior of a nanostructure. Thus, these nanopores are an ideal platform to study electrolyte transport properties on the nanometer scale [1, 3-7, 10, 12-19, 21, 24-44], to control the ion transport by modulation of the surface potential [5, 7-9, 12, 13, 16, 17, 20, 29, 31, 33, 36, 37, 39, 44-54], similar to the control mechanism present in field effect transistors.

Researchers have just started to realize the challenges and possibilities associated with nanopores, yet it is clear that the ability and understanding to achieve efficient and intelligent control of molecular and ionic transport within these nanofluidic structures will enable the construction of new devices that can address fundamental problems in molecular and ionic transport as well as open vistas for efficient and intelligent control of nanoscale analytes. Efficient and intelligent control of the nanoscale analytes implies materials and geometries which can sense size, charge, and molecular shape of the target analyte and generate signals that control transport on the basis of those characteristics. Both, artificial and biological nanopores have emerged as one of the popular choices for detection, confinement, and transport of nanoscale analytes allowing an opportunity to study nanometer level interactions which are typically lost in bulk measurement methods.

The rest of the chapter is organized as follows. Next section describes the basics of main application of nanopores as nanoscale Coulter counters. The chapter then briefly describes the application of biological nanopores and the challenges associated with them. The discussion then proceeds to artificial nanopores fabricated in a variety of substrates using various nanofabrication techniques. The chapter concludes with an overview of the work presented in this study and brief explanation of organization of the rest of the dissertation document.

1.2 Resistive Pulse Sensing

Although, there are many applications of nanofluidic structures, a promising approach which has gathered momentum among researchers is the use of nanopores for nanoscale analyte detection. For the past decade nanometer-scale pores have been investigated as sensing platforms, especially with an application towards sensing biological macromolecules. In general, two types of nanopores have been presented for application as sensing devices. The first type of nanopores used are naturally existing biological nanopores, called ion channels, such as α-Hemolysin, whereas the second type of nanopores used are artificial nanopores which have been developed using numerous conventional and non-conventional fabrication techniques and substrates. The fundamental principle employing the use of nanopores as nanoscale analyte sensors is simple. Nanopores act as Coulter counters or resistive pulse sensors when molecules are electrophoretically driven through the pore by applying an electric potential. Coulter counting or resistive pulse sensing technique was originally developed by Wallace H. Coulter of Coulter Electronics Corporation [55]. In resistive pulse sensing method a membrane consisting of a single nanopore is mounted between chambers filled with an ionic solution. An electric potential is applied across the membrane and the resultant ionic current flowing through the nanopore is recorded as a function of time. When an analyte with dimensions comparable to

4

diameter of a nanopore passes through, a momentary blockade of ionic current is observed, leading to a downward current pulse. The concentration of the target analyte in the solution is correlated with the frequency of downward spikes in the current vs. time trace and the magnitude and the duration of the downward spike becomes the electric signature of the target analyte[25-27, 32, 41, 47, 56-80]. The nanopore geometry can be tailored for the target analyte and then can be used to determine analyte size, concentration and electrophoretic mobility[25-27, 32, 41, 47, 56-80]. Figure 1.1 shows the concept of the above method.
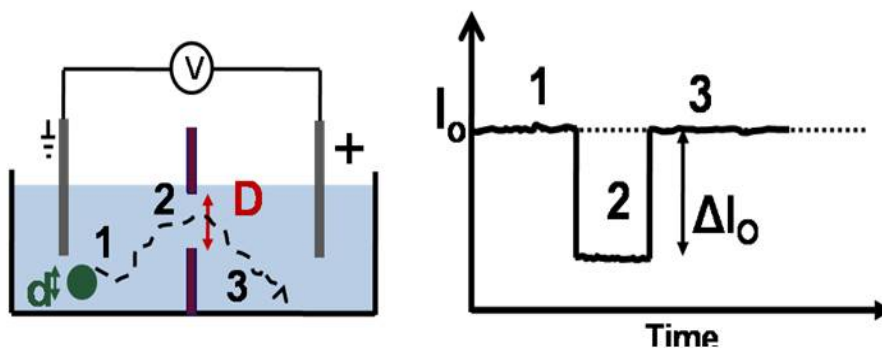
Figure 1.1 Graphical depiction of Coulter counting principle. While applying a bias across a nanopore of diameter, D the ionic current, I_o through the nanopore is measured. When an analyte of diameter, d passes through the nanopore (left pane), it results in a drop, ΔI_o in the measured ionic current (right pane).

Single most important application of nanopores has been in DNA analysis. The initial approach for DNA analysis used well-known cell membrane protein such as α-Hemolysin [56, 57, 60, 61, 75] which was later extended for use with other

membrane bound proteins of various sizes and functionalities [81-86] which is explained in the next section. Even though bulk of DNA analysis work still focuses on the use of biological nanopores, researchers have developed artificial nanopores using conventional or non-conventional fabrication techniques which have been summarized in these extensive review papers [14, 21, 79, 87-89]. Over a period of time researchers have used nanopores to discriminate between single stranded DNA (ssDNA) and double stranded DNA (dsDNA) [90-93], to distinguish between RNA and DNA molecules [75, 94], to assess nucleic acid preparation [95], and to discriminate between modified, single and poly-nucleotides [74, 96-98]. This application of this method has been expanded and it has been successfully used for detection, characterization, and size distribution of molecules, viruses, ions and biopolymers [19, 25, 26, 59-65, 69, 72, 73, 99-105].

1.3 Biological Nanopores

A major impetus for studying ionic and molecular transport at nanoscale also came in part because of important roles played by biological nanopores in many physiological processes of living organisms [106]. A cell membrane offers an impermeable barrier for any type of ionic or molecular transport in and out of a cell. The transport of ions and molecules is then facilitated by different types of membrane proteins, called ion channels, embedded in the cell membrane and spanning across the thickness of the cell membrane (~4nm), employing myriad of

transfer mechanisms such as facilitated diffusion, active transport and concentration gradients. Transport of ions and neutral molecules through ion channels also forms the backbone of intracellular communication [106]. The process of ionic and molecular transport through the membrane proteins is highly controlled and selective because biological ion channels are selective for only certain type of ions. Often, opening and closing of ion channels, called gating behavior, occurs in response to a stimulus such as deformations in the cell membrane, presence of a ligand or a specific signaling molecule, or changes in voltage potential, temperature or pressure across the cellular membrane. In the open or 'on' sate of an ion channel, the ions are allowed to pass through the channel and in closed or 'off' state, ion transport is blocked [106]. An extensive characterization of these transmembrane proteins and understanding of their respective transfer and gating mechanisms is a prolific research field [106].

The dimensions and the geometry of ion channels make them suitable candidates for nanometer scale resistive pulse sensing applications. Initial attempts to use biological nanopores for nanoscale analyte detection were made with α-Hemolysin, a single 2nm diameter transmembrane protein toxin from the bacterial species Staphylococcus aureus, inserted in a lipid bilayer [90, 94]. Kasionowicz *et al.* [90] found that α-Hemolysin pore allows ionic conduction at higher ionic strength solution and neutral pH. In addition to this, it was found that α-Hemolysin is also capable of passing steady current in a measureable range

ensuring low level of background noise, a benefit over other membrane ion channels which exhibit fluctuating current levels as a result of high sensitivity and spontaneous gating. In order to produce a nanopore, α-Hemolysin subunits are introduced into a buffered ionic solution which is in contact with a lipid bilayer spanned over two solution filled compartments. The head of the mushroom shaped α-Hemolysin nanopore is referred to as the *cis* side and the stem as the *trans* side. The lipid bilayer in which the α-Hemolysin subunits self insert also affect its operation as an ion channel. Such a setup is often used for single channel recording of ionic current and has been incorporated onto a silicon chip for miniaturization [107-109]. In the work reported, Kasianowicz *et al.* [90] were able to observe ionic current changes when DNA passed through the pore. They also concluded from the results observed that the duration of drop in current was proportional to the length of the passing DNA strand. Meller *et al.* [75] used α-Hemolysin to distinguish between purines and pyrimidines. Six polymers with the same lengths but different sequences were measured and the results were statistically analyzed. Since then α-Hemolysin has been explored and tailored to specific applications [59], due to its ideal pore size, low levels of noise in the electrical measurements and fairly well established preparation protocols.

Apart from α-Hemolysin other membrane bound proteins with suitable structure and properties have also been explored. Such proteins have been isolated and reconsitituted in a lipid bilayer for DNA analysis based on DNA

8

translocation. One such protein channel which has been used is the voltage dependent mitochondrial ion channel which is located in mitochondrial outer membrane [83, 84, 92]. Similarly, bacterial protein pores have also been studied in addition to α-Hemolysin [85]. OmpF porins from the outer membrane of *E. Coli* have also been employed in transport studies [82, 84, 110]. Another application of biological pores for analyte detection has used gramicidin pores [111]. Primary reasons to explore proteins other than α-Hemolysin are exploration of biological pores of varying sizes, ease of preparation procedures and structural modification as well as possibility of simpler structure, robustness, and better reproducibility [111].

Although, successfully employed in nanoscale resistive pulse sensing, many of the transport properties of biological ion channels are not well understood. Investigation of these properties becomes a challenge because of inherent shortcomings of biological systems as lipid bilayer embedded protein nanopores have limitations due to size, variation, and most importantly stability. Lipid bilayer membranes are fragile in nature and protein nanopores are metastable. In addition to this, biological nanopores have fixed pore diameter, allow a narrow range of safe electrical operation, and are susceptible to thermal, chemical, and physical variations in the environment leading to restrictions on experimentation possibilities [69, 112, 113]. Biological nanopores, due to their requirement of operating at a specific solution pH, are not suitable to study ionic and molecular

transport at wider range of solution pH. The complexity of ion selective transport coupled with the susceptibility of ion channels to the external factors presents a challenge to a thorough understanding and control of ionic and molecular transport. Thus, the innate shortcomings of biological nanopores coupled with the need to understand molecular and ionic transport in extensive detail force researchers to develop options which can serve as isolated and near ideal systems.

1.4 Artificial Nanopores

In these challenges lies the opportunity for use of artificial nanopores. Fabricating artificial nanopores mimicking the ionic and molecular transport properties of biological ion channels have the potential to provide a better understanding of the physical and chemical principles of operation of biological ion channel themselves. Move towards replacing biological nanopores with artificial nanopores to study ionic and molecular transport offers immense benefits. Artificial nanopores offer ease of fabrication, precise control of geometry, are chemically, mechanically, electrically and thermally robust and stable, and can be integrated with electronic circuits. Due to the advantages listed above artificial nanopores are ideal isolated physical modeling systems to understand the complexities of ionic transport at nanometer scale. Artificial nanopores also allow tailoring the nanopore surface chemistry for different applications thereby giving versatility of use. These benefits make solid state

nanopores suitable candidates for extensive ionic and molecular transport studies [4, 21-23, 25, 26, 65, 66, 69, 79, 89, 100, 104, 114-118].

Seeing the emerging opportunities researchers are coming up with newer ways and substrates to fabricate nanopores. Nanopores have been fabricated using polyimide thin films [119, 120], polystyrene [64, 121], carbon nanotubes [70, 72, 73, 122], silicon-on-insulator [19, 22, 23, 25, 26, 101-103, 115], glass capillaries [123], PDMS [80, 105], silicon nitride [35, 65, 71, 99, 100, 116, 124-126] , and graphene [41, 76, 127].

One of the prominent methods of fabricating nanopores is the use of ion beam milling process. A beam of massive ions with energies in several thousand electron volts (eV) is directed at the surface of the material under use causing nanometer scale atomic rearrangements. When a high energy beam of ions is focused on the surface of the material being used, atoms coming under the impact of the high energy ions are knocked off from the surface leading to formation of a nanometer scale aperture. This process was employed by Li *et al.* [99, 125] on a silicon nitride (Si_3N_4) membrane with a flat surface on one side and a bowl shaped cavity on the other. The flat surface was bombarded with high energy argon (Ar) ion beams removing material from the flat surface and creating a nanometer scale aperture in the process. By using a feedback-controlled ion beam system, the researchers could stop the ion beam as soon as breakthrough was achieved, leading to a nanopore of 1.8 nm diameter [99, 125, 126].   In another

11

innovative application of ion beam, the ion beam can be used to stimulate lateral transport of matter which can then be used shrink pre fabricated nanopores in a given substrate [65, 100, 126, 128]. Researchers have reported sample temperature, ion beam parameters, surface electric field, and geometry of the pore wall as some important parameters for shrinking of a pre fabricated nanopore using this method [65, 91, 100, 126, 128-130]. In an another approach, Chen *et al.* [27, 131] suggested using atomic layer deposition (ALD) for fine tuning the sizes of nanopore fabricated using ion beam sculpting [131]. Vapor phase atomic layer deposition (ALD) provides a uniform coating to all exposed surfaces [49, 131-133]. Since, the layer is deposited only inside the nanopore, ALD allows to maintain the initial geometry of the pore and only reducing nanopore diameter. The uniformity of ALD process allows the side wall lining of nanopore with atomic precision, leading to a reduction of nanopore diameter to desired dimension. Depending on the choice of material used for atomic layer deposition, this method can also be used for tailoring the surface properties of a nanopore [49, 131-133].

A similar process to fabricate nanopores uses fine tuning of the nanopore substrate using an electron beam. The high intensity and high energy electron beam is typically produced by transmission electron microscope (TEM) or field emission scanning electron microscope (FESEM). Electron beam lithography and standard cleanroom fabrication steps such as reactive ion etching, chemical vapor

deposition and wet etching are used to prepare the substrates [69, 102, 103, 114, 116, 124]. The method of fine tuning of nanopore diameter by using electron beam was pioneered by Storm *et al.* [102, 103] to shrink nanopores fabricated in silicon dioxide (SiO_2) membrane. Since then, it has become one of the most used solid state nanopore fabrication method. Storm *et al* .[102, 103] used silicon-on-insulator (SOI) wafers with top single-crystal silicon layer being 340 nm thick as a starting material to fabricate free standing silicon membranes. Thermal oxidation of the SOI wafers produced a 40nm thick SiO_2 masking layer on either side of the membrane. A large aperture is etched in the handle silicon wafer using the buried oxide layer as the etch stop layer. Then using a combination of electron beam lithography and reactive ion etching, square holes greater than 500 nm were etched in the top SiO_2 masking layer; subsequently pyramid shaped holes were etched in the top single-crystal silicon layer using wet potassium hydroxide (KOH) chemical anisotropic etch. KOH etches silicon faster along the <100> lattice plane compared to <111> lattice plane leading to truncated nanopores. The buried oxide separating the top single crystal silicon layer and the bottom handle silicon layer is the wet etched using hydrofluoric acid giving a thin silicon membrane with nanopore. The wafer is then thermally oxidized again to form a SiO_2 layer. Storm *et al.* [102, 103] used a commercial transmission electron microscope (TEM) to fine tune the size of pores at nanometer precision. The high energy, high electron intensity distorts the material surface thereby changing the

nanopore dimensions of the silicon dioxide nanopore in a controlled fashion. With the optimum electron beam intensity and pore diameter, nanopores start to shrink due to the lateral flow of the material. This whole process can be done in real time by observing the nanopore diameter change using the imaging mechanism of the microscope and can be switched off as soon as the desired diameter is reached, letting the material to quench off and retain its shape [103]. A similar strategy independently was used by researchers Heng *et al.*, Keyser *et al.,* and Ho *et al.* [35, 69, 71, 114, 116-118, 124, 134] to fabricate nanopores in ultra-thin membranes. Heng *et al.* [69, 114, 116, 124] employed a narrowly focused high energy electron beam from a transmission electron microscope to fabricate 1nm diameter nanopores with sub-nanometer precision in metal-oxide-semiconductor (MOS)-compatible membranes. Ho *et al.* [35, 71, 134] with a combination of standard nanofabrication techniques and electron beam fine tuning were able to fabricate a single nanopore in free-standing Si, SiO_2 and Si_3N_4 membranes. Similarly, Keyser *et al.* [117, 118] fabricated a 4nm diameter single nanopore in low-stress silicon nitride membrane. Recently, TEM electron beam was also used to fabricate nanopores in graphene [41, 76, 127]. In a minor variation of the electron beam fine tuning, Chang *et al.* [25, 26, 115] used a field emission scanning electron microscope (FESEM) to shrink a nanopore.

Another method of fabricating nanopores which is as prevalent as ion beam sculpting or electron beam tuning is the ion track-etch method. In order to

fabricate nanopores using ion track etching in polymer membranes, a polystyrene or polyimide membrane is first bombarded with a beam of high energy particles (>1MeV/ nucleon) from a nuclear reactor or a cyclotron. Every ion that penetrates the membrane creates a linear damage track that spans the entire thickness of the membrane, which is often around 5-10μm. The damage tracks were then controllably wet etched or electrochemically etched. The exposure time to the beam determines the number of latent damage tracks formed in the membrane, corresponding to the pore density, after chemical etching of the membrane. The nanopores created using this method are conical in geometry and are created in a polymer substrate [62-64, 68, 119, 121, 135, 136]. Important parameters such as size and axial uniformity of a pore can be controlled by manipulating the concentration of etchant, temperature and the duration of etching.

Nanopores were also fabricated in non-conventional methods and substrates. Saleh *et al.* [105] fabricated nanopores using micromolding techniques, a method fundamentally different from solid state nanopore fabrication. Standard cleanroom fabrication techniques were used to create a negative master of the pore and reservoirs which was subsequently cast into a poly(dimethylsiloxane) PDMS slab producing nanopore 3μm in length and 200nm in diameter. A similar method was also used by Sen *et al.* [80] to fabricate 200-500nm diameter nanopores in PDMS. On the other hand, Schmid *et al.* [137] have reported fabricating a nanopore with a diameter as small as 80nm in PDMS. Carbon

nanotubes were also used to fabricate nanopores in a fabrication procedure developed by Sun *et al.* [122] [70, 72, 73]. Carbon nanotubes are fabricated by stretching a multi-wall carbon nanotube and gluing it to a TEM grid using epoxy. The TEM grid and the multi-wall carbon nanotube are then encased in a two component epoxy, resulting in a polymer block which is then microtomed into thin membranes which are then immobilized on silicon support structure for measurements. The membrane sheets often end up with a thickness of 0.6-1.0μm. Carbon nanotubes (CNTs) offer benefit of providing smooth surface geometry. As reported by Henriquez *et al.* [70] a 400μm long CNT can provide with a substantial number of identical nanopore devices as they all come from a single polymer block. Another approach towards fabrication of nanopores by Zhang *et al.* [123] used glass capillaries. Glass nanopore is fabricated by sealing an atomically sharp platinum wire in a glass capillary, polishing the capillary terminal until a nanometer wide platinum disk is exposed. The platinum is then electrochemically etched away to produce a truncated cone shaped nanopore in glass. The platinum disk at the bottom of the pore serves as an electrode [123].

The nanopore fabrication methods and substrates presented above outline great research efforts. Unfortunately, these methods do suffer from serious drawbacks. Most of the processes outlined above are capable of producing nanopore with diameters as small as 1nm, all the processes suffer from a serious drawback in terms of high throughput mass fabrication of nanopores. Methods

16

employing electron beam, ion beam, and carbon nanotubes are tedious and time consuming in nature and necessitate the presence of skilled technician for fabrication of nanopores and therefore cannot be automated. The problem compounds when nanopores arrays are required for an application. Polyimide, Polystyrene, PDMS, and carbon nanotube substrates do not allow on chip integration of detection circuitry. Also, these substrates do not offer any capability for precise positioning of a nanopore on a substrate.

1.5 Summary of Work

The conceptual framework behind this doctoral research work is (i) to fabricate single and an array of nanopores of varying diameters in silicon-on-insulator (SOI) substrate using standard microfabrication techniques, (ii) characterize and understand ionic transport through the SOI nanopores as a function of ionic solution concentration to shed a light on the fundamental physics occurring at the nanometer scale due solid/ ionic solution interaction, (iii) to explore the possibility of field effect modulation of ionic transport through the nanopore and (iv) to assess the feasibility of application of nanopores as a nanoscale Coulter counters.

Chapter 2 presents in detail the microfabrication process capable of reliably producing single as well as an array of nanopores of cylindrical geometry with silicon dioxide surface on silicon-on-insulator substrate.

17

Chapter 3 describes the methodology, the measurement set up and the experimental protocol used to study ion transport through nanopores.

Chapter 4 presents the results of ion transport experiments performed on nanopores. This chapter also discusses the results of field effect modulation of ion transport.

Chapter 5 presents the results of resistive pulse sensing experiment demonstrating application of nanopores as nanoscale Coulter counters.

2. FABRICATION PROCESS FLOW OF SILICON-ON-INSULATOR

NANOPORES

2.1 Substrates and Techniques for the Fabrication of Nanopores

Nanopores derive their unique functionality not only due to the new physics at the nanoscale, but also because of the technological advances in nanoscale fabrication that allow precise control over geometry and dimensions of the nanopores. As modern microfabrication techniques are advanced and optimized, pores can be fabricated to have dimensions, composition and surface properties tailored to suit individual experiments. Nanopores have been fabricated using polyimide thin films [119, 120], polystyrene [64, 121], carbon nanotubes [70, 72, 73, 122], silicon-on-insulator [19, 22, 23, 25, 26, 101-103, 115], glass capillaries [123], PDMS [80, 105], silicon nitride [35, 65, 71, 99, 100, 116, 124-126] , and graphene [41, 76, 127].

Nanopores were fabricated in polyimide [119, 120] and polystyrene [64, 121], substrates by using ion track etch methods. The ion track etch method is a fabrication process which uses bombardment of accelerated uranium ions through either a polyimide or polystyrene substrate. The accelerated uranium ions leave damage tracks in the polymer substrate which are then controllably wet etched to provide nanopores. Although, the process produces pores as small as 2nm, it is presents major challenges in terms of mass fabrication, integration of microfluidics for solution delivery, integration of on chip electronic circuitry and

19

diameter and position control of the nanopores on the substrate. The use of uranium ions in the fabrication process discourages mass fabrication in a standard semiconductor cleanroom. Since the high energy uranium ions are bombarded on the substrate, the process offers no control on the positioning of nanopores on the substrate, thus making it unusable for ordered nanopore array fabrication for application towards high throughput Coulter counters. Lastly, the polymer substrates rule out the possibility of field effect manipulation of ion transport through the nanopores.

Unlike polymer substrates, silicon-on-insulator and silicon nitride substrates allow the fabrication of nanopores in a standard cleanroom environment. Silicon-on-insulator substrates are engineered multilayered substrates having a layer of an insulator, generally silicon dioxide, sandwiched between a top layer of monocrystalline silicon and a handle silicon wafer [138]. In one approach for the fabrication of nanopores on silicon-on-insulator substrates, the handle silicon wafer is wet etched along specific crystal planes, stopping at the buried oxide layer, leading to a large opening in the handle silicon wafer [102, 103]. The top silicon layer is patterned with an opening of the order of 500nm, which also is wet etched using potassium hydroxide (KOH) along the lattice planes of silicon, providing a nanopore. The nanopore is then shrunk to the desired diameter by growing a thin layer of silicon dioxide. The pores can be further reduced after oxidation by using an electron beam from a transmission electron microscope

20

(TEM) or field emission scanning electron microscope (FESEM) to cause "reflow" of the silicon dioxide at the nanometer level [25, 26, 102, 103, 115]. Although, the fabrication process and the silicon-on-insulator substrate are compatible with the standard cleanroom techniques, and allow the possibility of integration of on chip electronic circuitry and microfluidics, the challenge lies in fabricating an array of the nanopores. The use of transmission and field emission electron microscopes renders this process unusable for mass fabrication as well as fabrication of an array of nanopores, due to the requirement of a skilled personnel and amount of time involved in fabricating a nanopore. In addition to this, the use of a wet etch in the process often leads to loss of process and dimensional control.

Silicon nitride substrates are also used in a similar fabrication procedure to fabricate nanopores. The nanopores in silicon nitride were made using a process called focused ion beam (FIB) milling [35, 65, 71, 99, 100, 116, 124-126] . In focused ion beam milling, a heated liquid metal ion source is used to ionize metal and cause a field emission of ions. The ions are then accelerated to an energy of 5-50keV and focused on the substrate using electromagnetic lenses. The focused ion beam then allows local milling of the substrate leading to fabrication of nanopores. The nanopore size is shrunk to the desired diameter by the use of transmission electron microscope. As with the silicon-on-insulator substrate nanopores, silicon nitride also poses challenges in reliable fabrication of an ordered nanopore array. Silicon nitride thin films are prone to mechanical

stresses and pose a serious concern for the device robustness. Focused ion beam milling of nanopores is a slow process and creates atomic level debris which make it unfit for fabrication of ordered high packing density nanopore arrays.

The fabrication process flow developed in this research and presented in this chapter addresses all the drawbacks of the above substrates. The fabrication of nanopores in silicon-on-insulator using electron beam lithography and dry etching processes allows fabrication of precise, reliable definition of nanopores as well as an ordered array of nanopores. The process flow is compatible with standard cleanroom facilities for a high throughput fabrication of single as well as an array of nanopores. The process flow also permits precise dimensional as well as process control.

2.2 Design Parameters

This section describes the main design parameters which were taken into accountprior to the fabrication of nanopores. These parameters were chosen in order to explore the application of nanopores towards a study of field effect modulation of ion transport through the nanopores and application of nanopores as nanoscale Coulter counters.

2.2.1 Diameter of Nanopores

The most important parameter for the studies of field effect modulation of ion transport as well as nanoscale particle translocation is the diameter of the nanopore. When a solid surface comes in contact with an ionic solution, it influences the distribution of nearby ions in the solution. Ions of charge opposite to that of surface, called *counterions*, are attracted to the interface in order to screen the planar layer of charge on the surface of the solid. This results in high local concentration of counterions next to the interface. The ions of the same charge as the surface, called *coions* are repelled from the interface, leading to a low local concentration of coions. This resulting arrangement of charges on the solid/solution interface is known as the *electric double layer (EDL)* [139]. The overall width of the EDL is typically described by a characteristic length scale called the Debye length, which ranges from a few nanometers for high ionic concentration electrolyte solutions to a few hundreds of nanometers for low ionic concentration electrolyte solutions [139]. When the nanopore diameter falls in this range (1-300nm), the electric double layer extends across the entire pore diameter where counterions dominate and coions are excluded from the nanopores. This overlap of electric double layers, critically dependent on the aperture diameter, creates a unique unipolar environment which not only affects the ion transport through the aperture but also opens up the possibility of ion transport manipulation by applying a voltage bias to the substrate [4, 5, 14].

Similarly, in the detection of nanoscale particles translocating through the nanopore, the nanopore diameter plays an important role. When a nanoparticle passes through a nanopore, a decrease in the magnitude of ionic current is observed because part of the liquid volume that carries the ionic current is occupied by the nanoparticle. The drop in the magnitude of the ionic current is given by the following equation [70]:

$$\Delta I = I_{Baseline} * (d^3 / L * D^2) \tag{2.1}$$

Where, d is the spherical particle diameter, D is the pore diameter, L is the length of the nanopore and $I_{Baseline}$ is the ionic current measured through the nanopore for a given applied voltage and electrolyte solution. The smaller the pore diameter, that larger the ΔI for an observed particle. In this manner, nanopores can be designed to have different diameters to detect specific individual analytes of interest.

2.2.2   Silicon-on-insulator as a Substrate of Choice

Silicon-on-insulator (SOI) wafers are precisely engineered multilayer semiconductor/ dielectric structures. SOI substrates consist of a thin layer of a single crystalline Si separated by a layer of SiO_2 from the bulk substrate.The SOI substrate material and nanopore device geometry was decided upon based on two primary considerations. The first one being the field effect modulation of ion transport through the nanopores which requires fabrication of nanopore arrays to

24

enhance the signal to noise ratio and the second being the study of nanoscale particle translocation through nanopores which requires fabrication of single nanopores on the device chip. SOI substrates are chosen for fabrication of nanopores because of multiple advantages offered in the fabrication process, as well as for conductance measurements due to the presence of the buried oxide (BOX) layer. During fabrication, the buried oxide plays the critical role of etch stop layer due to high etch selectivity between silicon and silicon dioxide. The presence of the thick insulating BOX layer provides a high DC isolation resistance between the silicon device layer containing the nanopores and the handle wafer, thereby significantly reducing current leakage paths. The sandwiched BOX layer also lowers the overall capacitance of the chip, which leads to reduced noise floor in the conductance measurement. The SOI substrate also offers the benefit of being compatible with standard cleanroom fabrication processes which allow for mass fabrication of nanopores. Choice of SOI substrate also offers the critical benefit of directly applying the biasing voltage to the nanopore chip for field effect modulation of ion transport through the nanopores. Another benefit of SOI substrates is that the top silicon layer can be thermally oxidized to give an atomically smooth and well characterized, hydrophilic layer of SiO$_2$, making nanopores suitable for biological applications as well.

The Smart Cut ^{TM} process is Soitec's proprietary technology, used to manufacture the company's UNIBOND SOI wafers by wafer bonding and ion

implantation induced weakening or splitting. A 'seed' wafer, from which a layer of Si will be removed, is oxidized to a desired thickness. This oxide will become the buried oxide after wafer bonding. The next step is hydrogen ion implantation through the oxide and into Si. After implantation, the seed wafer and the handle wafer are carefully cleaned in order to eliminate any particle and surface contaminants and to make both surfaces hydrophilic. Wafer pairs are aligned and contacted so that the fusion wave can propagate across the entire interface bonding the two wafers together. A batch of bonded wafer pairs is loaded into a furnace and heated to a temperature of 400-600°C, at which point the wafers split along the hydrogen implanted plane. A final CMP touch polish brings the surface roughness of a SOI wafer to the same level as standard bulk Si wafers [138].

The approach described above makes it possible to reuse the seed wafer several times, thus reducing the final cost of a SOI wafer. It is the premium seed wafer that defines the quality of the SOI film, whereas the handle wafer only serves as a mechanical support and can have lower quality. Defining film thickness by implantation energy leads to a much better thickness control than is possible with either mechanical or chemical thinning [138].

The thickness of the silicon film and/or buried oxide can be adjusted in the Smart Cut™ process by tuning the implant energy and oxidation time in a wide range. The thickness of the silicon in current applications typically runs from

about 5 nm to 1.5 µm. The thickness of the silicon dioxide in current applications runs from about 5 nm to 5 µm [138].

2.3 Nanopore Fabrication Main Processes

The nanopores fabricated for the research described in this dissertation used a two mask, 12 step process and standard cleanroom processes. The two main processes which are instrumental in the successful fabrication of nanopores are patterning of nanopores using electron beam lithography and etching of the SOI substrate using reactive ion etching and deep reactive ion etching. These two important processes form the basis of nanopore fabrication. The following section briefly provides an overview of electron beam lithography and reactive ion etching and proceeds to the nanopore fabrication process flow in detail.

2.3.1   Etching Processes

Etching in nanofabrication implies pattern transfer by chemical/physical removal of a material from a substrate, often in a pattern defined by a protective mask layer. There are two types of etching process employed, called dry etching and wet etching, in order to etch different materials and layers. In wet etching, the sample is immersed in a liquid etchant. The ensuing chemical reaction dissolves the material from the substrate isotropically, keeping the mask layer intact. Wet etching is a faster and low cost etching process predominantly employed for bulk

material removal, cleaning, and removing surface damage. The major factors which control the rate of etching are etchant composition, temperature and crystallographic orientation of the substrate or the material to be removed. Although, useful for bulk material etching, wet etching often uses toxic chemicals leading to disposal issues, excessive particle contamination, undercutting and broadening of photoresist features, and to poor control of the process as well as dimensions of the device features. In addition to the above factors, a wet etching process is unsuitable for fabrication at the sub-micron level because of the role of surface tension in preventing the etchant from reaching between the photoresist features.

In the light of above listed issues with wet etching, dry etching, has evolved as the process of choice for precision pattern transfer. Dry etching is a collection of processes by which a solid surface is etched in the gas or vapor phase, physically by ion bombardment, chemically by chemical species at the solid surface, or by combined physical and chemical mechanisms. In dry etching, a combination of high energy electric and magnetic fields disintegrate an appropriate gas etchant to form energetic ions, neutrals, photons, electrons and highly reactive radicals. The solid surface to be etched is exposed to these reactive species leading to physical, chemical and physical/chemical etching of the surface. Reactive ion etching (RIE) and deep reactive ion etching (DRIE) are the processes from the family of dry etching processes used to fabricate nanopores.

Typically in reactive ion etching and deep reactive ion etching, chemical reactions between the solid surface and ion bombardment combine to etch the silicon surface. Reactive ion etching, although slow in etch rates compared to wet etching, provides numerous other benefits suitable for nanofabrication such as, critical dimensional and process control, fewer disposal problems, less undercutting and broadening of photoresist features, better selectivity of the etching between mask and the surface, and the choice of isotropic or anisotropic profiles.

Deep reactive ion etching (DRIE) was developed to address the issues faced in reactive ion etching such as, low etch rates, inability to maintain high aspect ratios and complete etching of masking layers during long etches. In deep reactive ion etching, a high density, low pressure and low energy plasma is generated by coupling ion producing electrons to the magnetic field arising from the RF voltage at 13.556MHz. In order to prevent creation of high energy electrons through capacitive coupling, the plasma is shielded from the electric field of the RF voltage. Using deep reactive ion etching, it is possible to attain etch rates in the range of 4-8μm/min [140] and high aspect ratio structures, such as a silicon to photoresist etch selectivity of 50:1. Deep reactive ion etching employs a specific technique, especially developed for obtaining vertical sidewalls, called the 'Bosch process,' which alternates between etch and passivation cycles to produce vertical sidewalls. The process starts with dry

etching silicon using sulfur hexafluoride (SF_6) as the source gas. The resulting high density plasma is generated above the substrate and is rich with fluorine (F) radicals which then isotropically etch the silicon surface. To assist the etching, a phase locked bias at 13.56MHz is applied to the platen holding the substrate, directing the ions towards the surface of the sample. In the second step, a passivation layer of polytetrafluoroethylene (PTFE, Teflon) using C_4F_8 is deposited. Deposition of PTFE using plasma leads to conformal coating of the silicon surface [141, 142]. The passivation layer at the bottom of the etched silicon is immediately destroyed by the downward ion bombardment in the next cycle of etching using sulfur hexafluoride (SF_6), but the sidewall coating of PTFE remains intact and prevents undercutting of the mask by protecting it from the ionic species and allows vertical sidewalls.

The nanopores used for this work were fabricated using an Oxford Instruments Plasmalab 80+ reactive ion etching tool and a Surface Technology Systems (STS) Advanced General Etch (ASE) and Advanced Silicon Etch (ASE) tools available in the Center for Solid State Electronics Research (CSSER) class 100 cleanroom at Arizona State University. The complete fabrication process flow is discussed later in the chapter.

2.3.2 Electron Beam Lithography

Electron beam lithography is a high resolution patterning technique which focuses high energy (10 to 100keV) electrons into a narrow beam in order to

expose electron sensitive resists. Electron beam lithography allows precise control of the energy and dose of electrons delivered to the resist coated wafers. Since the electron beam employed is deflected and modulated with ease using a series of electrostatic and magnetic fields, this process eliminates the need for a physical mask set and also lowers defect densities. Another advantage offered by electron beam lithography is that it can register accurately over small areas of a wafer allowing the precise definition of nanopores.

An important challenge in using electron beam lithography is that the resolution of the focused electron beam in e-beam writers is affected by the scattering of the electron beam inside the resist and substrate and also due to the backscattering of electrons from the substrate. This often leads to exposing of the substrate over a greater area than the beam spot size. Proximity effects such as partially exposing the resist far beyond the point of impact are also created by the scattering electrons.

The JBX-6000FS/E electron beam lithography system in the Center for Solid State Electronics Research (CSSER) is equipped with a thermal field emission electron gun with ZrO/W emitter, and was used to pattern nanopores using PMMA as the electron beam resist. It is used for research that requires ultra fine pattern exposure with resolution down to 10nm routinely achieved in PMMA resist. PMMA electron beam resist was used to pattern the nanopores due to its

high resolution capability; moderate glass transition temperature (114°C) and high dry etch resistance [143].

2.4 Nanopore Fabrication Process Flow

The fabrication process involves two mask sets and 12 steps overall, not counting the cleaning steps, to fabricate a 4 inch wafer with nanopore devices. The steps remain the same for fabrication of single nanopores, as well as arrays of nanopores, with only a minor change in one of the steps of the process. All the steps use standard cleanroom fabrication processes and were completed in a class 100 cleanroom at the ASU Center for Solid State Electronics Research (CSSER). In a nutshell, the fabrication process commences by defining the nanopores using electron beam lithography and then etching the nanopores using reactive ion etching in the top silicon layer, also called the device layer or top side, of a SOI wafer. The process then proceeds to the handle silicon wafer, or backside of a SOI wafer, to fabricate a 100μm pore in the handle wafer, directly under the nanopore etched in the top layer, using deep reactive ion etching. The 100 μm diameter opening in the handle wafer meets the nanopore in the top silicon layer at the buried oxide (BOX) layer. The buried oxide layer is then wet etched using buffered oxide etchant (BOE) and in the final step, the top layer is oxidized using thermal oxidation to shrink the nanopores to the desired diameter. Nanopores were fabricated on a double sided polished 100mm diameter p-type SOI

UNIBOND wafer purchased from Soitec, Bernin, France, with a 340nm top silicon layer, 450 μm thick p-type handle wafer and a 1μm buried oxide layer sandwiched between the two silicon layers (Figure 2.1.A). Prior to electron beam patterning of the nanopores, a 60nm thick layer of silicon dioxide is thermally grown in a dry oxygen atmosphere at 1000°C for 60 minutes and is used as the mask layer in order to etch the nanopores in the top silicon layer. SiO_2 is used as a mask layer because it is easy to grow and etches ten times more slowly than the silicon (Figure 2.1.B).

The next step in the fabrication process flow is electron beam patterning of the nanopores on the topside SiO_2 surface. The wafer is cleaned after the thermal oxidation and the topside is spin coated with 3% polymethyl methacrylate (PMMA) in Anisole® (methoxybenzene) at 5000 RPM. This provides a nominal thickness of 100nm of PMMA on the wafer (Figure 2.1.C). PMMA electron beam resist is used to pattern the nanopores due to its high resolution capability; moderate glass transition temperature (114°C) and most importantly high dry etch resistance, a critical factor as the PMMA acts as the mask layer during the reactive ion etching of the nanopores in the top silicon dioxide layer [143]. After the spin coating of PMMA, the wafer is baked at 175°C for 15 minutes on a level hotplate to ensure uniform solvent evaporation. The wafer was then ready for electron beam patterning of either single or an array of nanopores using the JEOL JBX-6000FS/E electron beam lithography system. Along with the patterning of

33

nanopores in the top silicon layer, the alignment markers for the backside processing are also patterned. The alignment markers serve as the reference point for backside lithography to etch the 100μm pore in the handle wafer. The area dose used for patterning was 460μC·cm^{-2} (Figure 2.1.D).

After the electron beam patterning session, the wafer is developed in a proprietary developer solution comprising of eleven parts of methyl isobutyl ketone: isopropanol (1:3), ten parts 2-ethoxyethanol: methanol (3:7) and one part methyl ethyl ketone:ethanol (26.5:73.5). The wafer was developed in the above mentioned developer for 20 seconds at 23°C, rinsed with isopropanol and dried using nitrogen gas. This completes the electron beam patterning of the nanopores in the 100nm thick PMMA electron beam resist. The next step is the transfer of the defined nanopore patterns from the PMMA to the SiO_2 hard mask and then to the top silicon layer of the SOI wafer using reactive ion etching.

An Oxford Instruments Plasmalab 80+ reactive ion etching system was used with CHF_3:Ar etch chemistry to dry etch the SiO_2 layer using PMMA as the mask layer. A CHF_3:Ar chemistry provided favorable etch rates for oxide and PMMA. In order to make sure that the pattern is completely transferred from the PMMA to the SiO_2, the top side was over etched for a total 20 minute etch run time (Figure 2.1.E). An STS AGE etch tool was used to transfer the pattern from the SiO_2 layer to the topside silicon layer using 500W of coil power and 50W of platen power to direct the plasma towards the wafer. In order to achieve

anisotropic profiles, chlorine (Cl) etch chemistry was explored and used instead of fluorine (F) as chlorine is inert and prevents lateral etching of silicon thereby giving vertical sidewalls [144]. The SiO_2 layer served as the mask layer in this step, providing an etch selectivity ratio of 1:10 for SiO_2:Si layers. The wafer was over etched to ensure the complete pattern transfer from SiO_2 to silicon layer (Figure 2.1.F).

After the completion of the above step, the top silicon layer of the SOI wafer has nanopores. Now the fabrication process flow moves towards the backside of the SOI wafer where a 100μm diameter pore is photolithographically patterned directly underneath the electron beam patterned nanopores and etched using deep reactive ion etching such that it contacts the buried oxide (BOX) layer of the SOI wafer. When the SiO_2 layer was grown before electron beam patterning of the nanopores, the backside of the wafer also ended up having a 60nm thick oxide layer. It is required to remove that 60nm thick SiO_2 layer from the backside before proceeding with the patterning and etching of the 100 μm pore. Prior to the removal process of the backside SiO_2 layer, the topside of the SOI wafer which contains etched nanopores is protected by using an 8 μm thick layer of AZ 4620 positive photoresist spun at 2500 RPM and then baked at 120°C for 5 minutes in an oven (Figure 2.1.G). After the application of the protective photoresist coating on the topside of the wafer, it is then immersed in diluted hydrofluoric acid, 1:4 HF 49% to water, to remove the 60nm thick backside SiO_2

(Figure 2.1.G). The next step after the removal of the 60nm thick backside SiO_2 layer is the removal of the protective photoresist coating from the topside of the SOI wafer. To accomplish this task, the wafer is then immersed for 5 minutes in AZ 400T photoresist stripper heated to 150°C. Once the wafer is a thoroughly cleaned, a fresh spin coat of AZ 4620 positive photoresist is applied to the topside of the SOI wafer, using 2500 RPM spin speed for the spin coater and baked at 120°C for 5 minutes in an oven, this time to protect the topside during the subsequent backside processing of the wafer.

Backside photolithography of the SOI wafer starts with spin coating hexamethyldisilazane (HMDS), an organosilicon compound at 2500 RPM. The application of HMDS prior to spin coating of the photoresist helps in adhesion of the photoresist with the silicon surface. This step is followed by the spin coating of AZ 4620 positive photoresist at 2500 RPM spin speed. The wafer is then soft baked at 90 °C on a level hot plate for 90 seconds. This results in an 8.1μm thick layer of AZ 4620 positive photoresist. Once the photoresist spin coat step is completed, optical lithography is done using an EV group 620 mask aligner on the SOI wafer with the help of the electron beam patterned alignment markers from the topside of the wafer. This alignment of the backside of the SOI wafer using the alignment markers from the topside ensures that when exposed the 100μm is directly beneath the nanopores etched on the topside of the SOI wafer. After the exposure, the SOI wafer is developed in 300MIF developer for 5 minutes (Figure

2.1.H). The developer is always maintained at 30°C in a water bath to avoid temperature dependent developing rate variations. This step is followed by the baking of the SOI wafer in a convection oven maintained at 120°C for 30 minutes to harden the photoresist layer (Figure 2.1.I). This bake step is done to further evaporate the solvent from the photoresist and increase the cross linking resulting in hardening of the photoresist. This is done because this photoresist layer is going to be the protective masking layer when the SOI wafer is processed in the deep reactive ion etcher for etching of the 100μm pore through the handle silicon wafer. An STS ASE tool was employed to etch the handle wafer using the previously described Bosch process with a typical cycle time of 14 seconds for etch and 7 seconds for passivation cycles for a total of 435 cycles. The etch rate of 4.2μm/ min at the surface was achieved in the beginning which dropped to about < 2 μm/ min as the etching went deeper. Due to the etch selectivity between SiO_2 and Si, the etching stopped at the buried oxide layer (Figure 2.1.J). To etch the handle wafer the SF_6 etch cycles were run at 600W coil power, 12 W platen power using 136 sccm of SF_6. Similarly for the passivation cycles the tool was run at 600W coil power, 2W platen power and 90 sccm of C_4F_8. Once the etch was complete, the SOI wafer was cleaned in AZ 400T photoresist stripper for 5 minutes at 150°C to clean the protective photoresist layer on the topside as well as the patterned layer on the backside. The SOI wafer was then cleaned in 1:1 ratio

of H_2SO_4 and H_2O_2 piranha solution for 5 minutes to clean the wafer of organic residuals from the photoresist or photoresist stripper.

After the completion of the backside etch of the handle wafer, the nanopores etched in the top silicon layer of the SOI wafer remain separated from the backside 100μm pore by the 1 μm buried oxide layer. The buried oxide layer plays an important role not only in the electrical measurements, as described in the beginning of this chapter, but also in the fabrication steps by providing a convenient etch stop layer for the etching of the backside handle wafer. The buried oxide (BOX) layer also serves as a support structure for the thin membrane that supports the nanopore in the top silicon layer, enhancing the mechanical robustness of the top silicon membrane. Since, the presence of the buried oxide layer is critical, it is desired to keep most of the layer intact and open a relatively smaller pore, preferably underneath the nanopores on the topside of the silicon layer to connect with the 100μm backside pore in the handle wafer. Thus, allowing a continuous path for the ionic current to flow through the nanopore chip. The approach taken to meet this goal was to protect the backside of the SOI wafer and wet etch the buried oxide layer using buffered oxide etchant, BOE (20:1). Since, the backside is protected, the buffered oxide etchant will flow through the nanopores etched in the topside layer and etch the buried oxide underneath. This was achieved by using a fixture called a single side etcher. The resulting etch of the buried oxide was a self selective, self aligned wet etch,

directly underneath the nanopores in the top silicon layer of the SOI wafer. The etch rates typically encountered for bulk wet etching of SiO_2 are approximately 30nm/min, but in this case the etch rate of the buried oxide is considerably slower than the bulk etch rate. This is attributed to the mass transport limitations arising because of the constricted flow passage offered by the nanopores. Another important factor to take into account for the wet etch of the buried oxide is the isotropic nature of the etching. The etching of the buried oxide starts at the interface between Si/SiO_2 and propagates forward in a hemispherical fashion. This results in a hemispherical cavity in the buried oxide underneath the nanopores. The SOI wafer was immersed in buffered oxide etchant solution for an etch time of 60 minutes to ensure that buried oxide is completely etched underneath the nanopore resulting in a continuous path of the ionic current to flow. This resulted in a 2µm cavity (Figure 2.1.K). Once the buried oxide etch was complete, the SOI wafer was then cleaned in a 1:1 H_2SO_4 and H_2O_2 piranha solution for 5 minutes.

The last step of the fabrication of nanopores was thermal growth of a SiO_2 layer using dry oxidation. This layer serves the role of passivation layer for the nanopores and also reduces the diameter of the nanopore. Dry thermal oxidation of the nanopores is highly reliable, conformable, and a well controlled process, which allows the capability to reduce the diameter of the nanopores to any desired value and to achieve an atomically smooth surface. A 60 nm thick layer of SiO_2

39

was thermally grown at 1000°C for 60 minutes in a dry oxygen atmosphere (Figure 2.1.L).

Once the final oxidation step was complete, the topside of the SOI wafer was then spin coated with AZ 4620 at 2500 RPM and baked on a level hot plate for 90 second at 90°C temperature and then in an oven at 120°C for 5 minutes. After this step, the backside of the SOI wafer was spin coated with HMDS, followed by spin coating of AZ 4620 at 2500 RPM and a soft bake for 90 seconds at 90°C giving a resist thickness of 8.1μm. Using the EV group mask aligner, grid lines are patterned on the backside of the SOI wafer to allow for accurate scribing of the SOI wafer into 1cm x 1cm die containing either a single nanopore or an array of nanopores which could then be mounted on measurement fixtures for ion transport experiments. One SOI wafer resulted in 49 die from the fabrication. Once the individual die were ready, they were cleaned in pre heated AZ 400T photoresist stripper at 150°C for 15 minutes followed by cleaning in 1:1 solution of H_2SO_4 and H_2O_2 for 15 minutes, resulting in pristine die. The individual 1cm x 1cm nanopore die were then stored in 1:1 isopropyl alcohol and water solution to prevent contamination and microbial growth. The nanopores were now ready for ion transport and nanoscale particle translocation experiments.
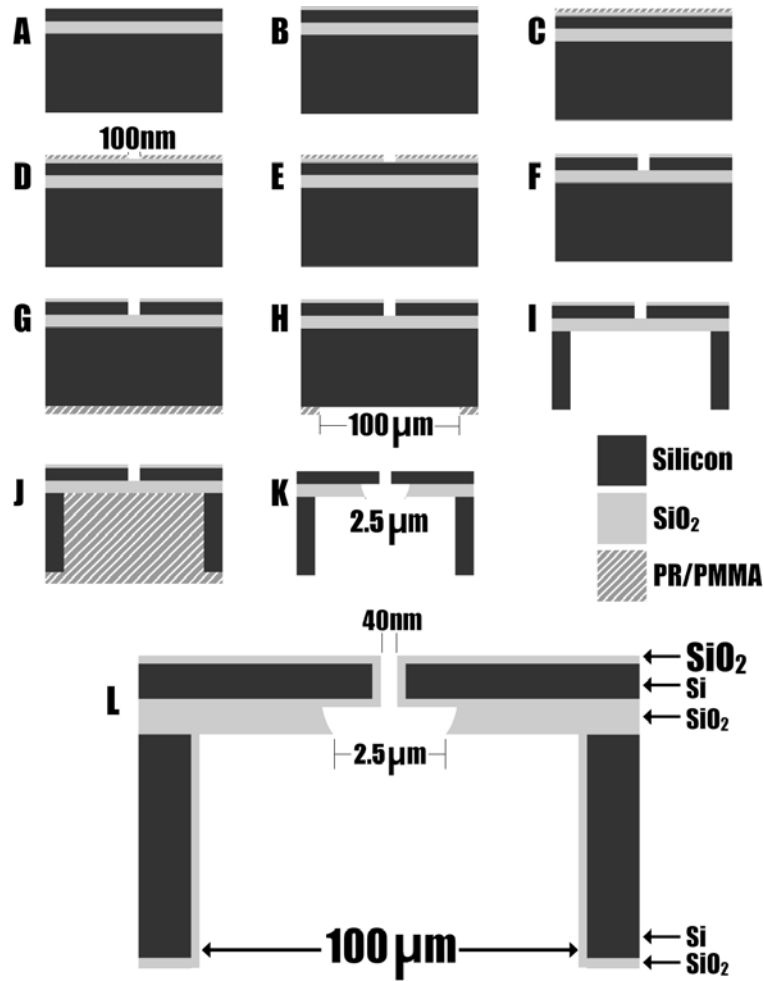
Figure 2.1 Complete process flow for the fabrication of a single cylindrical nanopore. (a) The process begins with a SOI wafer that is then (b) thermally oxidized to grow 60 nm of SiO_2. (c) The wafer is then spin coated with PMMA and (d) patterned using EBL to open a 100 nm diameter aperture. (e) The SiO_2 is then etched in a RIE with CHF_3:Ar, (f) followed by etching of the device layer in an ICP RIE with Cl_2. Processing then shifts to the backside of the wafer, (g) where AZ4620 is spin coated and (h) patterned with 100 lm openings. The handle wafer is then etched in a DRIE with SF_6 and C_4F_8 using the Bosch process. (j) The backside is then spin coated with AZ4620 and soft baked to fill the 100 lm aperture, (k) after which the wafer is immersed in BOE 20:1 to etch the buried SiO2 through the topside aperture. (l) The wafer is then thermally oxidized to reduce the pore diameter [22, 23].

41

2.5 Results of Nanopore Fabrication

Using the fabrication process above, single nanopores as well as an array of cylindrical nanopores were fabricated. Shown in Figure 2.2 is a cross-sectional scanning electron image of a typical single nanopore structure. The layer containing the nanopores is the device silicon layer. The cavity is the buried oxide layer. The handle wafer is left intact for manual scribing. The pore has an 'hourglass' profile and the diameter varies approximately 10-20% across its length. The picture was taken by Dr. Leo Petrossian.
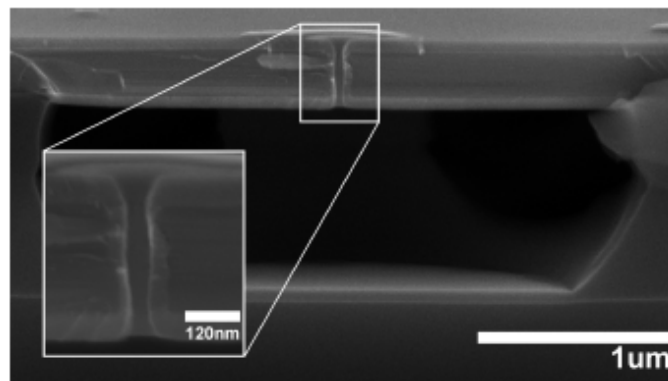
Figure 2.2: Cross sectional scanning electron image of a typical single 40nm cylindrical nanopore structure. The layer containing the nanopore is device silicon layer. The cavity is the buried oxide layer. The handle wafer is left intact for manual scribing [23].

The geometry of the pores in this array was defined to be a nominal 100nm in diameter by electron beam patterning. The inset picture is a zoomed in view of the nanopore which clearly demonstrates the cylindrical profile with

rounded edges at the top and bottom due to the thermal oxidation. The close to vertical sidewalls of the nanopore allow for a uniform electric field to be developed throughout the nanopore which is then used in manipulating the ion transport.
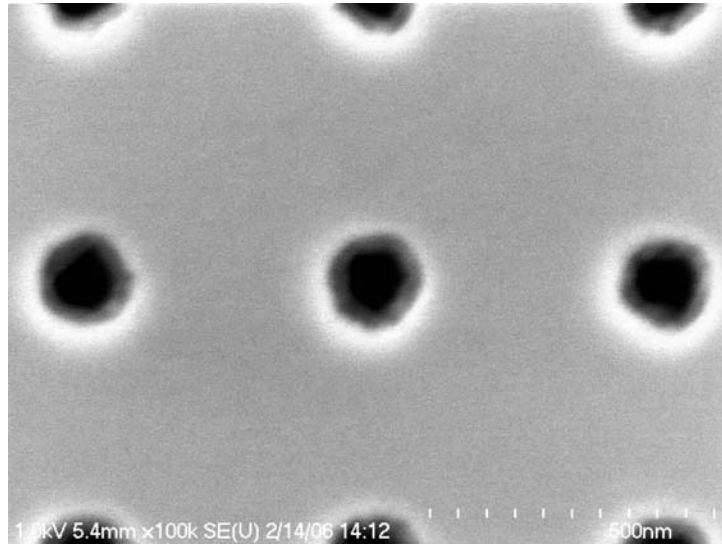
Figure 2.3: Partial view of a 5x5 95nm single pore diameter array. The fuzzy edges are the silicon dioxide grown in the last step of the fabrication.

Figure 2.3 is a field emission scanning electron microscope picture of a fabricated 5x5 nanopore array. In order for the clarity of the picture only the center three pores are shown. The nanopores in the array are uniformly spaced demonstrating the precise positional control afforded by the fabrication process flow presented in this chapter. The nanopores patterned in the array shown have a center to center distance of 500nm and have maintained their circular definition and demonstrate the high packing density that this fabrication process flow can

achieve. This high packing density and the cylindrical form of the nanopores is achievable because of the use of anisotropic chlorine reactive ion etching. This is the advantage of this process flow compared to the wet etching fabrication processes using potassium hydroxide (KOH). In wet etching processes the initial patterned area is much larger compared to the pore diameter to account for the preferential etch of silicon along the lattice planes which leads to loss of important silicon real estate. The process flow presented in this study is free from constraints in the horizontal direction. The electron beam lithography can be further optimized to pattern features as small as 20nm which in turn allows for further increase in packing density. The major limitations which would be encountered in increasing the packing density would be the robustness of the silicon membrane and proximity effects in the electron beam lithography. The fuzzy edges are the silicon dioxide grown in the last step of the fabrication.

2.6 Conclusion

This chapter presents a detailed description of a nanopore fabrication process flow capable of reliably producing cylindrical nanopores in silicon-on-insulator substrates using standard cleanroom fabrication processes. The detailed description of the fabrication process flow started with an overview of major semiconductor cleanroom processes which form the crux of the complete process flow. The description continued with presenting the results of the fabrication and

discussing the benefits of the process flow presented in this study compared to other established processes.

The nanopore fabrication process flow utilizing a combination of electron beam lithography and reactive ion etch steps presented in this study allows to mass fabricate on a wafer level nanopore arrays and single nanopores of desired diameter using standard semiconductor cleanroom fabrication processes. The process allows a precise definition of nanopores diameters and a high packing density with reproducible results.

3. MEASUREMENT METHODOLOGY AND EXPERIMENTAL SETUP

3.1 Introduction

This chapter describes in detail the experimental protocol, measurement methodology and instruments used in ion transport characterization as well as field effect modulation of ion transport through the nanopores. The experimental protocol is comprised of cleaning and mounting of nanopore chips for measurements, electrolyte solution preparation, electrode preparation for ion transport characterization as well as field effect manipulation of ion transport, signal transduction and amplification, and data acquisition hardware as well as software.

3.2 Preparation of Nanopore chip for Measurements

After the fabrication, the nanopore chips were stored in 70% IPA and nanopore water solution to prevent nanopore chip surface contamination as well as blocking of pores due to dust particles in ambient air. The nanopore chips, prior to mounting on the Teflon holders for measurements were cleaned in 1:1 solution of sulfuric acid and hydrogen peroxide for 15 minutes in a cleanroom environment.

3.2.1 Mounting of Nanopore Chip on Holders

In order to perform the ion transport experiments the nanopore chip was sandwiched between two custom made Teflon chambers filled with electrolyte solution using threaded metal rods with screws. The rectangular Teflon chambers were machined from solid Teflon blocks. One of the walls of the Teflon chamber was made up of a glass cover slip for mounting and aligning the nanopore chip and the chamber wall parallel to the glass cover slip had a 1.5mm diameter hole for mounting the nanopore as shown in Figure 3.1.
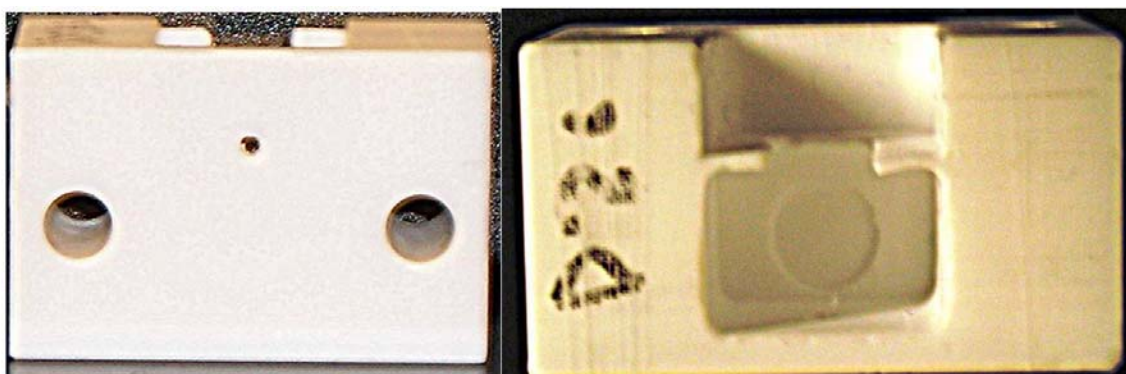
Figure 3.1: Teflon Holder fabricated from solid Teflon Block before gluing the glass cover slip at the back wall.

The glass cover slip was glued to the Teflon chambers using two different adhesives. The first layer of adhesive consisted of alcohol resistant epoxy EP5347 (Eager Polymers, Chicago, IL) and the second layer of adhesive consisted of water resistant silicone adhesive (DAP Products Inc., Baltimore, MD) as shown in Figure 3.2.
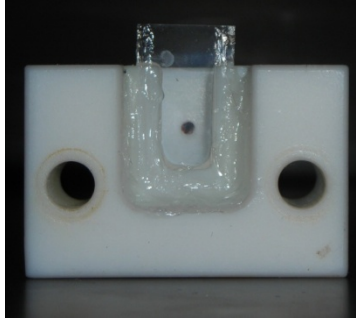
Figure 3.2: Teflon Holder with Glass cover slip.

Due to the involvement of liquid solutions in the experiment it became imperative to make sure that the seal between the nanopore chip and the Teflon chamber is leak proof. Different types of materials were used to test the measurement set up seal resistance. The materials tested for the purpose of making the set up leak proof were PDMS gaskets, rubber gaskets and silicone O-rings (McMaster Carr, Santa Fe Springs, CA). It was found out that silicone O-rings provided a leak proof seal for the set up. Figure 3.3 shows silicone O-rings glued to the Teflon holders.
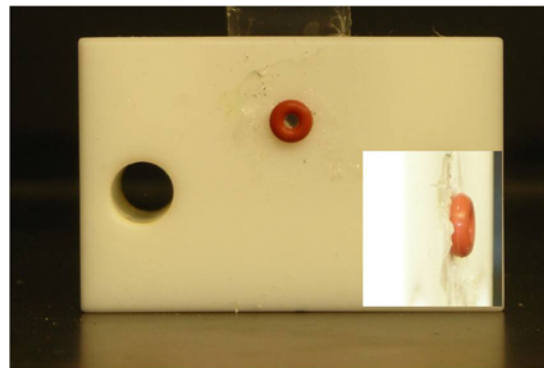
Figure 3.3: Silicone O-rings glued to the Teflon holders using solvent resistant epoxy ensuring a leak proof assembly.

Figure 3.4 (A) shows the Teflon holder placed with the threaded metal rods already in place so that the second Teflon chamber could be slid onto the metal rods completing the assembly, once the nanopore chip is in place. Figure 3.4 (B) shows the device mounted in such a way so as to ensure that the nanopore was placed approximately centrally within the silicone O-rings. By looking through the glass cover slip window the second chamber was aligned with the first chamber using the threaded metal rods as guiding rails. Once the assembly was in place the final metal screws were put in place to secure the assembly. Figure 3.4 (C) shows completed assembly with the nanopore chip sandwiched between the silicone O-rings and Teflon holders held in place with the help of metal rods. Figure 3.4 (D) shows the close up of the mounted nanopore between the silicone O-rings. Once the chip was mounted dry nitrogen was blown in the gap between the Teflon holders where the nanopore chip is visible to ensure that the silicone O-ring, exterior walls of the Teflon chambers and exposed parts of the mounted nanopore chip are completely dry. The last step of the mounting procedure is the degassing of the nanopore assembly for up to 12 hours in a desiccator to remove any residual bubbles that were present.
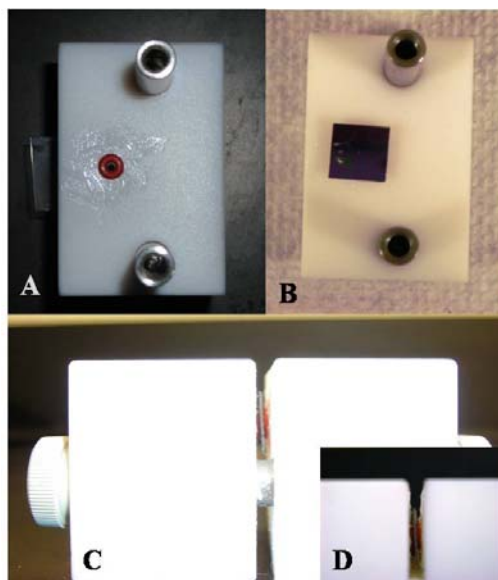
Figure 3.4: Nanopore chip mounting procedure. (A) Teflon holder in place with threaded metal rods. (B) Nanopore pore chip aligned with the bottom O-ring. (C) Completed assembly with the nanopore sandwiched between the O-rings. (D) Close up of the mounted nanopore chip.

3.2.2 Electrodes

Platinum and Ag/AgCl electrodes were used in ion transport characterization through the nanopores. The Platinum electrodes were purchased from Goodfellow, Cambridge, UK and the silver wire for the Ag/AgCl electrodes was purchased from Alfa Aesar, Ward Hill, MA. The Ag/AgCl electrodes were made by soldering a silver wire to a proprietary copper pin from Molecular Devices, Sunnyvale, CA, which plugs into the headstage of the low noise current amplifier. The Ag silver wire was then sanded to remove any residual grease, rinsed with deionized water and then soaked in 5% sodium hypochlorite (NaOCl, Bleach) solution for 20 minutes to form a surface coating of AgCl. A change in

color of the silver wire surface from metallic silver to white served as a visual confirmation of the chloridization process. The chloridization step was performed prior to every run of the experiment because of continual loss of Cl^- ions from the electrode surface into the solution due to passing of charge through the electrode during the measurements.

3.2.3   Preparation of Ionic Solutions

Ion transport characterization and field effect experiments were performed using aqueous HCl solutions. To minimize any type of contamination in the solutions a set of glassware (measuring cylinder and beakers) was dedicated for the purpose of electrolyte solution preparation and was stored in an airtight plastic bag. Before preparing solutions, the glassware was cleaned in 1:1 solution of sulfuric acid and hydrogen peroxide for 15 minutes and rinsed with nanopore deionized water. After the rinse the glassware was baked for 15 minutes in an oven at 80°C. The glassware was then left in a closed hood for cooling down to room temperature. A total of 12 different nominal electrolyte concentrations were prepared and the process was always started by preparing the solution of the least electrolytic concentration first. Nanopure water from a Cascada Bio water purification system (Pall Corporation, Ann Arbor, MI) was used in the preparation of all solutions. Table 1 shows the concentrations prepared and volume of HCl required for that concentration.

Concentration (M)	Volume of 36.5% HCl (in mL)
3.16μM	0.00006693
10μM	0.0004236
31.6μM	0.0006693
100μM	0.004236
316μM	0.006693
1mM	0.04236
3.16mM	0.06693
10mM	0.4236
31.6mM	0.6693
100mM	4.236

Table 3.1: Volume of 36.5 % assay hydrochloric acid (HCl) acid required for preparing broad range ionic solution. Typically concentrations below 316 μM were prepared by diluting higher concentrations of solution in appropriate ratios while measuring solution conductivity using an Accumet XL50 multiparameter meter.

Aqueous HCl solutions were prepared using electronic grade HCl (Assay 36.5%, Columbus Chemical Industries, Columbus, Ohio) was used. The desired volume of HCl, for a given concentration was poured into the measuring cylinder and added to the beaker filled with Nanopore™ water. The process of making dilute aqueous solutions was done in a chemical hood due to safety reasons. Once

the solutions were prepared their conductivity was measured using the Accumet XL-50 conductivity meter (Fisher Scientific, Pittsburgh, PA) which was then used to calculate the actual concentration of the electrolytes in the solution. The measured conductivity and concentration values are plotted in Figure 3.5.
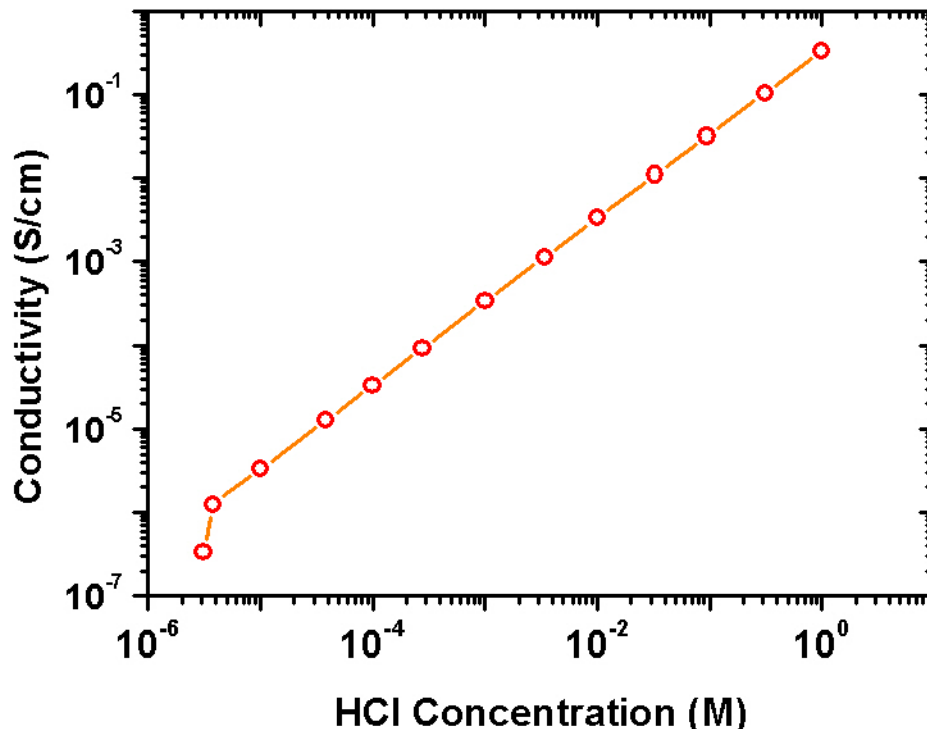
Figure 3.5: Electrical conductivity of aqueous HCl solution as a function of concentration of HCl.

The electrolyte solution bottles were then topped off with Argon gas, capped and sealed with three layers of Parafilm®. Argon was used because being heavier than air it can form a protective layer on top of the solution. Also, Argon is inert therefore it will not dissolve into the solution and not adversely affect the

pH and conductivity of the electrolyte solution over a long period of time. The bottles were then labeled with the measured conductivity value, nominal concentration and measured concentration values before storage. The bottles were then refrigerated at 5°C to prevent any kind of microbial growth in the solutions. Prior to each experiment run the solution was allowed to come to room temperature. At room temperature the conductivity of the electrolyte solutions was measured again and recorded. As stated before, the measured conductivity value was then used to back calculate the concentration of electrolyte in the solution. This was done to keep track of the variation of electrolyte concentration in the solution over a period of time. The solutions with higher concentrations, 10mM or higher, did not show large variations in conductivity but the solutions in the concentration range less than 1mM displayed significant variation in conductivity with time, even after all the precautions. Due to this gradual variation in concentration of low electrolyte concentration solutions, the lower concentration solutions were discarded after every three days and new solutions were prepared for the experiments.

3.3 Electrical Set up

In a nutshell, the measurement methodology for ion transport through the nanopores is as follows. An ionic solution filled nanopore acts as a variable resistor whose resistance is directly proportional to the electrolyte concentration

in the solution. For a nanopore of given diameter, at high electrolyte concentration, the resistance of the nanopore is in few tens of MΩs due to the presence of large number of ionic charge carriers in the solution. At low electrolyte concentrations, the nanopore resistance is measured in ~GΩs. The electrodes submerged in the opposing baths act as signal transducers between the electronic and ionic current. The low noise current amplifier monitors the current flowing between the two electrodes while keeping the applied voltage between the two electrodes constant, a process known as voltage clamping. The measured current flowing between the electrodes is amplified and converted back to a voltage signal and is output to a data acquisition system which collects the data. The data then can be processed to calculate various parameters characteristics of a given system.

3.3.1 Low Noise Patch Clamp Amplifier

A low noise patch clamp amplifier is the primary instrument used in electrophysiology for measuring ion transport through lipid bilayers and membrane ion channel. Electrophysiologists are especially interested in the activity of membrane proteins that provide conductive pathways through biological membranes: ion channels, transmitter receptors, and ionic pumps. Ion channel activity results in changes of membrane conductance. Membrane current, of the order of a few picoamps is measured because there is no direct way of measuring membrane conductance. One of the primary modes in which a path

clamp amplifier is operated is called voltage clamp mode [145]. In this mode, the amplifier keeps the applied voltage, also called the holding potential, constant and measures the resulting ionic current. The constant holding potential across the membrane ensures that the membrane current measured is linearly proportional to the conductance being studied. Due to the nature and sensitivity of the ion channels measurements patch clamp amplifiers have two important attributes which allow its usage in nanopore ion transport characterization. These attributes are maximum speed of the response and minimum noise in the measurements. Another advantage of using a voltage clamp amplifier is that as the electrode potential drifts, the amplifier continues to clamp the voltage applied across the device to specified value. The drift in electrode potential will be recorded as an offset current in the actual recording and can be taken into consideration.

Measuring ion transport through nanopores specifically at low ionic solution concentrations poses similar challenges as ion channel measurements. At lower electrolyte concentrations the number of ionic charge carriers passing through a nanopore is very low. Due to this, the nanopore acts as a high resistor connected in series between the electrodes placed in the opposite baths. This high resistance imposes a limit on the speed with which voltage changes can be applied across a nanopore and it also limits the time resolution of current recordings. Also, due to the low number of ions available for ion transport through nanopores at low concentration electrolyte solution, the current measured is very sensitive to

noise. Thus, to have accurate results of ion transport through the nanopores a current amplifier with high bandwidth and low noise is a necessity.

A patch clamp amplifier is basically a sensitive current-to-voltage converter, converting small currents into voltage signals which then can be sampled by a computer. The workings of a patch clamp amplifier operating in voltage clamp mode can be explained by using a simple resistive feedback operational amplifier circuit. The electrodes complete the circuit by connecting the Teflon chamber + electrolyte solution + nanopore chip system with the outside electronics. The operational amplifier's positive and negative inputs are forced to the same potential in order to keep the applied potential V_{App} across the chip constant. Also, the current flowing into the operational amplifier, I_{In} is equal to the current flowing out of it (I_{Out}). All the current flowing through the operational amplifier is going through the feedback resistor R_f such that (Figure 3.6):

$$V_{Out} = I_{Out} * R_f \qquad\qquad (3.1)$$
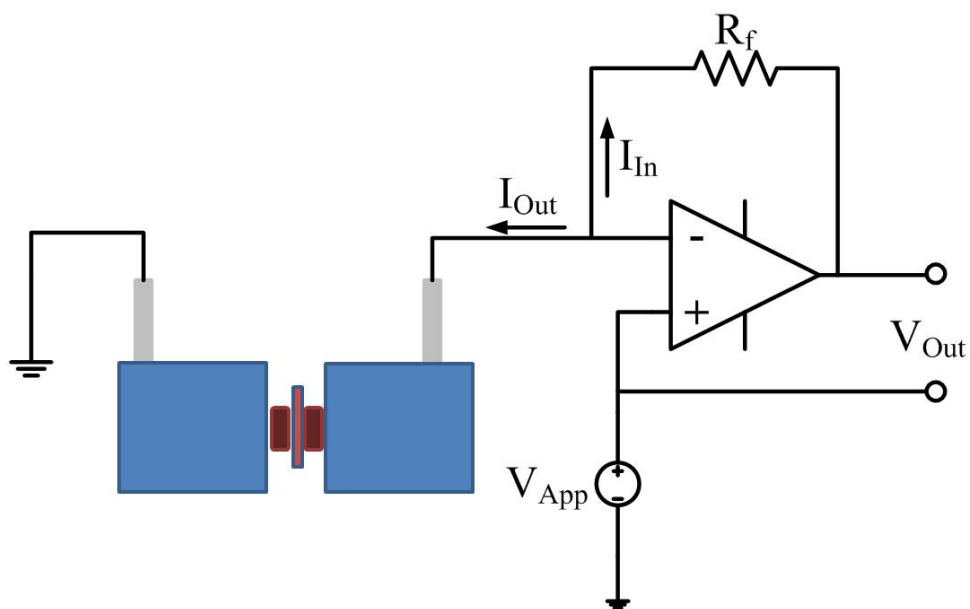
Figure 3.6: A simple operational amplifier circuit depicting the voltage clamp configuration used to hold the constant potential across a nanopore chip and measure the resulting current.

where V_{Out} is the measured output voltage and R_f is the feedback resistor and typically the gain of the circuit. Thus, in order to measure the current flowing through the nanopore all that is required is a resistor of known value and the measured voltage output. All the experiments performed in this study used an Axopatch 200B (Molecular Devices, Sunnyvale, CA) low noise current amplifier (Figure 3.7) in constant voltage or voltage clamp mode.

Figure 3.7: Axopatch 200B Low Noise Current Amplifier.

The Axopatch 200B uses a cooled dual junction field effect transistor input headstage front end amplifier added with an operational amplifier with high gain as a current to voltage converter. The headstage front end amplifier is separate from the main instrument which allows the convenience of placing the headstage in the Faraday cage next to the device measured. This also serves the purpose of minimizing the induced current noise in cables before the first amplification of the system. The Axopatch 200B utilizes two resistive feedbacks and one capacitive feedback mode in the headstage amplifier. All of the experiments performed in characterizing ion transport through the nanopores used the resistive feedback mechanism of the Axopatch 200B in voltage clamp mode.

The resistive feedback configurations in the Axopatch 200B are the "*Whole Cell β = 1*" and "*Whole Cell β = 0.1*". The "*Whole Cell β = 1*" configuration has a parallel combination of a 500MΩ resistor and a 1pF capacitor as the feedback element and for the "*Whole Cell β = 0.1*" configuration a parallel combination of a 50MΩ resistor and a 1pF capacitor serve as feedback elements.

The overall gain of the amplifier, in voltage clamp mode, is given by $I = \alpha \beta$ mV/pA. α is the gain of the output gain of the amplifier and ranges from 0.5-100. The output gain is the gain of the second voltage amplifier after the headstage amplifier. The open circuit current noise for the Axopatch 200B is 0.45pA rms for the "*Whole Cell $\beta = 1$*" configuration and 1.45pA RMS for the "*Whole Cell $\beta = 0.1$*" configuration. A couple of additional features in the Axopatch 200B also help in reducing the current noise further and make these measurements possible. The Axopatch 200B has an adjustable 4-pole low-pass Bessel filter which filters out all the higher frequency noise in the range of 1kHz-100kHz. The second feature boosting the low noise capabilities is the integration of a Peltier thermoelectric cooler into the headstage. This reduces the current noise by cooling the input stage to -20°C.

3.3.2   Data Acquisition

The Axopatch 200B can be externally controlled by a desktop computer using a DAQ system. Analog to digital (A/D) converters convert an analog voltage signal to a digital representation consisting of some quantized bit value. The input range (±10V) of the A/D converter must be matched to the output range of the current amplifier so that data is not lost by clipping i.e. amplifier voltage output exceeding ±10V. A Digidata 1322A from Molecular Devices, Sunnyvale, CA (Figure 3.8) was used for data acquisition. The Digidata 1322A is a high-

60

resolution, low-noise digitizer intended for precision scientific applications. The Digidata 1322A digitizes at an aggregate speed of 500 kHz. It provides sixteen multiplexed, 16-bit analog inputs and two non-multiplexed, 16-bit analog outputs. The Digidata 1322A communicates with the host computer through the SCSI bus.

Figure 3.8: Digidata 1322A data acquisition system.

3.3.3   Measurement Methodologies

There were two sets of experiments performed to study ion transport through the nanopores. The first set of experiments consisted of measuring the conductance of nanopores as a function of electrolyte concentration. By measuring the conductance one can observe the effects of interaction between the nanopore wall surface charge and the ions translocating through the nanopores. The conductance measurements were always started with the lowest electrolyte concentration solution first. To exchange the electrolyte solution, the solution

which was just used in the measurement was removed from the Teflon chambers using a pipette and rinsed with nanopure water, and then rinsed with the new electrolyte solution of higher concentration three times, and finally filled and measured on the fourth turn. This ensured that when the measurement for the next higher concentration solution was actually done, the solution in the nanopore was as close to the desired higher concentration electrolyte solution as possible. This step of rinsing the Teflon chambers prior to measurements was followed for the field effect measurements as well. The conductivity value of the electrolyte solution was also measured along with the ionic conductance. This constituted the first set of measurements. The results of these measurements will be discussed in next chapter.

Having successfully performed the first set of measurements the second set of experiments involved field effect modulation of ion transport through the nanopores. The aim of this set of experiments was to explore the possibility of influencing the ion transport through the nanopore by applying a second electric field transverse to the flow of ions through the nanopore, a process similar to operation of MOSFETs in semiconductor devices.

The electrodes for the electrostatic modulation of ion transport through the nanopores were made using standard jumper wire (Digikey, Thief River Falls, MN) and molded using a pair of pliers to resemble a paper clip. The top of these electrodes was then soldered to standard wire for connection to the instruments.

The nanopore chip was then clamped between electrodes ensuring a mechanically robust, as well as consistent, three dimensional electrical contact. To accomplish a well-controlled electric field established via an electrostatic gate in a nanopore chip, it was necessary to position the gate electrode in close proximity to the nanopore. The original intent was to use small alligator clips but it was found that these clips exerted too much force on the SOI chip creating a real danger of breaking the chip. The electrode, chip and Teflon holder assembly is shown in the Figure 3.9.
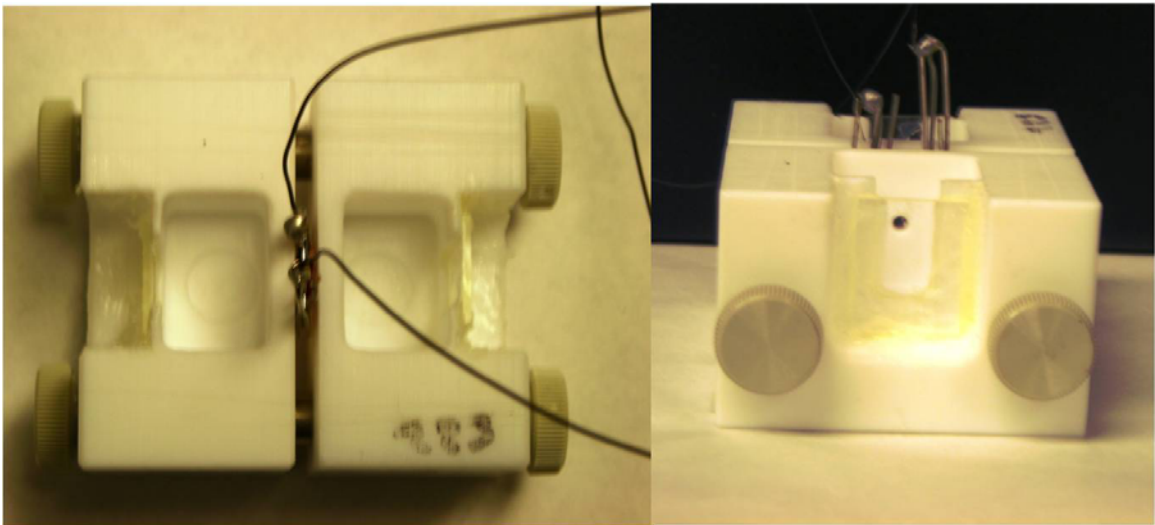
Figure 3.9: Custom made electrodes attached to the nanopore chip mounted in teflon chamber assembly. (A) Top View. (B) Front View

One of the electrodes was connected to a Keithley 236 source measure unit which supplied the constant DC voltage for biasing as well as measuring the

leakage current through the SOI substrate. The magnitude of the leakage current was continuously monitored in order to make sure that the current measured is due to the flow of ions through the nanopore. The second electrode was used to connect the Keithley 2182 nanovoltmeter. The nanovoltmeter was used to verify that there was no bias voltage drop due to high contact resistance. The ground connections from the Keithley 236 and Keithley 2182 were then connected to the Axopatch ground. The setup schematic is shown in Figure 3.10.
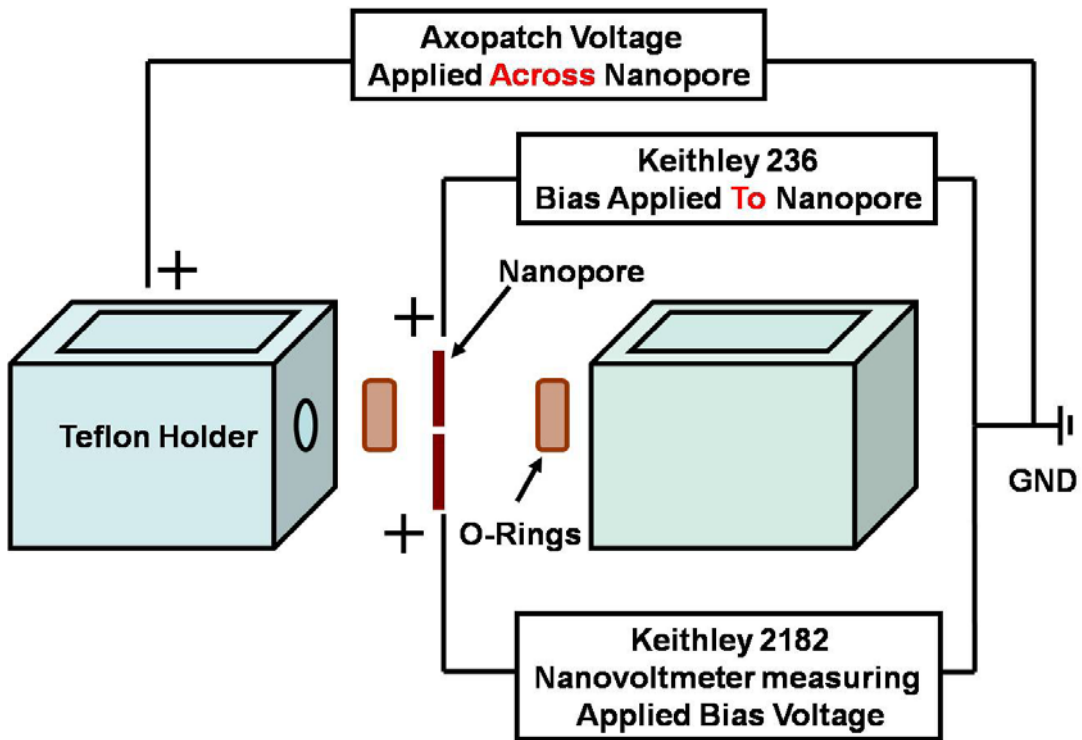
Figure 3.10: Axopatch 200B is used to measure ionic current flowing through a nanopore. Keithly 236 is used to apply gate bias to the nanopore chip for field effect modulation experiments. Keithley 2182 is used to monitor the gate bias applied to the nanopore as well as the leakage current flowing through the nanopore chip.

3.4 Noise Considerations

A major challenge in characterizing ion transport through the nanopores by measuring the ionic conductance is the noise level of the surrounding environment. Experimental measurements pick up mechanical vibrations and random noise as the experiments are conducted in the same frequency range as power supplies. Thus, electrical isolation as well as mechanical stability of the measurement set up becomes paramount for successful low noise measurements.

Figure 3.11: Faraday cage used to shield the nanopore chip and the electrodes from electrical noise.

The measurements were carried out in a Faraday cage (Warner Instruments LLC, Hamden, CT), Figure 11, to electrically isolate the nanopore chip system by shielding it from electromagnetic radiation. A primary source of noise in experiments is the electrical power system operating at 60Hz. An unshielded cable can easily become a source of noise. In addition the system is

also exposed to electrical noises from computer power supplies and monitors, amplifier power supplies, transformers, switch mode power supplies, and any other electrical appliances plugged into the wall. The sensitivity of these measurements necessitates proper shielding of the nanopore chip assembly from these sources of noise.

Ground-loop noise arises when shielding is grounded at more than one place. Magnetic fields may induce currents in this loop. Moreover, if the different grounds are at slightly different potentials, a current may flow through the shielding and introduce noise. A single common ground point for the whole electrical system is an important way to prevent spurious noise due to ground loops between different parts of the setup.

Another source of noise which can affect the experimental results, in addition to electrical noises is mechanical noise. Building vibrations due to compressors in refrigerators and AC systems, high vacuum pumps or any other type of heavy machinery operating in the vicinity, people walking in the lab close to the area of the measurement set up can lead to mechanical vibrations in the system. An isolation air table (Warner Instruments LLC, Hamden, CT) was used to dampen the major vibrations. The air table uses a continuous supply of nitrogen at 30psi to maintain the integrity of the bellows inside the air table.   In conjunction with this, an *active* anti-vibration table from Halcyonics, as shown in Figure 12, was also used to dampen the mechanical vibrations. The active

vibration isolation system works by monitoring the absolute velocity of the mass to be isolated, and then generating a compensating movement from an actuator. The Nano 20 benchtop unit protects the instruments from vibrations from about 0.6 Hz to high frequency, providing 40 dB attenuation above 10 Hz. The actuator replaces the viscous damper of traditional passive isolation tables. The electromechanical sensors detect absolute motion in all 6 axes, and the actuators immediately counteract this motion. Another precaution taken to shield the system from mechanical vibrations was to keep the exposed surface of the electrodes completely submerged within the electrolyte solution.
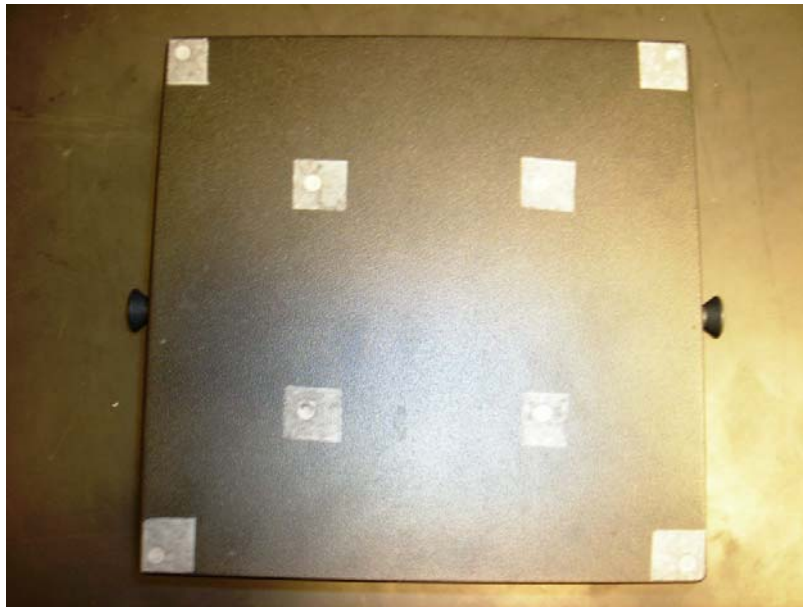
Figure 3.12: Halcyonics active anti vibration table.

3.5 Conclusion

In this chapter the experimental platform set up and the measurement protocol established to characterize as well as manipulate ion transport through the nanopores was explained in detail. The instruments used in the measurements and their functionality were also discussed. The nanopore chip preparation, chip mounting, electrolyte solution preparation protocol and the measurement methodologies were also explained.

4. CHARACTERIZATION AND FIELD EFFECT MODULATION OF ION TRANSPORT THROUGH NANOPORES

4.1 Introduction

In the last few years, microfabrication technologies have contributed immensely to advances in microscale analysis systems. In particular, recent developments in design, patterning, and utilization of microfluidic devices have found many applications in transport, separation, identification, and synthesis of a wide range of chemical, biochemical, and biological species [21, 67, 88, 146-153].

In the past, understanding of various transport processes was targeted at size scales where the continuum description of a fluid could be employed to understand the observed phenomena. However, the drive for miniaturization has lead to a significant decrease in the mass and the volume of analytes and reagents used for analysis. In addition, due to advances in nanofabrication, materials and structures are designed at a molecular level and then fabricated with control of composition and dimensions at atomic length scales. Due to the confined geometries at the nanometer level, the continuum assumption often presents an incomplete picture of the physical phenomena observed. Independent of the type of driving force, the novel attributes of nanostructures in general, and nanopores in particular, ensure ionic and molecular transport characteristics that are

fundamentally different from those in larger micrometer and millimeter scale structures.

The characteristics of ionic and molecular transport often observed in nanostructures are pronounced influence of surface charge density, coupled and enhanced mass and ion transport, nanostructure size and shape, mobile phase ionic strength, large surface-to-volume ratio, large mass-to-charge ratio of ionic species in an ionic solution, ion depletion/enrichment, ion current rectification, and diminished background signals [1-21]. These myriad phenomena, point to a simple fact that the molecular characteristics can dominate the behavior of a nanostructure.

A major impetus to study these transport processes also comes from the study of nanometer sized pores formed by proteins, called ion channels, which are prevalent in biology where they regulate the flow of ions and molecules through the otherwise impermeable cell membrane [56-59]. In biology, the cell membrane presents an impermeable barrier to ion transport and nanometer pores formed by proteins, offer an easy conduit in order to facilitate molecular and ionic transport. Similarly, a few charge selective phenomena have previously been observed in membrane filtration studies which mainly contain nanopore and nanochannel with irregular geometries, often with high porosity [154, 155].

The studies performed in membrane filtration research, although useful in providing insight into fluid transport at the nanometer level, often arrived at the

results after intricate statistical analysis. In case of biological nanopores, the complexity of ion selective transport as well as the susceptibility of the ion channels to the external factors such as temperature, solution pH and solution ionic concentration presents a challenge to a thorough understanding and control of ionic and molecular transport [4, 5]. Due to this the need to understand molecular and ionic transport in extensive detail in isolated and near ideal systems is further underscored.

Researchers have just started to realize these challenges and possibilities, yet it is clear that the ability and understanding to achieve efficient and intelligent control of molecular and ionic transport within these nanostructures will enable the construction of new devices that can address fundamental problems in molecular and ionic transport as well as open vistas for efficient and intelligent control of nanoscale analytes. Efficient and intelligent control of the nanoscale analytes would enable materials and structures which can sense size, charge, and molecular shape of the target analyte and generate signals that control transport on the basis of those characteristics.

Solid state nanopores have come up to fill the need for near ideal and isolated physical modeling systems to study and understand ion transport at the nanometer level. Solid state nanopores offer precise control of geometry, are chemically, mechanically, electrically and thermally robust and stable, and can be integrated with electronic circuits. Nanopores also facilitate the prospect of label-free single

molecule detection by exploiting ion transport modulation. These benefits make solid state nanopores suitable candidates for extensive ionic and molecular transport studies [21, 74, 89].

This chapter briefly discusses the physical phenomena typically observed at the nanometer level ionic and molecular transport and then presents the results of ion transport measurement through single as well as arrays of nanopores. The chapter also presents the results of control of ionic transport through the nanopores by applying a voltage to the SOI substrate, in a similar fashion as a semiconductor field effect transistor.

4.2 Electric Double Layer

When a solid surface comes in contact with an ionic solution, it typically acquires an electric charge which influences the distribution of nearby ions in the solution. Surface charge on a solid/ ionic solution interface is predominantly caused by the dissociation of surface groups and the specific adsorption of ions in solution to the surface. The solid surface acquires a positive or a negative charge depending on the number and type of the acid and base groups present in the solution. This results in the solid surface acquiring either a positive or a negative surface charge density. For ease of understanding, ions in the solution of the same charge as the surface charge are called *coions* and ions of opposite charge as the surface charge are called *counterions*. As a result of the fixed surface charge at

72

the solid/ ionic interface an oppositely charged region of counterions is formed in the ionic solution to maintain the electroneutrality of the solid/ ionic solution interface. The resulting arrangement of charges on the solid/ solution interface is known as the *Electric Double Layer (EDL)* [4, 5, 14, 139].

The simplest representation of an electric double layer is a parallel plate capacitor, often attributed to Hermann von Helmholtz. Helmholtz proposed that the counterions in the electrolyte which are in the vicinity of the solid surface bind directly to the surface, in equal magnitude as the surface charge to neutralize it. The two layers of charges, the charged solid surface and the counterions in the ionic solution, then resemble the charge arrangement of a simple parallel plate capacitor. This idealistic arrangement of ions in the electrolyte solution is also called *perfect shielding,* since all of the other ions in the electrolyte solution are shielded from the surface charge. In this arrangement of charges the distance of approach of counterions is limited by their ionic radius. This simplistic model proposed by Helmholtz, also assumes that the electrostatic potential at the surface of the solid drops to the value of bulk electrostatic potential of the ionic solution, over the thickness of the layer of counterions [4, 5, 14, 139].

In reality, at a solid/ ionic solution interface ions in the liquid do not lie in a single plane. Due to finite temperature of a system and thermal motion of ions associated with it, the ions are not fixed at their respective positions as Helmholtz had proposed. This effect of random motion of ions in an ionic solution due to

73

temperature was taken into account in a model independently proposed by Louis George Gouy and David Leonard Chapman [4, 5, 14, 139].

In the Gouy-Chapman model, not all of the ions are confined in a single sheet next to the solid surface, fixed in their respective positions. Instead, the distribution of ions in the ionic solution is such that the density of the charges decreases with distance from the surface. The counterions in the immediate vicinity of a charged surface are under the constant influence of two competitive forces. On one hand is the attractive electrostatic force from the surface charges, pulling the counterions in the ionic solution towards the surface and on the other, is the random thermal motion of the ions. The mixing tendency resulting from the interaction of these two forces leads to a diffused distribution of the counterions. For this reason, only a few of the counterions are close to the surface due to electrostatic force, the remainder being distributed in a spatially probabilistic manner, the distribution of which is given by the Poisson-Boltzmann equation. The counterions in this distribution are diffused in a spatial region. The extent of this spatial region is defined, on one hand by the charged solid surface and on the other by a position in space, where the random thermal motion of the ions is strong enough to overcome the electrostatic attraction. At this 'edge' position the potential energy from the electrostatic attraction is approximately equal to the kinetic thermal energy of the counterions. Farther from this 'edge' position, the thermal energy is dominant and the anions and cations in the electrolyte solution

are in equal distribution. This 'diffused' arrangement of charges does not provide perfect shielding of the surface charge. Or in other words, if there were no random thermal motion of the ions there would be just as many counterions in the electric double layer as needed to balance the surface charge and the electric double layer would collapse to a thin layer, just as Helmholtz had proposed. The potential drop is exponential across this layer, as long as the system is in thermodynamic equilibrium. Although, much more descriptive than the Helmholtz model, even the Gouy-Chapman model is not able to capture the complete picture of electric double layer structure as the Gouy-Chapman model neglects adsorbed ions on the surface, ion-ion interactions, and constant dielectric constant in the interfacial region [4, 5, 14, 139].

The model suggested by Otto Stern and later further developed by David Grahame is more comprehensive and is widely used today. The Gouy-Chapman model reasonably explains the structure of the electric double layer as long as the system is simple and contains symmetric ions. These ions are mobile and will enter or depart the electric double layer owing to their thermal motion as long as the overall charge remains the same. The picture also incorporates the specific adsorption of ions on the solid surface. These ions are attracted to the solid surface by more than electrostatic forces. The driving force for these ions to be attracted to the electric double layer is specific to the surface in nature. The plane going through the center of the specifically adsorbed ions is defined as the inner

Helmholtz plane (IHP) and thus encloses an adsorbed layer of water molecules electrostatically attracted to the solid surface, as well as certain non hydrated surface active species present in the solution, and a few non hydrated counterions adsorbed onto the surface. The spatial extent of this region is known as the inner Helmholtz layer (iHL). Next to the inner Helmholtz layer is another layer of hydrated counterions which are adsorbed to the solid surface. In a similar fashion, the plane going through the mean geometric location of hydrated charge centers due to counterions adsorbed to the solid surface is known as the outer Helmholtz plane (OHP) and the spatial extent of these charge centers is called the outer Helmholtz layer (oHL). The region consisting of inner and outer Helmholtz planes is also called the Stern layer. The ions in the inner and outer Helmholtz layer still do not provide complete shielding of the surface charge. The Stern-Grahame model also incorporates the diffuse layer of the counterions from the Gouy-Chapman model to present a comprehensive picture of the structure of electric double layer. The Stern-Grahame model assumes a linear potential drop from the surface of the solid to the outer Helmholtz plane, as Stern recognized the fact that there is a finite distance from the solid surface to the center of the ion at which the electrical potential distribution starts, and an exponential decay of potential from the outer Helmholtz plane to the bulk electrolyte solution. In addition to this, Stern also understood that the assumption of treating ions as point

charges and the solvent as a structure of constant dielectric permittivity is quite unsatisfactory [4, 5, 14, 139].

In summary, the comprehensive picture of the structure of the electric double layer which emerges from the Helmholtz-Gouy-Chapman-Stern-Grahame model is that it is separated into three layers. The first layer next to the solid surface is at the inner Helmholtz plane and bears the potential Φ_i, where coions and counterions are not hydrated and are specifically adsorbed to the solid surface. The second layer is defined at the outer Helmholtz plane with potential Φ_d, consisting of a layer of bound, hydrated and partially hydrated counterions. Since the shielding of the surface charges is still not perfect by these two layers, there is a third and an outermost layer, composed of 'diffuse' distribution of mobile counterions and coions in which resides the slip plane bearing the ζ potential (described next). The slip plane or hydrodynamic plane of shear is an imaginary plane separating the immobile charged species on the solid surface from the mobile charged species in the solution. Figure 4.1 summarizes the description of the electric double layer structure [14].
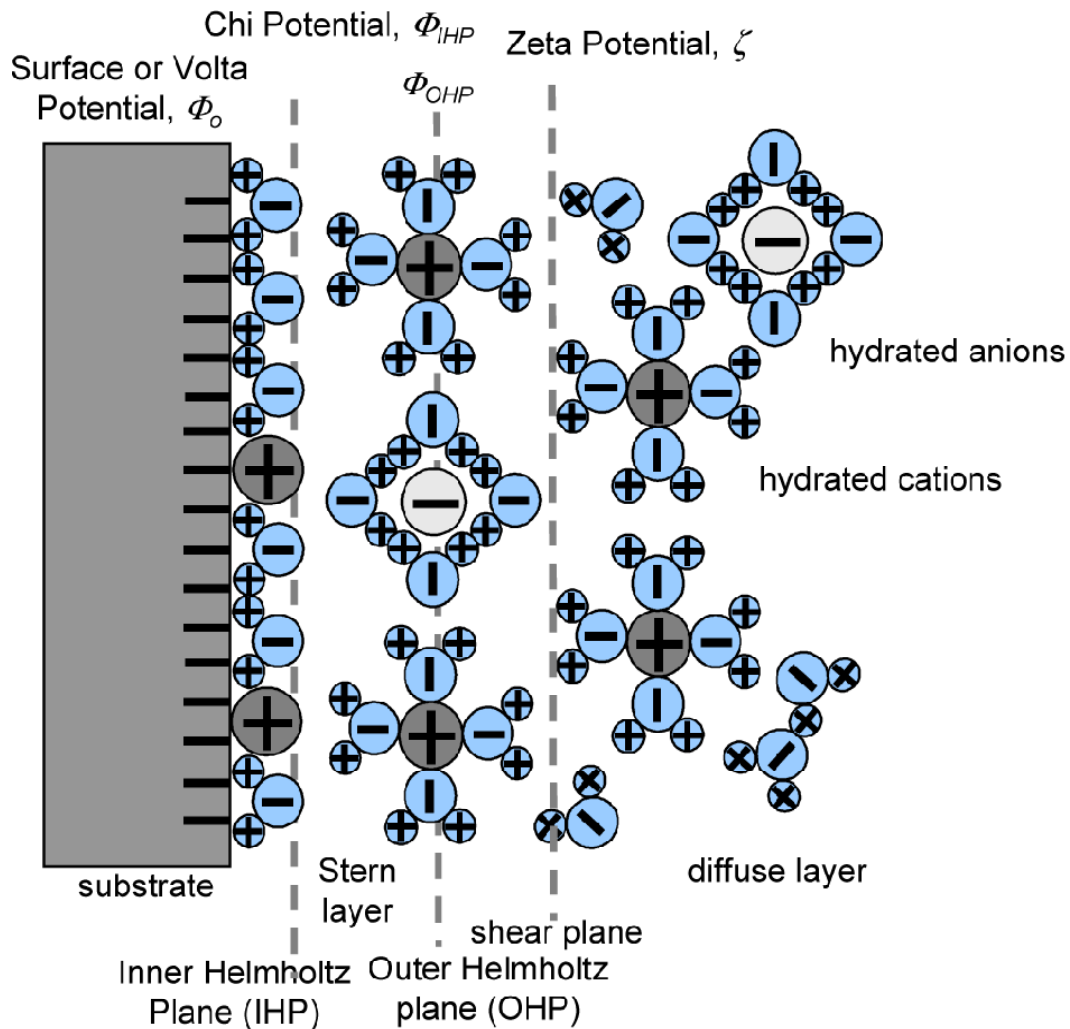
Figure 4.1: Gouy-Chapman-Stern model of the electric double layer developed at the solid/ionic solution interface. The solid surface is illustrated with negative surface potential Φ_o. The figure also shows the inner Helmholtz plane (IHP), consisting of non-hydrated counterions and adsorbed water molecules. The outer Helmholtz plane (OHP) is built up of predominantly hydrated counterions. The inner Helmholtz plane and the outer Helmholtz plane combined form the Stern layer. The diffuse layer is defined beyond the outer Helmholtz plane. The figure also illustrates the slip plane or the hydrodynamic plane of shear which marks the transition between mobile and the immobile ions. Figure from [14].

4.2.1 Width of Electric Double Layer

The overall width of the electric double layer is typically described by a characteristic length called the Debye Length λ_D, which is in the range of 1-300 nm for aqueous electrolyte solutions and for symmetric binary electrolytes it is related to the ion concentration in the bulk solution , η, as follows:

$$\lambda_D = \left(\frac{\varepsilon_r \varepsilon_o RT}{2F^2 z^2 \eta}\right)^{\frac{1}{2}} \tag{3.1}$$

where R is the gas constant, T is the temperature, z is the charge on the ion, ε_r is the relative permittivity of the solution, ε_o is the absolute permittivity and F is the magnitude of electric charge per mole of electrons [139]. At higher ionic concentration the Debye length is of the order of a few nanometers. Due to the large number of counterions next to the solid surface the surface charge is easily neutralized. The Debye length also decreases with increasing valency because fewer ions are required to equilibrate the surface charge. More importantly, the Debye length increases as the square root of absolute temperature which implies that without thermal agitation, the double layer would collapse to an infinitely thin layer. At low ionic concentrations, there are far fewer counterions in the immediate vicinity of the solid surface to neutralize the surface charge and the Debye length extends to hundreds of nanometers into the solution in order to have enough counterions to compensate for the surface charge. In channels and pores with sizes in the micron range the Debye length is significantly smaller than the channel dimensions and the bulk of the solution is shielded from the surface

charge, whereas, in the case of nanopores, the pore dimensions are often comparable to or smaller than the Debye length. Figure 4.2 shows Debye length as a function of molar concentration of aqueous HCl solution calculated using equation (3.1).
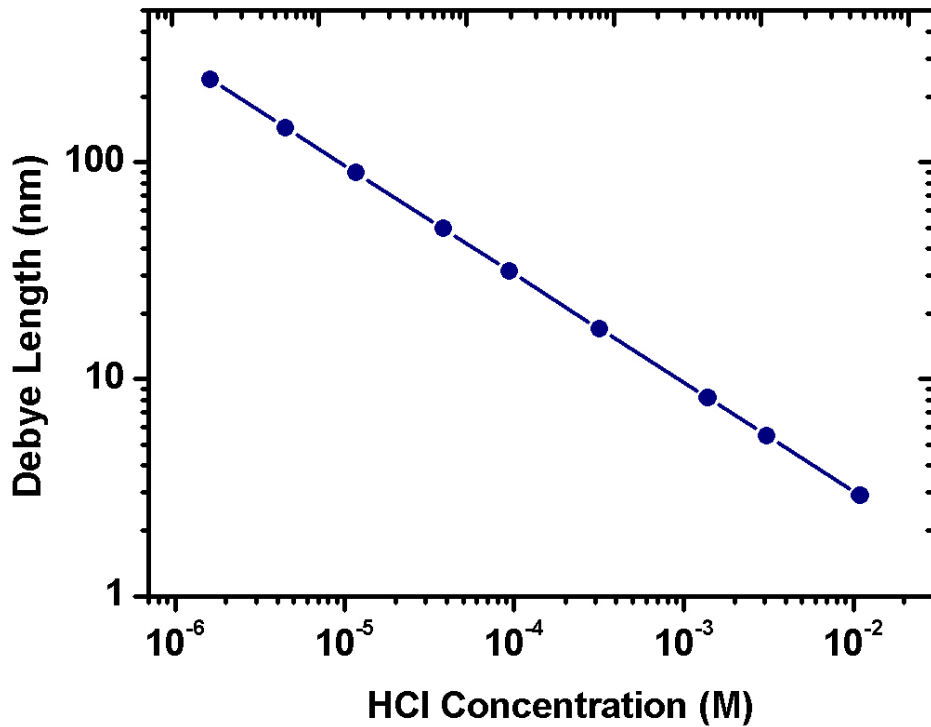
Figure 4.2: Debye length as a function of concentration of aqueous HCl solution. For higher ionic concentration solutions the Debye length is a few nanometers, whereas for solutions with low ionic concentrations, the Debye length extends up to hundreds of nanometers.

4.2.2 Zeta Potential

The picture of the electric double layer which emerges from the above discussion is that the electric double layer is comprised of fixed and mobile charges. Fixed charges are within the spatial region called the Stern layer, based on the Stern model, including the inner and outer Helmholtz layers. Adjacent to the Stern layer is the mobile part of the electric double layer with diffused charge distribution, as borrowed from the Gouy-Chapman model, and is composed of mobile counterions and coions. The spatial boundary between the immobile and mobile charges is an imaginary plane called the slip plane or hydrodynamic plane of shear. Although, neither a discrete slip plane nor a discrete interfacial plane exists, theory is usually based on infinitely sharp transitions. A vast amount of experimental data suggests that the slip plane is situated at some finite distance in the solution. The value of the surface potential measured at this slip plane is called the zeta (ζ) potential. In other words, the zeta potential is defined at the shear plane that identifies the closest region to the solid surface where the motion of ions is still hydrodynamic, as opposed to the outer Helmholtz plane, defining the interface region, where the majority of ions are bound to the surface, forming the fixed Stern layer, and are not expected to slip parallel to the surface. Also, the zeta-potential is defined with reference to an electrostatic zero which is defined as the potential of the region where the local ionic density is unaffected by the surface charge on the solid [1, 139, 156, 157].

4.2.3 Relationship Between Zeta Potential and Surface Charge Density

When the SiO_2 surface of a nanopore comes into contact with an aqueous HCl solution, the surface acquires negative surface charge density due to deprotonation of silanol groups [1]:

$$SiOH \rightleftharpoons SiO^- + H^+ \tag{3.2}$$

The calculation of ionic distributions in the vicinity of a charged solid surface requires solving the Poisson-Boltzmann equation [1, 4, 157]. The ionic distribution near a solid uniformly charged planar surface was studied by Grahame [3] and later the Debye-Huckel approximation was used to study the case of cylindrical geometry [1, 157]. Thus, applying the Poisson-Boltzmann equation and using Grahame's approach for a planar charged surface, the surface charge density of a nanopore surface can be treated as a linear sum of the charge density due to a planar charged surface and a perturbation term due to the cylindrical curvature of the nanopore wall [1, 157]. Also, Behrens and Grier [156] derived a relationship between the zeta (ζ) potential and surface charge density (σ) for silica based on the surface reactivity. An analytical model combining the above two approaches was developed by our collaborators Dr. Alex Smolyanitsky and Dr. Marco Saraniti for the nanopores [157] and was used to obtain the values of zeta potential (ζ) and surface charge density (σ) as a function of HCl solution concentration and are plotted in Figure 4.3.

Figure 4.3 shows the nanopore zeta potential (ζ) and the surface charge density (σ) as a function of HCl concentration. At low ionic concentrations the surface charge density is high due to deprotonated silanol groups, leading to a higher value of zeta potential as well. As the ionic electrolyte concentration starts to increase the surface charge density (σ) and zeta potential (ζ) both reach to zero [157]. At a specific pH, the solid surface is completely neutralized by the counterions from the solution and bears no net charge. This is known as point of zero charge or *isoelectric point*. The isoelectric point for silica is at a pH value of ~2 [158].
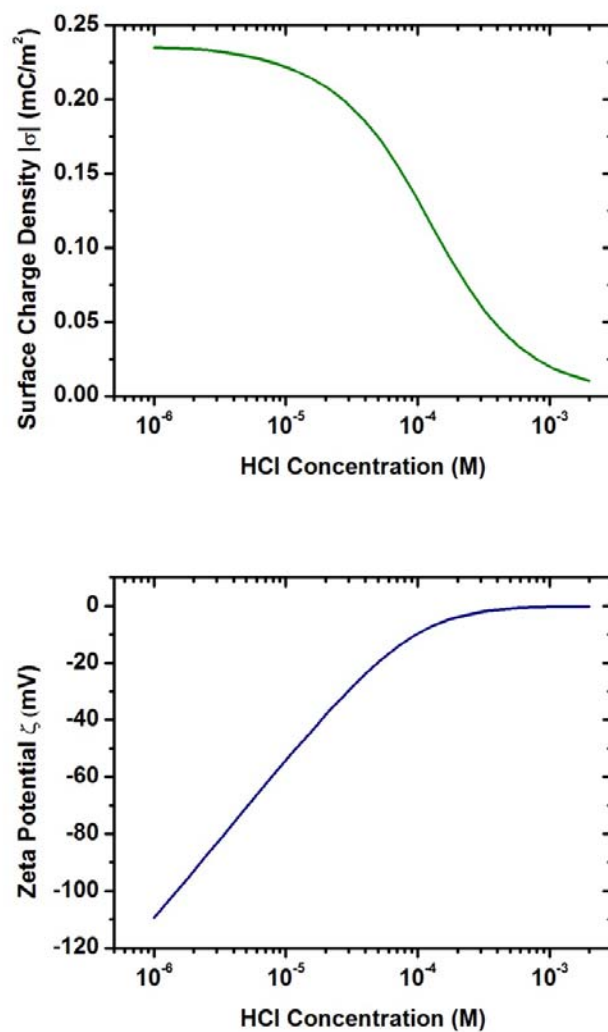
Figure 4.3: SiO$_2$ Surface Charge Density, top plot, (σ) and Zeta Potential (ζ), bottom plot, as a function of aqueous HCl concentration calculated using the analytical model from [157]. At low concentration of ionic solution the surface charge density and the resulting zeta potential is high due to the deprotonated silanol groups. As the concentration of ions in the solution is increased and the surface silanol groups are protonated the surface charge density and zeta potential start to decrease and reach a negligible value.

4.3 Electrical Characterization of Nanopores

4.3.1   Ion Transport Measurements through Nanopores

Nanopores derive their unique ion transport characteristics from the interaction of electric double layers with the nanopore wall surface charge. As noted in the previous section, the quantitative measure of the spatial extent of the 'spread' of electric double layer is given by the Debye length, which depends on the bulk ionic concentration of an ionic solution. The higher the concentrations of ions in a solution, the smaller the electric double layer and shorter the Debye length. On the other hand, the lower the concentration of ions in a solution, the larger the electric double layer and longer the Debye length. This happens because as the bulk ionic concentration in an ionic solution is decreased, more and more counterions within the nanopore volume are required to shield the nanopore surface charge, leading to an extended spread of the counterions in the diffuse layer part of the electric double layer. This simple relationship between the ionic concentration of an ionic solution and the dimensions of an electric double layer, play a large role in understanding the ion transport through nanopores.

For a nanopore of given dimensions, at optimum particular ionic concentration, the Debye length becomes equal to the nanopore radius. At that ionic concentration, the counterionic mobile charge due to the random thermal motion of the ions is practically smeared over the whole of the nanopore cross-section, a process which is often referred to in the literature as *electric double*

layer overlap. Due to this phenomenon, the nanopore as a whole becomes selectively permeable, or *ion permselective* as it is called in literature, to the counterions i.e. the nanopore within its volume enriches and allows passing of counterions and excludes coions. This concurrent enrichment of counterions and exclusions of coions from within a nanopore volume due to the electrostatic interactions between the ions in the solution and surface charge is called the e*xclusion enrichment effect* [4, 5, 13, 15].

In a microfluidics channel, in comparison to the nanopores, the electric double layer with counterionic mobile charge is confined to a very thin layer at the surface, so that the fluid within a microfluidic channel is quasi-electroneutral. Hence, most of the fluid flowing through a microfluidics channel is charge non-selective and does not discriminate between charge transport of counterions and coions.

In order to study ion transport through nanopores, standard current-voltage measurements using an Axopatch 200B low noise amplifier were done because the current-voltage measurements do not require the use of often expensive fluorescent labels. Another benefit of electrical characterization is that these measurements can be integrated on the chip by fabricating the measurement circuitry on a nanopore chip. This allows portability for the whole detection and measurement system. In addition to this, the electrical characterization of the

nanopore systems can be easily parallelized giving a fast, high throughput system for rapid field application.

The ion transport characterization and field effect measurements were performed on arrays of 25 cylindrical, silicon-on-insulator nanopores, with individual pore diameters of 34nm and 95nm because using an array provided enhanced signal to noise ratio of the measured current compared to a single nanopore. Single nanopores were used for the Coulter counting experiments which are discussed in the next chapter. The nanopore chips, prior to mounting on the Teflon holders for measurements were cleaned in 1:1 solution of sulfuric acid and hydrogen peroxide for 15 minutes in a cleanroom environment. In order to perform the ion transport experiments the nanopore chip was sandwiched between two custom-made Teflon chambers filled with electrolyte solution using threaded metal rods with screws. Once the nanopore chip was mounted, the complete holder-chip assembly was degassed in a dessicator to remove air bubbles present in the nanopore. Platinum electrodes used to measure the ionic current were rinsed with deionized water prior to every run of the experiment without any additional chemical treatment. There were two sets of experiments performed to study ion transport through the nanopores. In the first set of experiments, the conductance of a nanopore array as a function of ionic solution concentration was measured. In the second set of experiments, the conductance of a nanopore array was again measured as a function of ionic solution concentration but this time a

voltage bias was applied to the nanopore chip using a Keithly 236 source meter unit to study the modulation of ion transport by application of a chip bias voltage. By measuring the conductance one can observe the effects of interaction between the nanopore wall surface charge and the ions translocating through the nanopores. The conductance measurements were always started with the lowest electrolyte concentration solution first. To exchange the ionic solution, the solution which was just used in the measurement was removed from the Teflon chambers using a pipette and rinsed with nanopure water, and then rinsed with the new ionic solution of higher concentration three times, and finally filled and measured on the fourth turn. This ensured that when the measurement for the next higher concentration solution was actually done, the solution in the nanopore was as close to the desired higher concentration electrolyte solution as possible. This step of rinsing the Teflon chambers prior to measurements was followed for the field effect measurements as well. The conductivity values of ionic solutions were also measured along with the ionic conductances.

Shown in Figure 4.4 is the log-log plot of the conductances of two nanopore arrays of individual pore diameter of 34nm (Black) and 95nm (Orange) respectively, while varying the HCl concentration from ~3 μM to 100mM. For all of the data points presented in Figure 4.4, five measurements were taken and the results averaged. The X- axis on a log scale displays the average values of the ionic concentrations calculated by using the measured conductivity of the ionic

solutions. Similarly, the Y-axis displays the conductance of the nanopore arrays measured using the Axopatch 200B low noise amplifier at different HCl concentrations. By examining this data it can be seen that nanopores of different diameters behave in a similar fashion. At high ionic concentration solutions, the conductance is predicted by the bulk approximation but it soon starts to divert at lower ionic concentration solutions. The larger pores follow the cylindrical theory for lower salt concentrations than the smaller pores. The 34nm pore diameter array starts to diverge from the linear behavior at approximately 300μM HCl concentration, whereas the 95nm pore diameter array deviates from the linear behavior approximately at 20μM HCl concentration. For a given ion concentration, the Debye screening length is fixed, therefore the smaller nanopores will have overlapping double layers before the larger apertures, as can be seen from the earlier divergence in the conductances.

At high ionic strength electrolytes, nanopore conductance can be explained using a simple model which is used to explain the conductance of a cylindrical resistance and is similar to the behavior exhibited by a microfluidics channel. This is because at higher ionic concentrations all the silanol groups at the nanopore wall surface are protonated because there are enough H^+ ions present within the nanopore to shield the surface charge leading to an electric double layer having a Debye length of only a few nanometers.

At low ionic concentration solutions a conductance plateau is observed. When the ionic strength of the solution is low, the electric double layer overlaps inside of the nanopore and the effect of surface charge extends over the whole of the nanopore cross-section more and more and starts to affect the ion transport through the nanopore. This effect can be explained by considering the condition of overall charge neutrality within the nanopore. The surface charge inside a nanopore must be balanced by the counterions, present within the nanopore. The condition of charge neutrality necessitates that the number of mobile counterions far exceeds the number of mobile coions. The nanopore attracts H^+ ions to satisfy the electroneutrality condition, whereas the Cl^- ions are repelled from the nanopore. As the ionic strength of the electrolyte solution is further decreased the emerging unipolar conductance of the nanopore starts to exceed the corresponding bulk ion contribution in the solution. This counterionic conductance reaches a plateau and is independent of the nanopore size as well as the bulk ionic concentration. As a result, at low ionic strength solutions, the presence of excess counterions in the nanopore explains the plateau in the conductance plot suggesting that the surface charge governs the ion transport in nanopores.
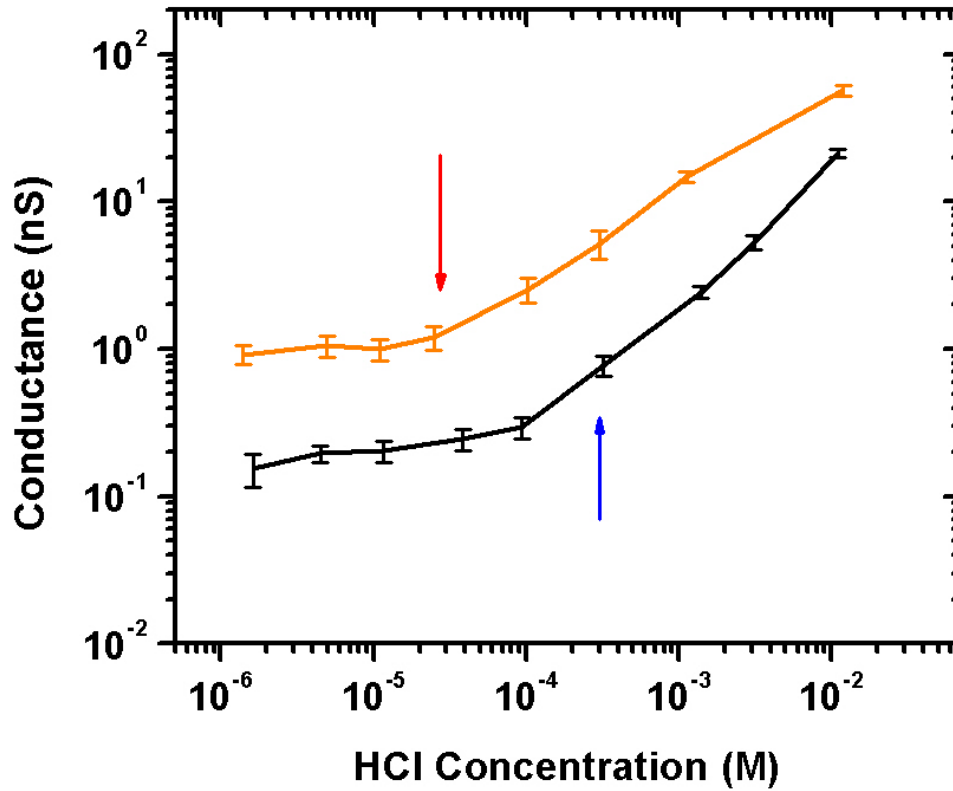
Figure 4.4: Nanopore array conductances as a function of HCl concentration ranging from 3μM to 100mM. The measured nanopore array conductances are shown as solid lines for a gate bias of 0V for 34nm pore diameter array (black) and 95nm pore diameter array (orange). The uncertainty in the conductance is shown as error bars for each measurement point. The vertical arrows mark the HCl concentrations where the Debye length is equal to the radius of a single nanopore. At high solution concentrations, to the right side of both the arrows, the conductivity of the solution in the nanopore is similar to that of the bulk and does not exhibit any nonlinearity due to surface charge effects. At low solution concentrations, to the left of both the arrows, the surface charge starts to affect the ion transportation through the nanopores.

It is clear that the nanopore array conductances display a significant change due to the effects of the nanopore surface charge interaction with the ion transport as the ionic concentration of the solution is gradually decreased. On one end of the observed nanopore conductance phenomena is the complete non charge selective behavior of the nanopores due to a negligible electric double layer with zero surface charge and zeta potential, when filled with high ionic strength solutions. On the other hand is the behavior displayed of unipolar ionic conductors, meaning that the ionic current through the nanopores is predominantly due to counterions, with extended electric double layer overlap, leading to high values of surface charge and zeta potential, when filled with low ionic strength solutions. The electric double layer overlap within nanopores also results in the presence of electric potential from the nanopore surface, over the whole of the nanopore cross-section, allowing the possibility of modulating the surface potential by applying a voltage bias to the nanopore substrate, in a fashion similar to a semiconductor field effect transistor, which is discussed next.

4.3.2 Field Effect Modulation of Ion Transport through Nanopores

A metal-oxide-semiconductor field effect transistor is a transistor that uses a control electrode, *the gate*, to capacitively modulate the conductance of a semiconductor surface channel joining two contacts, *the source* and *the drain*. The gate is separated from the semiconductor body or *substrate*, underlying the

gate by a thin layer of insulator, typically silicon dioxide. When a voltage is applied to the gate electrode it modifies the distribution of charges in the semiconductor substrate. Depending on the polarity of the voltage applied and the type of inherent charge carriers within the semiconductor, a surface channel is formed at the interface between the semiconductor body and the gate insulator consisting of unipolar charge carriers which then can be modulated by varying the gate voltage [159]. This concept is called field effect modulation and is applied here towards the study of ion transport through the nanopore arrays.

Typically, there are three types of charges that can affect the ion transport or ionic conductance in nanopores:

- The charged ions from the ionic solution in the nanopore.
- The localized surface charges at the nanopore walls, either due to adsorption of ions from the electrolyte or due to the dissociation of surface groups.
- Charges external to the system, such as those induced by the field effect.

In the previous section, the effects of interaction surface charge with the ions within the nanopore were discussed. It should be noted again that the effects of the surface charge interaction with the ions within the nanopore are pronounced at low ionic concentration solutions, the first signs of which appear when the Debye length of an electric double layer becomes comparable to the radius of a

nanopore. At that point, the electric double layer starts to overlap resulting in the prevalence of electric potential, of the same sign as the surface potential, over the whole nanopore cross-section. Due to this the nanopore as a whole becomes ion permselective i.e. enriches the counterions within the nanopore volume and excludes the coions. It is this counterion rich unipolar environment within the nanopore with prevalent surface potential in the nanopore that raises the possibility of exploring field effect modulation of ion transport through the nanopores.

The exclusion enrichment effect or permselectivity, as it is referred to in membrane filtration studies [154, 155] was first experimentally investigated using polymer nanoporous membranes. Researchers worked on exploring the possibility of modulating the ion transport through such synthetic sieves. Nishizawa *et al.* [50]., Lee and Martin [39] and Martin *et. al.*[10] developed a gold plating technique to control the size as well as the surface chemistry of the nanopores etched in polycarbonate membranes. These nanopores were etched in polycarbonate substrates using track etch method. The permselectivity of these membranes for anions or cations increased when the Debye length was comparable to the nanopore diameter. The ion permselectvity also depended on the surface charge of the nanopores. Nanopores with positive surface charge demonstrated increased anion flux compared to negatively charged pores while the opposite was true for cations. This further strengthened the idea that the

exclusion enrichment effect was leading to the ion permselectivity of the nanopores and can be successfully exploited to manipulate the ion transport at the nanometer scale. Similar results of the field effect modulation of ion transport through nanochannels using external electrodes were also demonstrated by other researchers [17]. Karnik *et al.* [8, 9] and Fan *et al.* [2] demonstrated that a gate electrode on nanochannels can be used to change their surface charge, enabling field effect control of the ions.

Despite the significant number of studies on the control of the ionic current via an external field, little is known about the efficiency of the modulation of the ionic current via the electrostatic gate. Although a transconductance value is reported by Nam *et al.* [49], it would be interesting to directly determine the change in surface charge on the inside of the channel versus the applied gate voltage. Such an effort requires both a simulation of the expected change in surface charge as well as an experimental study on the efficiency of the electrostatic gate control.

To establish a well-controlled electric field via an electrostatic gate in a nanopore structure, it is necessary to position the gate electrode in close proximity to the nanochannel and ensure that the electrode has the same symmetry as the channel itself. An electrode geometry like this was first demonstrated by Nam *et al.*[49], however, without a dielectric insulator between gate electrode and channel itself, the capacitance between the gate and the ion-conducting channel is

substantial, as is the leakage current. In the approach undertaken in this study thermal oxidation was employed to create an insulating layer that separates the conductive top silicon layer from the pore volume. By using the top silicon layer as the electrostatic gate, the surface charge inside the nanopore could be controlled via the potential applied directly to the silicon. Using an array of nanopores for the experiments the total conductance could be substantially increased with improvement in the signal-to-noise ratio compared to using single nanopores, which is especially beneficial when measuring ionic currents at low ionic concentration solutions. The experimental observations are complemented by a numerical model for the ion transport though the pore based on Brownian dynamics (BD). This allows us to correlate the bias voltage required in the experiments with the theoretical value that is necessary to accomplish a change in the nanopore array conductance for a given electrolyte concentration. Furthermore, the BD model provides valuable insight into the dominant current transport mechanisms at low electrolyte concentrations while taking into account the electric field fringing effects at the nanopore extremities. The BD model is scalable, allowing it to be applied to nanopores with smaller dimensions and different ionic concentrations.
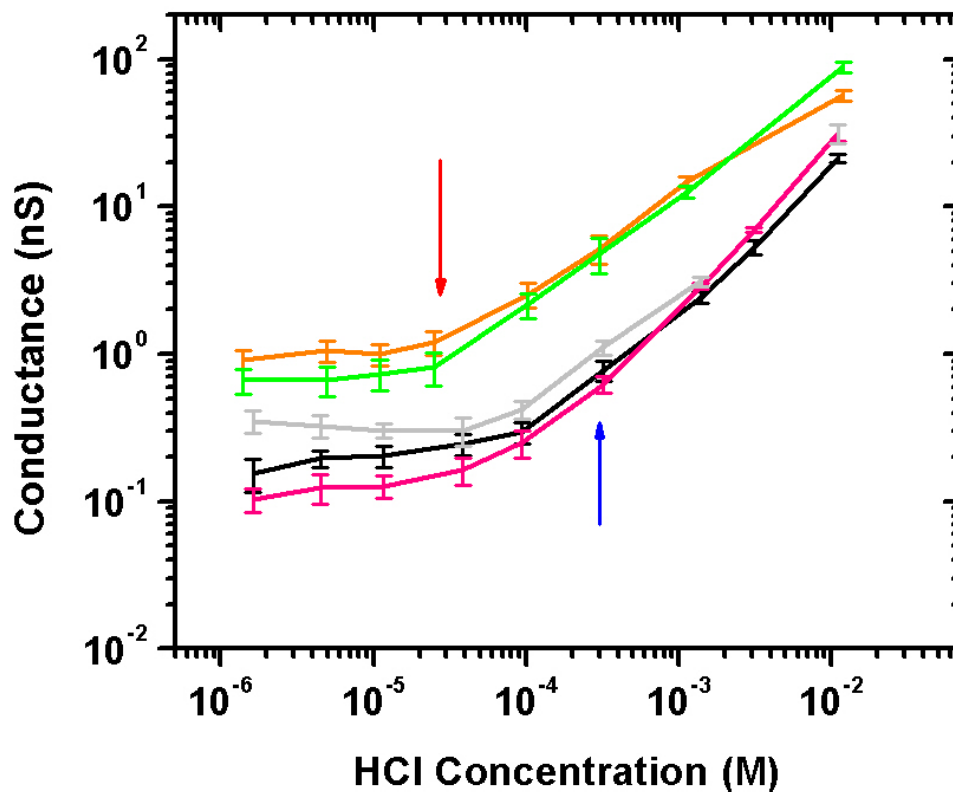
Figure 4.5: Field effect modulation of nanopore array conductances as a function of HCl concentration. The measured array conductances are shown as solid lines for gate bias of 0V for 34nm pore diameter (black), and 95nm pore diameter (Orange). For   +10V bias the conductances are in green for 95nm pore diameter and purple for 34nm pore diameter. Conductance of 34nm pore diameter array was also measured at a bias of -1V (grey). The uncertainty in the conductance is shown as error bars for each measurement point. The vertical arrows mark the HCl concentrations where the Debye length is equal to the radius of a single nanopore.

Figure 4.5 shows the conductance of the arrays as a function of HCl concentration for the different bias voltages for both the 34nm diameter pore array

and the 95nm pore array. For all of the data points presented in Figure 5, five measurements were taken and the results averaged. The error bars indicate the typical standard deviation between nominally identical measurements. To investigate the influence of surface charge as well as the effect of a DC voltage bias applied to the substrate on the ionic conductance, a voltage of V_{SOI}, of 0V, +10V and −1V was applied to the SOI layer on both of the nanopore arrays.

At higher bulk ionic concentrations, concentrations greater than 10^{-4}M, the EDL is thin and the ionic conductance depends only on the cylindrical volume nanopore geometry and the bulk concentration i.e. the concentration of electrolyte filling the baths. Also, the conductance in this concentration range ($> 10^{-4}$M) is unaffected by the bias applied to the SOI substrate.

On the other hand, at low bulk ionic concentrations, concentrations less than 10^{-4}M, the conductance of the nanopores starts to deviate from the bulk behavior. This deviation can be explained by a unipolar conduction model based on the effect of nanopore surface charge. As the counter-ions accumulate in the nanopores, the EDL becomes comparable to the nanopore dimensions and starts to overlap. In this regime the surface charge governed transport dominates the conduction mechanism and significantly influences the conductance of the nanopore array. The oxide-covered inner surface of the nanopores in the array are negatively charged due to the presence of dissociated silanol groups which repel Cl^- ions from within the nanopores, leaving H^+ ions as the majority ions

contributing to the ionic current flow at low HCl concentration and for V_{SOI}=0V. When a positive bias is applied to the nanopore SOI layer, at low electrolyte concentrations, it depletes the H^+ ions within the array and effectively decreases the ionic current. Likewise, a negative substrate bias attracts additional H^+ ions and the pore conductance is increased. A +10 V bias reduces the conductance at low HCl concentration by a factor of two while the conductance can be increased by a factor of 2-3x with just a -1V bias. This asymmetry is attributed to the rectifying nature of the current flowing between the substrate and the HCl electrolyte, with a negative substrate bias being much more effective at modifying the surface potential at the interface between the electrolyte and the $Si:SiO_2$.

In order to prevent the substrate bias voltage reaching the breakdown voltage of oxide in the SOI substrate, the leakage current through the substrate was also monitored. At low electrolyte concentrations, the leakage current flowing from the SOI layer to the HCl electrolyte can exceed the current flowing through the nanopore itself. Figure 4.6 shows the absolute value of the leakage current flowing out of the SOI substrate as a function of the applied substrate bias.
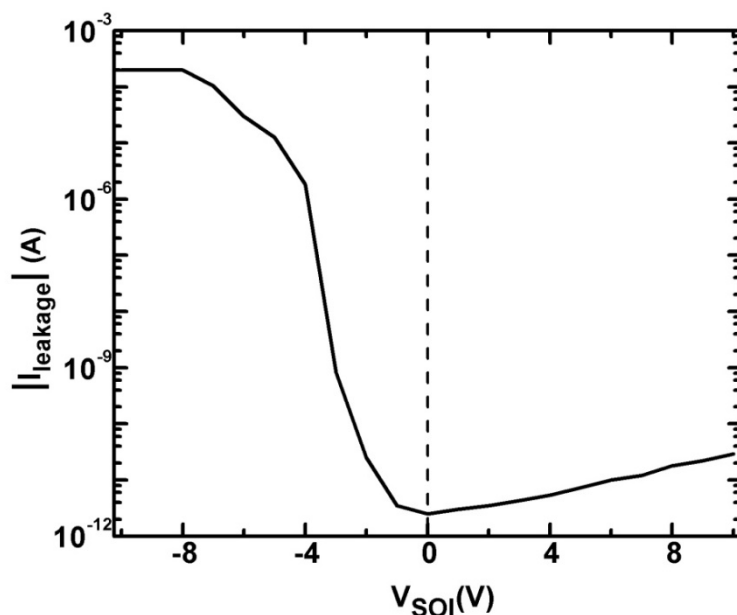
Figure 4.6: The leakage current flowing into the SOI substrate as a function of substrate bias at 10μM HCl.

Positive gate biases of up to +10V can be applied to the substrate before the substrate current exceeds the current flowing through the nanopore array itself. In contrast, the substrate current grows rapidly when a negative bias is applied and we are therefore limited to small magnitude negative bias voltages up to -1V. This asymmetry in leakage current is attributed to the applied voltage dependent conductivity of SiO_2 [54].

To identify the transport mechanisms contributing to the ionic conductance of the nanopore arrays, a 3D Brownian dynamics (BD) simulation has been performed [157]. The use of BD, being a particle-based simulation

100

framework, is motivated by its accuracy, compared to continuum-based models, such as Poisson-Nernst-Planck (PNP) formalism [157, 160], and numerical efficiency compared to Molecular dynamics. Also, Brownian dynamics is capable of reproducing excluded ionic volume effects on complex, non-periodic computational domains (as compared to continuum-based models). Electric field fringing effects at the nanopore extremities are also taken into account. Brownian dynamics furthermore allows simulating the ionic distribution in nanopores and nanochannels with smaller diameters than those used in this study. This is of relevance if pores are being studied that have diameters that approach the Debye length of electrolytes in physiologically relevant concentrations.

The surface charge density was obtained from the model mentioned in , with the assumption that the gate bias does not modify its value significantly. This value was then used as an input parameter to the Brownian dynamics simulation, setting a constant charge density on the wall of the simulated nanopore for each HCl concentration. The pore conductances extracted from the BD simulations are compared with the experimental data in Figure 4.7.
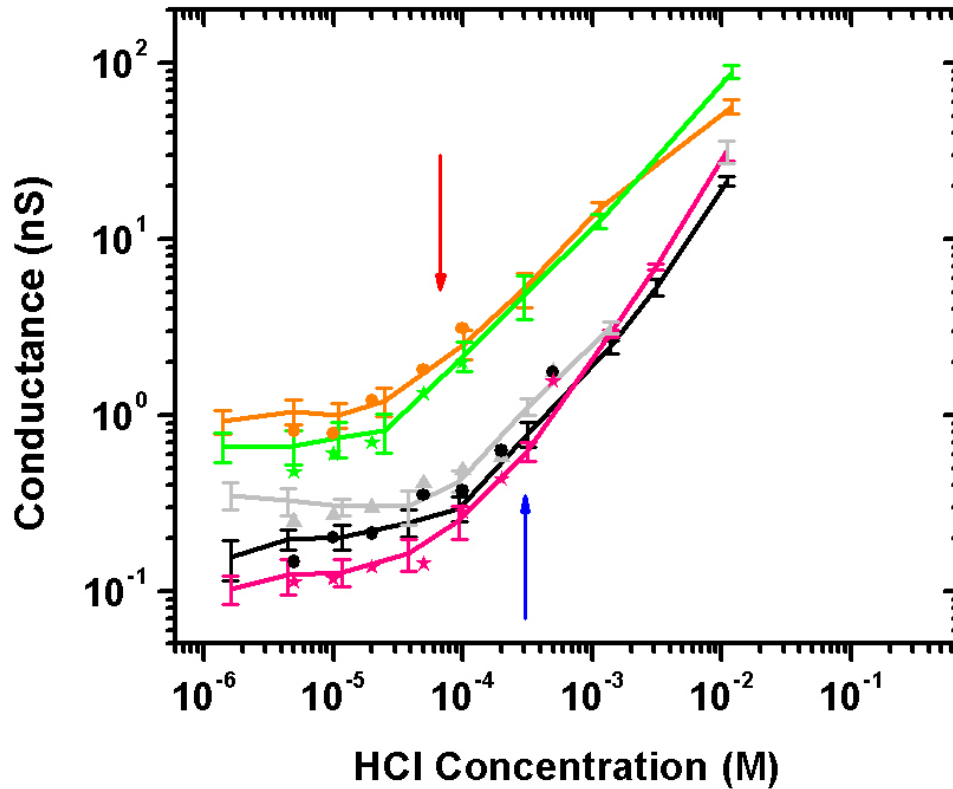
Figure 4.7: Field effect modulation of nanopore array conductances as a function of HCl concentration. The measured array conductances are shown as solid lines for gate bias of 0V for 34nm pore diameter (black), and 95nm pore diameter (Orange). For +10V bias the conductances are in (green) for 95nm pore diameter and purple for 34nm pore diameter. Conductance of 34nm pore diameter array was also measured at a bias of -1V (grey). The uncertainty in the conductance is shown as error bars for each measurement point. The vertical arrows mark the HCl concentrations where the Debye length is equal to the radius of a single nanopore. The simulated nanopore array conductances are shown as scatter points. For 95nm diameter pores the simulated biases are floating ~0V (Orange circles) and +0.5V (Green Stars). For 34nm diameter pores the simulated biases are floating ~0V (Black circles), -0.5V (Grey Triangles) and +0.3V (purple).

102

BD simulations reproduce the saturation in conductance at low HCl concentrations and the gating effect of substrate bias. The substrate bias used in the BD simulations to reproduce the measured data is significantly lower than the values used for the measurements. This is attributed to the fact that the BD simulations modify the Fermi potential within the silicon by the amount of the applied bias, while the bias applied to the electrodes on the silicon layer is being partially screened by charges present in the volume of the SiO_2 layer as well as by the surface states present at the oxide-electrolyte interface [157]. By comparing the bias applied in the BD simulation to that used in the experiments, an efficiency of the applied potential can be derived, which enables us to predict the controllability of the electrolytic current through the nanopore array.

The BD simulations allow visualization of the pore characteristics that may provide useful insight into their behavior for example as biosensors. Figure 4.8 shows the cation and anion concentration distribution along a plane at the midway point of the nanopore when the substrate is floating and when it is raised to a bias of +0.5V. It is clear from Figure 4.8 that for a bulk concentration of 50 μM the H^+ concentration in the pore is reduced by the applied bias, but any change in the anion concentration is less apparent.

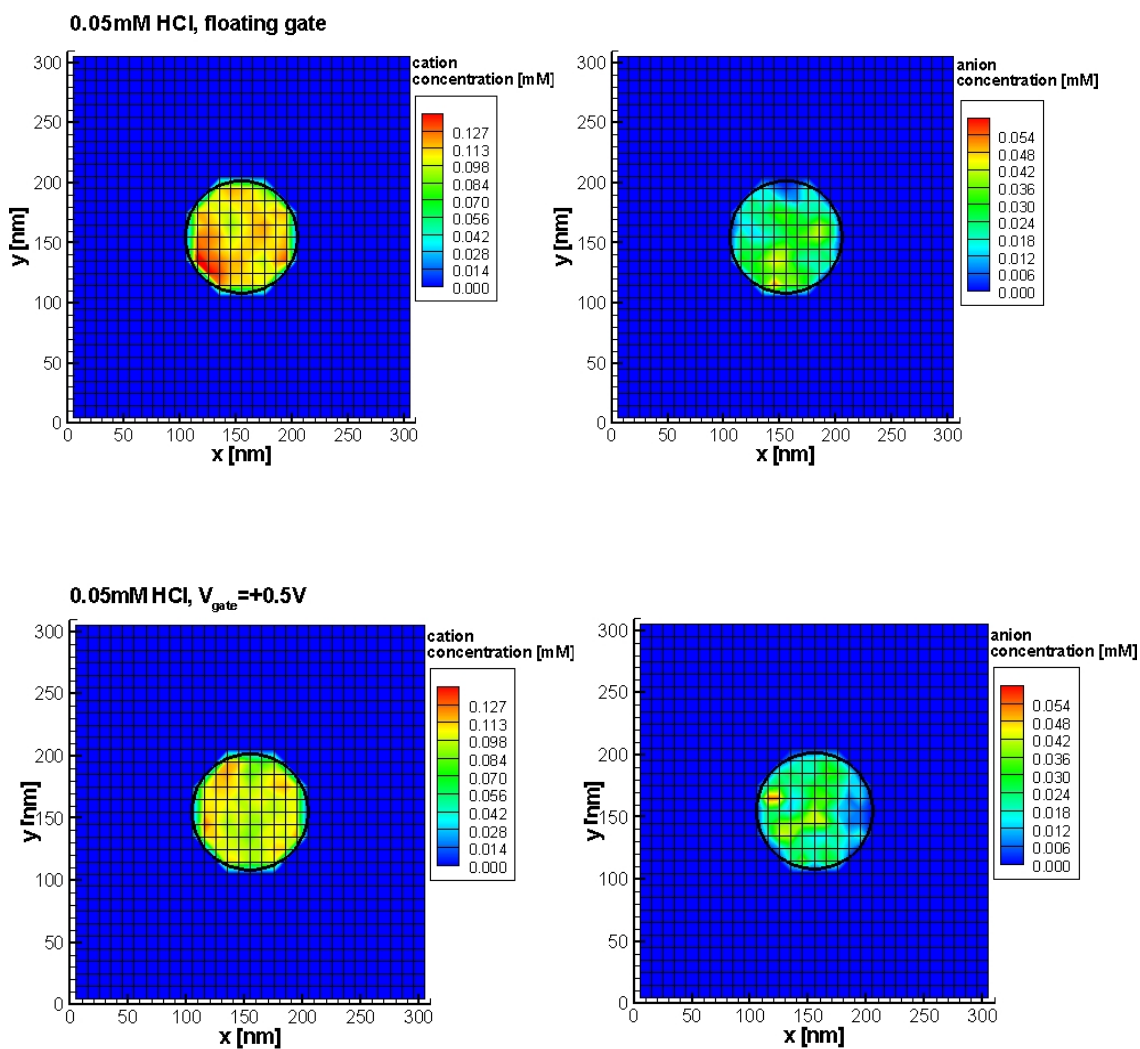Figure 4.8: Distribution of the ion concentration across a 100 nm diameter pore for a bulk HCl concentration of 50 μM, corresponding to the floating gate (top) and the gate bias of +0.5 V (bottom).

To further improve the numerical statistics the anion and cation concentrations were averaged across the pore diameter from all 32 cross-sections along the pore that are far enough away from the openings that fringing fields to

104

do not play a role. The results are shown in Figure 4.9, as radial ionic distributions across a 100 nm diameter pore. The larger diameter has been chosen to improve the statistics of the ionic trajectories within the pore. The qualitative aspects of the discussion that follows are equally applicable to smaller diameter nanopore arrays. The accumulation of cations inside the nanopore is attributed to the surface charge, causing the nanopore to act like an electrostatic pump. At 5.0μM of HCl, the value of surface charge is calculated to be -0.23mC/m^2 [157] giving a Debye screening length of ~136 nm, and the pore is expected to be filled by protons only, as supported by the simulation results in Figure 4.9 (a). For 50μM in Figure 4.9 (b), the surface charge is -0.16 mC/m^2, and the Debye length is ~40 nm, which is comparable to the nanopore radius, and the ionic population is expected to be mostly cationic, although the anion population is non-zero (unlike the case at 5 μM) and peaks in the center of the pore. At an HCl bath concentration of 500μM in Figure 4.9 (c) the population of anions and cations is equal and uniformly distributed across the pore.

Applying a positive gate bias modifies the nanopore surface potential, causing the cationic population to decrease and the population of anions to marginally increase at low concentrations. For a bulk HCl concentration of 50 μM a bias of +0.5 V reduces the H$^+$ concentration at the surface of the nanopore by approximately a factor of two while the concentration at the center of the pore does not change noticeably with bias. For a bulk HCl concentration of 5 μM the

H$^+$ concentration is reduced by a factor of ~2 across the entire diameter of the pore reflecting the complete overlap of the double layers. At a bulk concentration of 50 μM the application of a +0.5V bias increases the anionic population, however, this does not contribute considerably to the conductance, as the Cl$^-$ mobility is about 25% of the H$^+$ mobility in water [161], resulting in the overall decrease of nanopore conductance. Toward higher bulk HCl concentration, the nanopore surface in absence of a bias voltage is close to neutral, causing both anions and cations to equally contribute to the conduction process, and applying a gate voltage does not noticeably modify the ionic populations, or the pore conductance, as shown in Figure 4.9 (c).
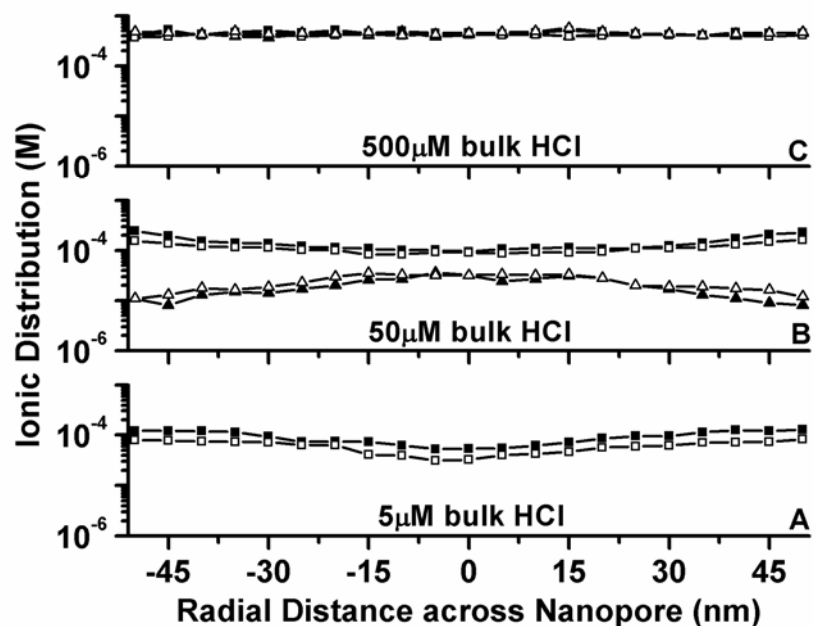
Figure 4.9: The simulated radial ionic distributions across a 100 nm diameter pore for 5μM, 50μM and 500μM HCl concentration. The solid squares (■) show the cationic distribution while the solid triangles (▲) show the anionic distribution for floating gate electrode whereas the open squares (□) and open triangles (Δ) show the cationic and anionic distribution, for a gate bias of +0.5V, respectively. At the concentration of 5μM, the nanopore has a unipolar environment due to double layer overlap and is filled with cations only, leading to pronounced field effect modulation of cation distribution. The anion polpulation in the pore at an HCl concentration of 5 mM is zero and hence only the cation distribution is shown in the pane (A). At the concentration of 500μM, the electric double layers are small compared to the pore diameter, resulting in equal distributions of cations and anions and an absence of field effect modulation of ionic distribution within the nanopores.

4.4 Conclusion

In summary, this chapter discusses the main physical phenomena which affect the ion transport through the nanopores and the field effect modulation of ionic conductance of 25 cylindrical, high aspect ratio nanopores with diameters of 34nm and 95nm fabricated in silicon-on-insulator substrates. Field effect modulation of the conductance of both pore arrays was observed for HCl concentrations below ~ 0.1 mM. A 3D Brownian dynamics simulation of the pores reproduced the trends in order to identify the transport mechanisms contributing to the ionic conductance of the nanopore arrays as well as the bias potential needed to accomplish a change in the pore conductance.

5.   COULTER COUNTING

5.1 Introduction

The Coulter counter is a commercially available device used to count red blood cells and other particles suspended in a conducting fluid. The device was invented by Wallace H. Coulter in 1948 and was subsequently patented in 1953 [55]. Coulter counters operate on a simple principle of resistive pulse sensing and are capable of detecting particles with diameters in the wide range of 0.4μm to 1200μm by using apertures of different sizes. The attributes offered by fabricated solid state nanopores such as precise control of geometry, chemical, mechanical, electrical and thermal robustness and stability, and the ease of integration with standard electronic circuits have made them a viable candidate for usage in high throughput nanoscale Coulter counting applications.

The fundamental operating principle of Coulter counters relies on using a small aperture to connect two fluidic chambers filled with conducting liquid. When a voltage is applied across an aperture the ions in the solution move towards cathode or anode depending on their charge, due to the electric field resulting from the applied voltage. This movement of ions through the aperture due to applied voltage constitutes ionic current through the aperture. When a non conducting particle flows through the ionic solution filled aperture, it displaces a volume of electrolyte equivalent to its own volume. This leads to a drop in the measured ionic current through the aperture for the duration of the particle

109

passing through the aperture. The drop in current or increase in the electrical voltage drop across the aperture leads to an increase in the electrical resistance of the aperture temporarily which then can be measured and used to sense a particle of given type. This is called as Resistive Pulse Sensing or Coulter principle, or Coulter counting.

A previous chapter of this document presented the effect of biasing on the ion transport through nanopore arrays. This chapter presents the results of Coulter counting experiments through a single nanopore with and without the effects of biasing.

5.2 Theoretical background

To calculate the expected increase in resistance due to the presence of an additional particle, initial approximations were developed that were sufficient in specific conditions, but insufficient overall. The first approach towards these approximations was taken by James Clarke Maxwell and was presented in his seminal work, *A Treatise on Electricity and Magnetism* published in 1873 [70]. In his work Maxwell approximated change in resistance due to addition of a spherical particle, referred to as particle here after, in an aperture, as a change in the effective resistivity of the solution as a function of the volume fraction. Considering a cylindrical pore of length L and diameter D filled with an ionic

solution with resistivity ρ, the electrical resistance of the pore when it is completely filled with ionic solution can be calculated as follows:

$$R = 4\rho L / \pi D^2 \quad (5.1)$$

where L>> D. To compensate for the addition of a particle with a diameter d to the system, the resistivity was modified to:

$$\rho_{eff} = \rho(1 + \frac{3}{2}f + ...) \quad (5.2)$$

where f represents the volume fraction occupied by the particle. The volume fraction of the particle is given by the following equation:

$$f = 2d^3 / 3D^2 L \quad (5.3)$$

If the diameter of the particle is much smaller than the diameter of the pore i.e. $d << D$ (thus the pore surface is far from the particle), then Maxwell's model can be applied and the electrical resistance of the pore containing a non-conducting sphere can be obtained as follows:

$$R' = (4\rho L / \pi D^2)(1 + \frac{d^3}{LD^2} + ...) \quad (5.4)$$

Therefore, increase in resistance of the pore due to presence of a non conducting particle is then given by the following equation:

$$\Delta R = R' - R = 4\rho d^3 / \pi D^4 \quad (5.5)$$

In the above equation, the change in resistance ΔR is a function of the solution resistivity, diameter of the spherical particle and the diameter of the cylindrical pore. Therefore, for a solution of given resistivity either d or D can be found if one of the two variable is fixed.

The relative change of pore resistance is therefore,

$$\Delta R / R = d^3 / D^2 L \quad (5.6)$$

In normal operation of resistive pulse sensing, the ionic current through the aperture is continuously measured to observe the translocation of the particles suspended in the ionic solution. This current then serves as a baseline current I_o for a given applied voltage bias and solution resistivity. When a particle passes through the aperture, the baseline ionic current through the aperture decreases and can be calculated as follows [70]:

$$\frac{\Delta I}{I_o} = d^3/(L * D^2) \quad (5.7)$$

5.3 Experimental Procedure

The procedure to prepare solutions of nanoparticles for use in Coulter counting experiment was followed using methods as reported by Sun and Crooks [122]. The main steps of the procedure are preparation of base ionic solution, addition of non-ionic surfactant in the solution and finally the addition of supplied nanoparticle solution.

HCl solutions of concentrations 100mM and 10mM were prepared using Nanopore™ water. Typically, 125mL of nanoparticle bead solution was prepared at a time to prevent contamination of the ionic solution. In order to prepare the bead solution, Nanopure™ water was placed on a magnetic stirrer with a Teflon® stir rod at 1500RPM and required amount of hydrochloric acid added to achieve the desired ionic concentration in the solution. The conductivity of the solution was measured before adding surfactant. 125μL of Triton X-100 (Sigma Aldrich Chemical) was then added to the freshly prepared ionic solution. The non ionic surfactant prevents nanopartices from agglomerating within the solution. The final step in nanoparticle solution preparation was addition of polystyrene beads into the ionic solution. Before adding the beads to the ionic solution, the stock solution from Bangs laboratories was sonnicated for a minimum of five hours to ensure dispersion of polystyrene beads. The targeted final concentration

of nanoparticles in the solution was 5×10^{11} particles/ ml, to remain consistent with the procedure reported by Sun *et al.* [122] Nanoparticle solution was ordered from Bangs Laboratories, Fishers, IN in 5ml dilution containing 1.050 g/ ml concentration of polystyrene beads with mean diameter of 60 nm ± 6 nm. Nanoparticle solutions were bottled and capped under argon and stored in refrigerator. Before running Coulter counting experiments, the nanoparticle solution was brought to room temperature and sonnnicate for a minimum of five hours to ensure monodisperse solution of nanoparticles.

In order to assess the variation in diameter of the polystyrene beads, nanoparticle solution was analyzed using Nicomp 380 ZLS particle sizer. The particle sizer reported a mean diameter of 62 nm for the polystyrene beads used (data not shown). Another experiment performed with the particle sizer was to determine the duration of sonnication required to ensure monodispersion of polystyrene baeds. Based on these characterization experiments, the nanoparticle solution were sonnicated for a duration of a minimum of five hours prior to Coulter counting experiments.

For Coulter counting application individual nanopore of diameter 105nm was used. The ionic transport through the nanopore was thoroughly characterized and was found to be in accordance with the results seen for nanopore arrays. The nanopore was then used for Coulter counting experiments. pClamp 9.0, the proprietary software from Molecular devices to control Axopatch 200B and

Digidata 1320 was used for data acquisition. The applied potential waveform range was from 0mV-70mV with 5mV increments and current was sampled for 20 seconds at 50 kHz for every voltage using the setup described in chapter 3.

5.4 Experimental Results

Presented are the results of translocation, referred to as Coulter counting here after, of 62 nm polystyrene beads through 105 nm diameter single nanopore. The purpose of this experimental sequence is to pass 62 nm polystyrene beads and quantify the magnitude of resulting ΔI. The 105nm diameter nanopore was mounted on the Teflon holder assembly as described elsewhere in the document. The Teflon chambers were then filled with monodispersed polystyrene bead solution prepared in 10mM HCl solution. Once filled the resistance of the nanopore was measured and compared to the previous values.

Figure 5.1 (top panel) presents the current vs. time traces produced as a result of a complete voltage sweep from 0mV to 70mV with a voltage increment of 5mV for 105 nm nanopore filled with monodispersed polystyrene beads in 10mM aqueous HCl solution. The nanopore chip in this case is not biased. The bottom panel of figure 5.1 focuses on the current traces generated by 50mV, 55mV, 60mV, 65mV, and 70mV.

The previous chapter analyzed the flow of ions in an array of nanopores in the presence of a voltage bias applied across the nanopore chip as well as applied

115

to the nanopore chip. A similar, albeit, more complicated scenario arises when a colloidal particle with a surface charge immersed in an aqueous ionic solution is subjected to an external electric field. In this case, the particle is also susceptible to move in response to the applied electric field, and a relative motion between the particle and the ionic solution is developed. When an electric field is applied to a suspension of charged particles, the particles migrate along the electric field lines owing to the presence of surface charge on the particles. When dispersed in an aqueous ionic solution polystyrene beads tend to acquire a surface charge due to dissociation of surface carboxyl –COOH groups as per the following reaction:

$$COOH \rightarrow COO^- + H^+$$

leading to a negatively charged polystyrene surface. As the polystyrene beads come closer to the nanopore they are pushed into the nanopore due to the applied bias and as the polystyrene beads pass, their translocation is registered as a drop in the measured ionic current which is visible as downward spikes in the current vs. time trace.
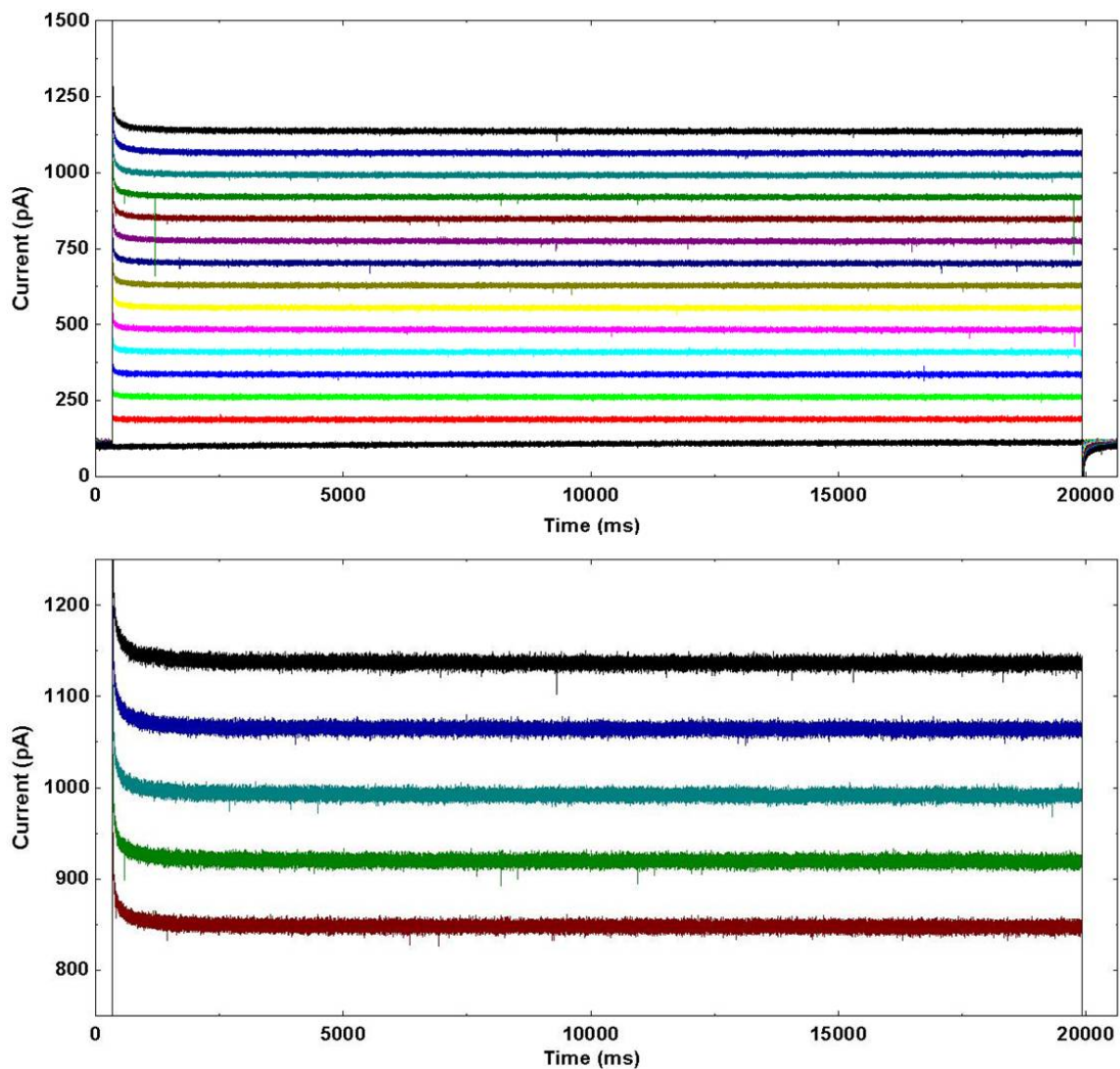
Figure 5.1 shows the results of Coulter counting experiment at 0V gate bias. The voltage applied across the nanopore was swept from 0mV to 70mV and few Coulter counting events are seen.

At a gate bias or nanopore chip bias of 0V very few Coulter events were seen in the voltage sweep. After doing Coulter counting experiments with 0V bias to the nanopore chip, the experiments were repeated with a +10V bias to the nanopore chip. Results are shown in Figure 5.2

Figure 5.2 Complete voltage sweep from 0mV-70mV at an increment of 5mV for 10V gate bias for 10mM HCl solution (top panel). Current traces for voltages 50mV, 55mV, 60mV, 65mV and 70mV showing significantly higher number of bead translocation events compared to 0V bias case (bottom panel).

118

When positive gate bias voltage of +10V was applied more and more charged polystyrene beads were electrophoretically driven to the nanopore [75] leading to an increased number of charged polystyrene beads coming towards the nanopore.

The experiment was repeated for polystyrene beads monodispersed in 100mM aqueous HCl solution with 0V bias and +10V bias. Results are shown in Figure 5.3. There were considerably more events for 0V bias at 100mM HCl solution compared to 10mM solution. In the beginning of the sweep very few Coulter events are seen but as the voltages in the sweep increase more and more polystyrene beads are attracted towards the nanopore resulting in translocating events. Figure 5.3 (middle panel) plots out current vs. time traces for 50mV, 55mV, 60mV, 65mV, and 70m showing numerous events. In order to understand the nature of current spikes, the current trace resulting due to 70mV of applied bias is plotted separately in the following figure (Figure 5.3 bottom panel).

The figure reveals current spikes of different magnitudes. The larger current spikes correspond to the actual translocation events where a polystyrene bead passes through the nanopore. The smaller current pikes are generated because of the beads attempts to pass through the nanopore. As a polystyrene bead comes closer to the nanopore opening sometimes due to the motion the bead does not enter the nanopore right away. Instead, the bead ends up partially blocking the nanopore for a short duration and rebounding before it enters the nanopore. A similar plot for the case of +10V gate bias is also plotted Figure 5.4.
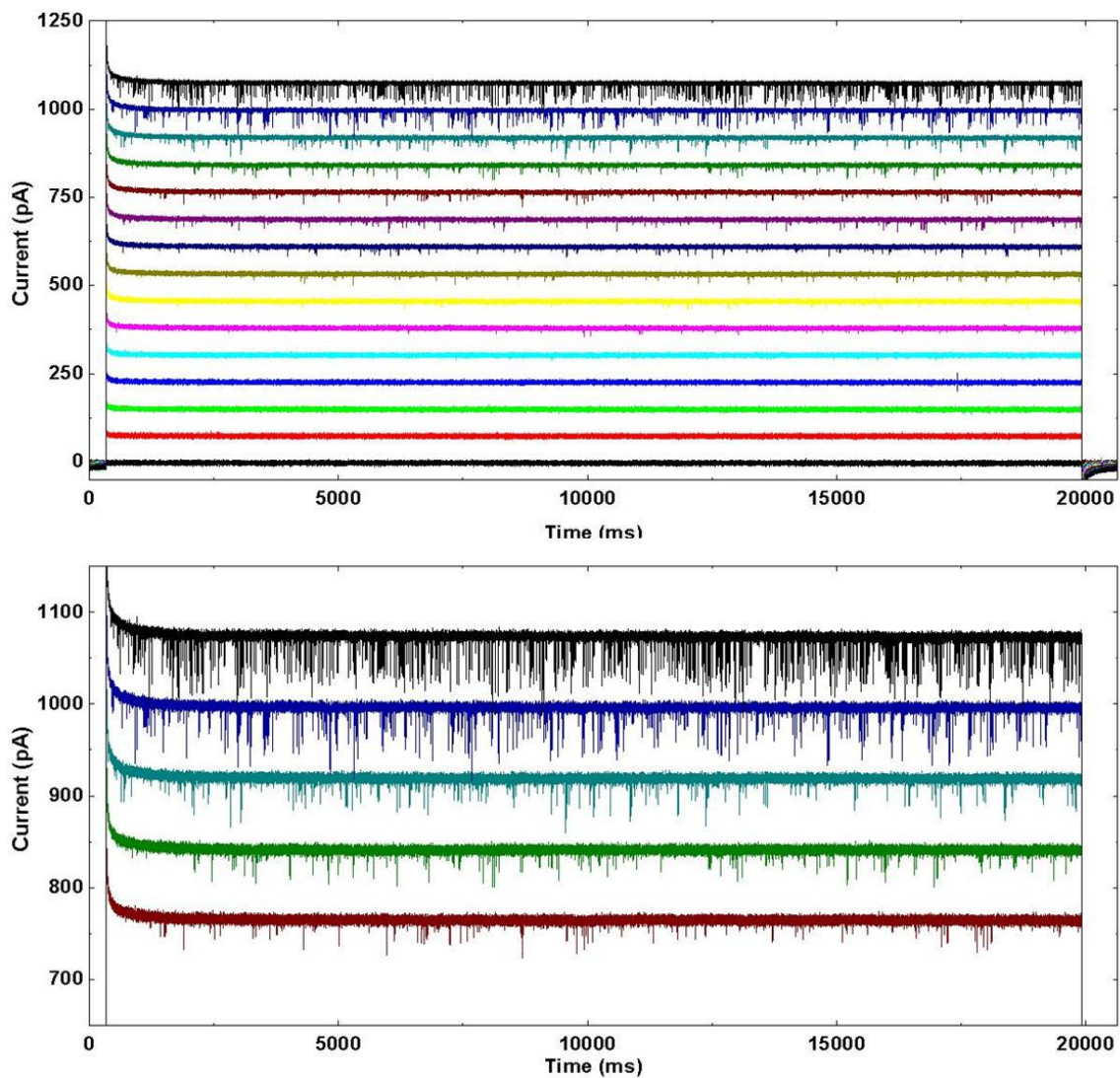
119
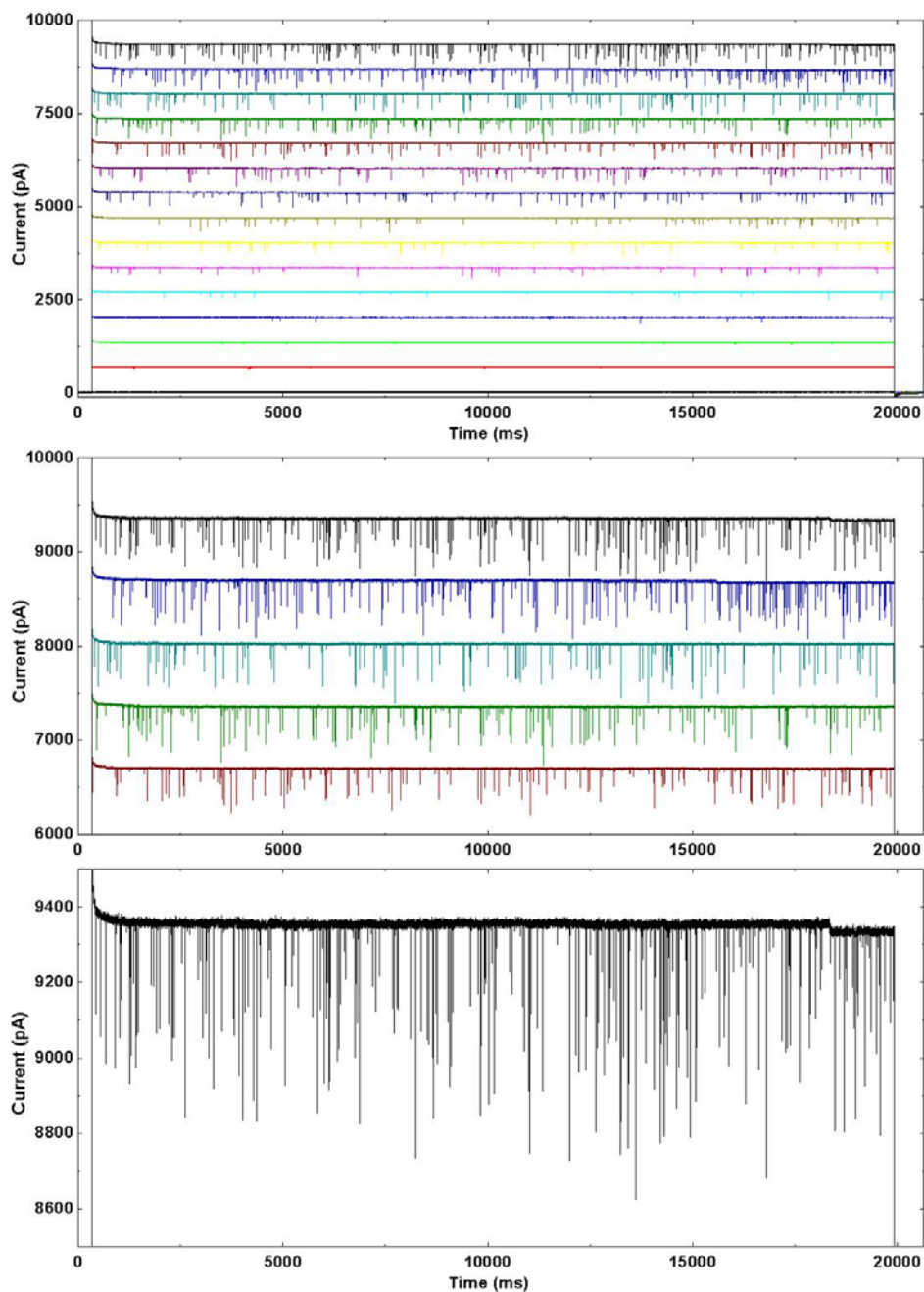
Figure 5.3 Complete voltage sweeps from 0mV-70mV at an increment of 5mV for 0V gate bias for 100mM HCl solution (top panel). Current traces for voltages 50mV, 55mV, 60mV, 65mV and 70mV (middle panel). Current trace for 70mV showing numerous Coulter events (bottom panel).
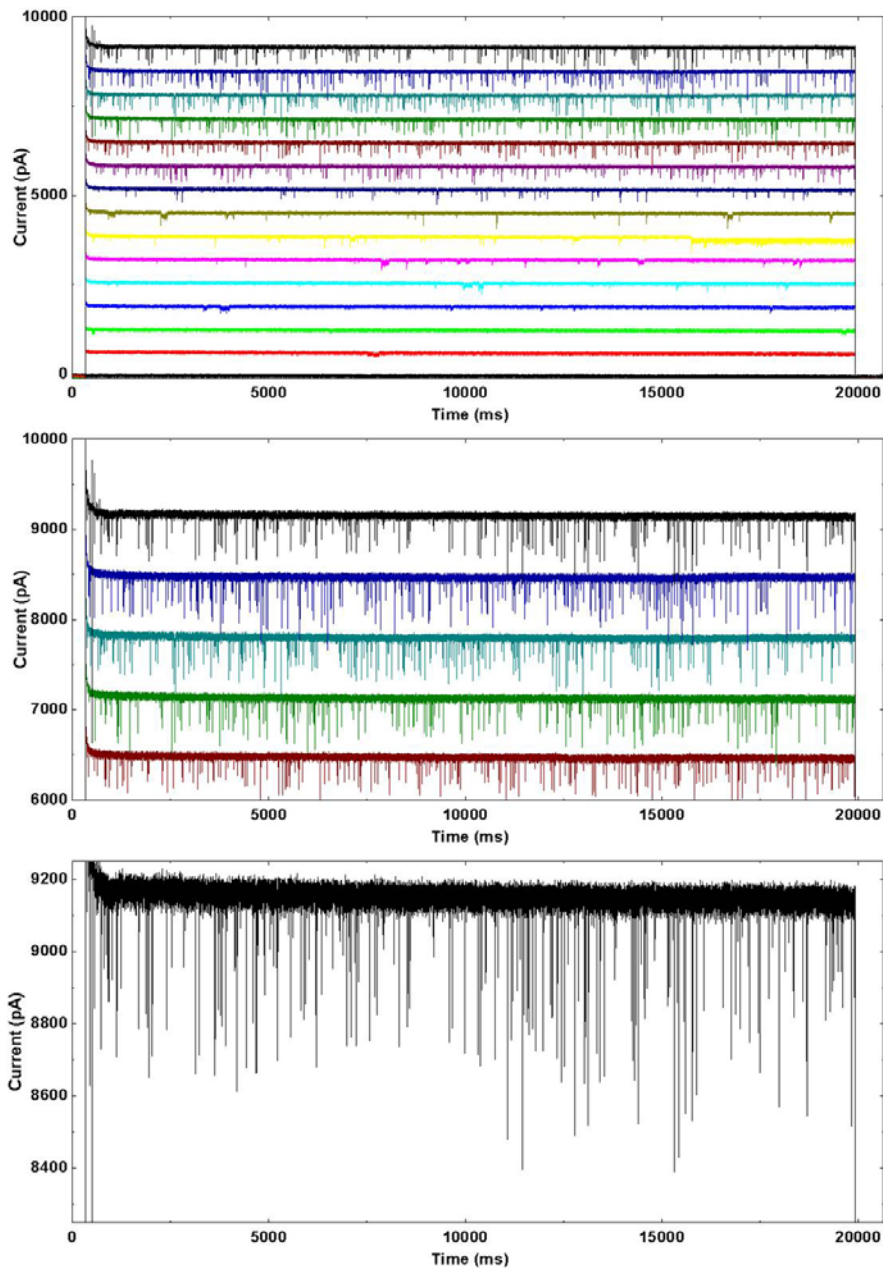
Figure 5.4 Complete voltage sweeps from 0mV-70mV at an increment of 5mV for 10V gate bias for 100mM HCl solution (top panel). Current traces for voltages 50mV, 55mV, 60mV, 65mV and 70mV (middle panel). Current trace for 70mV showing numerous Coulter events. Also, noticeable is the increase in the background peak-to-peak noise due to biasing the nanopore chip (bottom panel).

121

In order to understand the nature of translocation of polystyrene beads through a nanopopre, a single transition event from the current traces, Figure 5.3 (bottom panel) and Figure 5.4 (bottom panel), have been plotted in Figure 5.5.
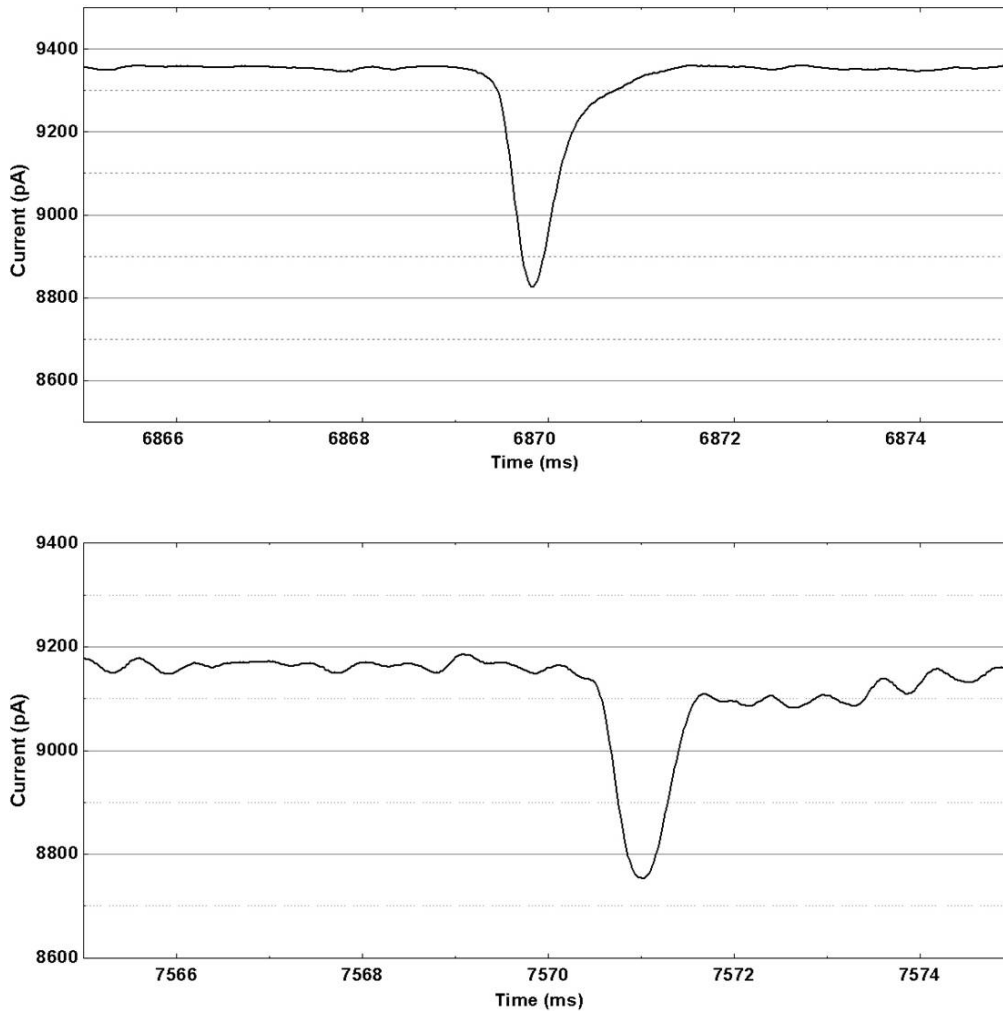
Figure 5.5 A single polystyrene bead translocation event at 0V gate bias (top panel) and 10V gate bias (bottom panel). The voltage applied across the nanopore in both the cases was 70mV.

The current stays at the baseline value until a bead passes through the pores. The passing of beads displaces the ionic liquid from the nanopores leading

122

to decrease in the measured current. The travelling of nanobeads through the nanopore is seen as a downward spike in the current trace. Once the beads have passed through the nanopore the measured current is back to its baseline value. This drop in current is then correlated with the diameter of the nanoparticle. The profile of the current drop dip resulting due to a bead translocation event was expected to be squarer in shape but instead it appears more triangular. The reason the dip has a triangular shape instead of a square one is because of the short duration of the bead translocation event. Another important feature to notice is the distinctive nature of the current spikes. The background noise on the current trace is 20pA peak-to-peak as measured by the low noise current amplifier and the current spikes generated by polystyrene beads passing through the nanopore create current spikes which are distinctive enough from the background noise.

As was the case with the experiments with 10mM HCl solutions the number of Coulter events for +10V bias is much greater than the number for 0V bias. In order to understand the effects of nanopore chip biasing or gate biasing as it is referred to the data from the current traces obtained at 0V and 10V was analyzed by our collaborators Mr. Prasanna Sattigeri and Dr. Andreas Spanias and the results of the data analysis is shown in Figure 5.6. The X-axis plots the value of the voltage applied across the nanopore. The Y-axis displays the number of Coulter events observed at a given applied across nanopore.
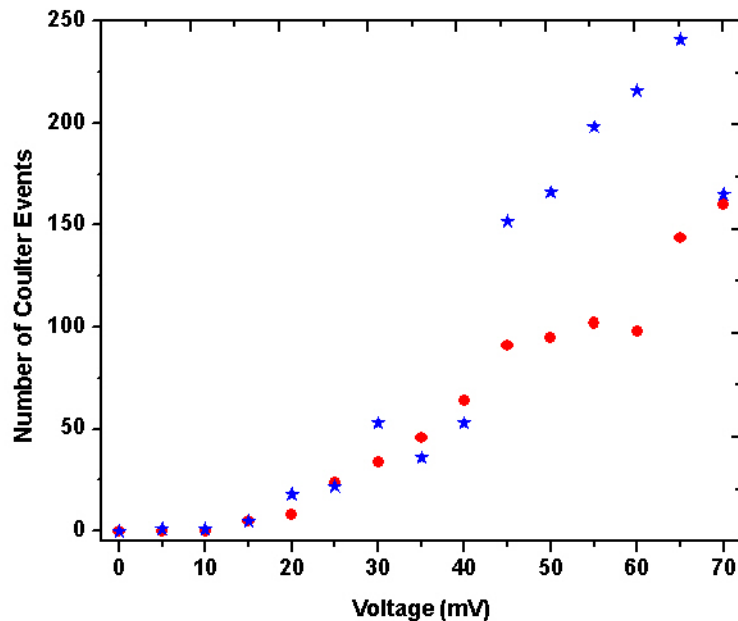
Figure 5.6 Coulter events as a function of voltage applied across the nanopore during a voltage sweep. A gate bias of +10V leads to a higher number of translocation events compared to a gate bias of 0V.

Figure 5.6 shows the number of Coulter events observed as the voltage applied across the nanopore is swept from 0mV to 70mV. At low voltages very few Coulter events are seen in the case of 0V (red circles) and 10V bias (blue stars). As the voltage applied across the nanopore is increased the number of particles going through the start to increase.

It is worthwhile to point out at this point of time that the polystyrene beads are negatively charged due to the –COO⁻ group. Therefore, when a positive bias is applied to the nanopore chip a large number of polystyrene beads come in the

vicinity of the nanopore which leads to an increase in the bead translocation events.

5.5 Conclusion

In this chapter a brief introduction to the principle of Coulter counting was given. A theory to describe the magnitudes of current spikes observed due to bead translocation events was also presented. In addition this, the results of Coulter counting experiments with 61nm mean diameter polystyrene beads using 105nm diameter single nanopore at different ionic concentrations are presented. Also, presented are the results of Coulter counting experiments with and without bias to the nanopore chip.

6.   CONCLUSION

Significant advances in nanofabrication technologies have led to the beginning of a new era where materials and structures are designed at a molecular level and then fabricated with control of composition and dimensions at molecular length scales. This drive to design, manipulate and build structures with dimensions in the molecular range has immensely contributed to advances in nanoscale analysis systems. Although, the direction of progress of nanoscale analysis systems or nanofluidic structures seems to follow the path of microelectronics, it differs in one important aspect from microelectronics that the fundamental physics in nanoscale analysis systems, changes more rapidly as the size scale is decreased. When a system is reduced in size the changes in length, area, and volume ratios alter, often in unexpected ways, the relative influence of various physical effects that determine the overall operation of a system. Independent of the type of driving force, the novel attributes of nanofluidic structures ensure ionic and molecular transport characteristics that are fundamentally different from those in larger micrometer and millimeter scale structures.

One such category of nanofluidic structures demonstrating unique ionic and molecular transport characteristics are nanopores. The characteristics of ionic and molecular transport often observed in nanopores are pronounced influence of surface charge density, coupled and enhanced mass and ion transport,

nanostructure size and shape, mobile phase ionic strength, large mass-to-charge ratio of ionic species in an ionic solution, ion depletion/enrichment, ion current rectification, and diminished background signals. These effects of these phenomena are much more pronounced when the nanopore dimensions are comparable to the Debye screening length of the ionic solution. These myriad phenomena, point to a simple fact that the molecular characteristics can dominate the ionic and molecular transport behavior of a nanostructure. Thus, these nanopores are an ideal platform to study electrolyte transport properties on the nanometer scale to control the ion transport by modulation of the surface potential, similar to the control mechanism present in field effect transistors. In addition to this nanopores have also emerged as one of the popular choices for detection, confinement, and transport of nanoscale analytes allowing an opportunity to study nanometer level interactions which are typically lost in bulk measurement methods.

This doctoral study made an attempt to understand and influence the ion transport through the nanopores fabricated in silicon-on-insulator substrate using standard clean room fabrication techniques. The fabrication process flow developed in this research and presented in this research presents a novel approach compared to all other prevalent processes in the research field. The fabrication of nanopores in silicon-on-insulator using electron beam lithography and dry etching processes allows fabrication of precise, reliable definition of

nanopores as well as an ordered array of nanopores. The process flow is compatible with standard cleanroom facilities for a high throughput fabrication of single as well as an array of nanopores. The process flow also permits precise dimensional as well as process control.

The ion transport measurements through the silicon-on-insulator nanopores displayed a significant change due to the effects of the nanopore surface charge interaction with the ion transport as the ionic concentration of the solution is gradually decreased. On one end of the observed nanopore conductance phenomena is the complete non charge selective behavior of the nanopores due to a negligible electric double layer with zero surface charge and zeta potential, when filled with high ionic strength solutions. On the other hand is the behavior displayed of unipolar ionic conductors, meaning that the ionic current through the nanopores is predominantly due to counterions, with extended electric double layer overlap, leading to high values of surface charge and zeta potential, when filled with low ionic strength solutions. The electric double layer overlap within nanopores also results in the presence of electric potential from the nanopore surface, over the whole of the nanopore cross-section, allowing the possibility of modulating the surface potential by applying a voltage bias to the nanopore substrate, in a fashion similar to a semiconductor field effect transistor. In a microfluidics channel, in comparison to the nanopores, the electric double layer with counterionic mobile charge is confined to a very thin layer at the

surface, so that the fluid within a microfluidic channel is quasi-electroneutral. Hence, most of the fluid flowing through a microfluidics channel is charge non-selective and does not discriminate between charge transport of counterions and coions.

The above phenomenon was used in manipulating the ion transport by field effect modulation. A positive bias applied to the nanopore SOI layer, at low electrolyte concentrations, effectively decreased the ionic current. Likewise, a negative substrate bias increased the pore conductance significantly. A +10 V bias reduces the conductance at low HCl concentration by a factor of two while the conductance can be increased by a factor of 2-3x with just a -1V bias.

Single nanopores were then used to demonstrate Coulter counting at nanometer scale using polystyrene beads at different ionic solution concentrations. Also, the effects of biasing the nanopore chip on Coulter counting were also presented.

6.1 Future Work

Nanopores offer a multitude of possibilities and applications and so does the fundamental physics at the nanometer level. One such study which could employ effective use of nanopores is the interaction of electrical double layers with nanopores of different surfaces. Also, to explore further application of field effect

modulation gold or platinum electrodes can be embedded within the nanopore structure.

An on growing field of application for nanopores is the passing of DNA molecules for DNA sequencing. Most of the nanopores which are used for DNA studies are not fabricated using standard cleanroom technologies and hence lack the potential of mass fabrication. Silicon-on-insulator nanopores can fill that gap.

In the end, nanopore research has a bright future!

REFERENCES

[1]   B. J. Kirby and E. F. Hasselbrink, "Zeta potential of microfluidic substrates: 1. Theory, experimental techniques, and effects on separations," *Electrophoresis,* vol. 25, pp. 187-202, Jan 2004.

[2]   R. Fan, S. Huh, R. Yan, J. Arnold, and P. D. Yang, "Gated proton transport in aligned mesoporous silica films," *Nature Materials,* vol. 7, pp. 303-307, Mar 2008.

[3]   D. C. Grahame, "The Electrical Double Layer and the Theory of Electrocapillarity.," *Chem. Rev.,* vol. 41, pp. 441-501, 1947.

[4]   A. Holtzel and U. Tallarek, "Ionic conductance of nanopores in microscale analysis systems: Where microfluldics meets nanofluidics," *Journal of Separation Science,* vol. 30, pp. 1398-1419, Jul 2007.

[5]   R. B. Schoch, J. Y. Han, and P. Renaud, "Transport phenomena in nanofluidics," *Reviews of Modern Physics,* vol. 80, pp. 839-883, Jul-Sep 2008.

[6]   J. Y. Jung, P. Joshi, L. Petrossian, T. J. Thornton, and J. D. Posner, "Electromigration Current Rectification in a Cylindrical Nanopore Due to Asymmetric Concentration Polarization," *Analytical Chemistry,* vol. 81, pp. 3128-3133, 2009.

[7]   R. Karnik, K. Castelino, R. Fan, P. Yang, and A. Majumdar, "Effects of biological reactions and modifications on conductance of nanofluidic channels," *Nano Letters,* vol. 5, pp. 1638-1642, Sep 2005.

[8]   R. Karnik, K. Castelino, and A. Majumdar, "Field-effect control of protein transport in a nanofluidic transistor circuit," *Applied Physics Letters,* vol. 88, p. 12311, 2006.

[9]   R. Karnik, R. Fan, M. Yue, D. Y. Li, P. D. Yang, and A. Majumdar, "Electrostatic control of ions and molecules in nanofluidic transistors," *Nano Letters,* vol. 5, pp. 943-948, 2005.

[10]   C. R. Martin, M. Nishizawa, K. Jirage, and M. Kang, "Investigations of the transport properties of gold nanotubule membranes," *Journal of Physical Chemistry B,* vol. 105, pp. 1925-1934, Mar 2001.

[11] S. Pennathur and J. G. Santiago, "Electrokinetic transport in nanochannels. 1. Theory," *Analytical Chemistry,* vol. 77, pp. 6772-6781, Nov 1 2005.

[12] S. Pennathur and J. G. Santiago, "Electrokinetic transport in nanochannels. 2. Experiments," *Analytical Chemistry,* vol. 77, pp. 6782-6789, Nov 1 2005.

[13] A. Plecis, R. B. Schoch, and P. Renaud, "Ionic transport phenomena in nanofluidics: Experimental and theoretical study of the exclusion-enrichment effect on a chip," *Nano Letters,* vol. 5, pp. 1147-1155, Jun 2005.

[14] S. Prakash, A. Piruska, E. N. Gatimu, P. W. Bohn, J. V. Sweedler, and M. A. Shannon, "Nanofluidics: Systems and applications," *Ieee Sensors Journal,* vol. 8, pp. 441-450, May-Jun 2008.

[15] Q. S. Pu, J. S. Yun, H. Temkin, and S. R. Liu, "Ion-enrichment and ion-depletion effect of nanochannel structures," *Nano Letters,* vol. 4, pp. 1099-1103, 2004.

[16] R. B. Schoch and P. Renaud, "Ion transport through nanoslits dominated by the effective surface charge," *Applied Physics Letters,* vol. 86, Jun 20 2005.

[17] R. B. L. Schoch, Harald van; Renaud, Philippe, "Effects of surface charge on ion transport through nanoslits," *Physics of Fluids,* vol. 17, p. 100604, 2005.

[18] Z. S. Siwy, "Ion-current rectification in nanopores and nanotubes with broken symmetry," *Advanced Functional Materials,* vol. 16, pp. 735-746, Apr 4 2006.

[19] R. M. M. Smeets, U. F. Keyser, D. Krapf, M. Y. Wu, N. H. Dekker, and C. Dekker, "Salt dependence of ion transport and DNA translocation through solid-state nanopores," *Nano Letters,* vol. 6, pp. 89-95, Jan 2006.

[20] T. C. Kuo, D. M. Cannon, Y. N. Chen, J. J. Tulock, M. A. Shannon, J. V. Sweedler, and P. W. Bohn, "Gateable nanofluidic interconnects for multilayered microfluidic separation systems," *Analytical Chemistry,* vol. 75, pp. 1861-1867, Apr 15 2003.

[21]   P. W. Bohn, "Nanoscale Control and Manipulation of Molecular Transport in Chemical Analysis," *Annual Review of Analytical Chemistry,* vol. 2, pp. 279-296, 2009.

[22]   L. Petrossian, S. J. Wilk, P. Joshi, S. Hihath, S. M. Goodnick, and T. J. Thornton, "Fabrication of Cylindrical Nanopores and Nanopore Arrays in Silicon-On-Insulator Substrates," *Journal of Microelectromechanical Systems,* vol. 16, p. 1419, 2007.

[23]   L. Petrossian, S. J. Wilk, P. Joshi, S. Hihath, J. D. Posner, S. M. Goodnick, and T. J. Thornton, "Demonstration of Coulter counting through a cylindrical solid state nanopore," *Solid State Electronics,* vol. 51, p. 1391, 2007.

[24]   M. Ali, P. Ramirez, S. Mafe, R. Neumann, and W. Ensinger, "A pH-Tunable Nanofluidic Diode with a Broad Range of Rectifying Properties," *Acs Nano,* vol. 3, pp. 603-608, Mar 2009.

[25]   H. Chang, F. Kosari, G. Andreadakis, M. A. Alam, G. Vasmatzis, and R. Bashir, "DNA-mediated fluctuations in ionic current through silicon oxide nanopore channels," *Nano Letters,* vol. 4, pp. 1551-1556, Aug 2004.

[26]   H. Chang, B. M. Venkatesan, S. M. Iqbal, G. Andreadakis, F. Kosari, G. Vasmatzis, D. Peroulis, and R. Bashir, "DNA counterion current and saturation examined by a MEMS-based solid state nanopore sensor," *Biomedical Microdevices,* vol. 8, pp. 263-269, Sep 2006.

[27]   P. Chen, J. J. Gu, E. Brandin, Y. R. Kim, Q. Wang, and D. Branton, "Probing single DNA molecule transport using fabricated nanopores," *Nano Letters,* vol. 4, pp. 2293-2298, Nov 2004.

[28]   J. H. Dai, T. Ito, L. Sun, and R. M. Crooks, "Electrokinetic trapping and concentration enrichment of DNA in a microfluidic channel," *Journal of the American Chemical Society,* vol. 125, pp. 13026-13027, Oct 29 2003.

[29]   H. Daiguji, Y. Oka, and K. Shirono, "Nanofluidic diode and bipolar transistor," *Nano Letters,* vol. 5, pp. 2274-2280, Nov 2005.

[30]   H. Daiguji, P. D. Yang, and A. Majumdar, "Ion transport in nanofluidic channels," *Nano Letters,* vol. 4, pp. 137-142, Jan 2004.

[31] R. Fan, S. Huh, R. Yan, J. Arnold, and P. Yang, "Gated proton transport in aligned mesoporous silica films," *Nature Materials,* vol. 7, pp. 303-307, April 2008 2008.

[32] R. Fan, R. Karnik, M. Yue, D. Y. Li, A. Majumdar, and P. D. Yang, "DNA translocation in inorganic nanotubes," *Nano Letters,* vol. 5, pp. 1633-1637, Sep 2005.

[33] S. A. Gajar and M. W. Geis, "An Ionic Liquid-Channel Field-Effect Transistor," *Journal of the Electrochemical Society,* vol. 139, pp. 2833-2840, Oct 1992.

[34] J. Goldberger, R. Fan, and P. Yang, "Inorganic Nanotubes: A Novel Platform for Nanofluidics," *Accounts of Chemical Research,* vol. 39, pp. 239-248, 2006.

[35] C. Ho, R. Qiao, J. B. Heng, A. Chatterjee, R. J. Timp, N. R. Aluru, and G. Timp, "Electrolytic transport through a synthetic nanometer-diameter pore," *Proceedings of the National Academy of Sciences of the United States of America,* vol. 102, pp. 10445-10450, Jul 26 2005.

[36] D. Huh, K. L. Mills, X. Y. Zhu, M. A. Burns, M. D. Thouless, and S. Takayama, "Tuneable elastomeric nanochannels for nanofluidic manipulation," *Nature Materials,* vol. 6, pp. 424-428, Jun 2007.

[37] E. B. Kalman, I. Vlassiouk, and Z. S. Siwy, "Nanofluidic bipolar transistors," *Advanced Materials,* vol. 20, pp. 293-+, Jan 18 2008.

[38] M. L. Kovarik and S. C. Jacobson, "Nanofluidics in Lab-on-a-Chip Devices," *Analytical Chemistry,* vol. 81, pp. 7133-7140, Sep 1 2009.

[39] S. B. Lee and C. R. Martin, "Controlling the transport properties of gold nanotubule membranes using chemisorbed thiols," *Chemistry of Materials,* vol. 13, pp. 3236-3244, Oct 2001.

[40] B. Schiedt, K. Healy, A. P. Morrison, R. Neumann, and Z. Siwy, "Transport of ions and biomolecules through single asymmetric nanopores in polymer films," *Nuclear Instruments & Methods in Physics Research Section B-Beam Interactions with Materials and Atoms,* vol. 236, pp. 109-116, Jul 2005.

[41] G. F. Schneider, S. W. Kowalczyk, V. E. Calado, G. Pandraud, H. W. Zandbergen, L. M. K. Vandersypen, and C. Dekker, "DNA Translocation

through Graphene Nanopores," *Nano Letters,* vol. 10, pp. 3163-3167, Aug 2010.

[42]   Z. Siwy, P. Apel, D. Dobrev, R. Neumann, R. Spohr, C. Trautmann, and K. Voss, "Ion transport through asymmetric nanopores prepared by ion track etching," *Nuclear Instruments & Methods in Physics Research Section B-Beam Interactions with Materials and Atoms,* vol. 208, pp. 143-148, Aug 2003.

[43]   Z. Siwy, I. D. Kosinska, A. Fulinski, and C. R. Martin, "Asymmetric diffusion through synthetic nanopores," *Physical Review Letters,* vol. 94, Feb 4 2005.

[44]   D. Stein, M. Kruithof, and C. Dekker, "Surface-charge-governed ion transport in nanofluidic channels," *Physical Review Letters,* vol. 93, Jul 16 2004.

[45]   P. Joshi, A. Smolyanitsky, L. Petrossian, M. Goryll, M. Saraniti, and T. J. Thornton, "Field effect modulation of ionic conductance of cylindrical silicon-on-insulator nanopore array," *Journal of Applied Physics,* vol. 107, p. 6, Mar 2010.

[46]   E. B. Kalman, O. Sudre, I. Vlassiouk, and Z. S. Siwy, "Control of ionic transport through gated single conical nanopores," *Analytical and Bioanalytical Chemistry,* vol. 394, pp. 413-419, May 2009.

[47]   P. J. Kemery, J. K. Steehler, and P. W. Bohn, "Electric field mediated transport in nanometer diameter channels," *Langmuir,* vol. 14, pp. 2884-2889, May 12 1998.

[48]   T. C. Kuo, L. A. Sloan, J. V. Sweedler, and P. W. Bohn, "Manipulating molecular transport through nanoporous membranes by control of electrokinetic flow: Effect of surface charge density and debye length," *Langmuir,* vol. 17, pp. 6298-6303, Oct 2 2001.

[49]   S. W. Nam, M. J. Rooks, K. B. Kim, and S. M. Rossnagel, "Ionic Field Effect Transistors with Sub-10 nm Multiple Nanopores," *Nano Letters,* vol. 9, pp. 2044-2048, May 2009.

[50]   M. Nishizawa, V. P. Menon, and C. R. Martin, "Metal Nanotubule Membranes with Electrochemically Switchable Ion-Transport Selectivity," *Science,* vol. 268, pp. 700-702, May 1995.

[51]   J. Vidal, M. E. Gracheva, and J. P. Leburton, "Electrically tunable solid-state silicon nanopore ion filter," *Nanoscale Research Letters,* vol. 2, pp. 61-68, Feb 2007.

[52]   I. Vlassiouk and Z. S. Siwy, "Nanofluidic diode," *Nano Letters,* vol. 7, pp. 552-556, Mar 2007.

[53]   G. L. Wang, B. Zhang, J. R. Wayment, J. M. Harris, and H. S. White, "Electrostatic-gated transport in chemically modified glass nanopore electrodes," *Journal of the American Chemical Society,* vol. 128, pp. 7679-7686, Jun 14 2006.

[54]   Y. Zhang, T. C. Gamble, A. Neumann, G. P. Lopez, S. R. J. Brueck, and D. N. Petsev, "Electric field control and analyte transport in Si/SiO2 fluidic nanochannels," *Lab on a Chip,* vol. 8, pp. 1671-1675, 2008.

[55]   W. H. Coulter, "Means for Counting Particles Suspended in a Fluid," U.S. Patent Number 2656508, 1953.

[56]   H. Bayley, O. Braha, and L. Q. Gu, "Stochastic sensing with protein pores," *Advanced Materials,* vol. 12, pp. 139-142, Jan 20 2000.

[57]   H. Bayley and P. S. Cremer, "Stochastic sensors inspired by biology," *Nature,* vol. 413, pp. 226-230, Sep 13 2001.

[58]   H. Bayley and L. Jayasinghe, "Functional engineered channels and pores - (Review)," *Molecular Membrane Biology,* vol. 21, pp. 209-220, Jul 2004.

[59]   H. Bayley and C. R. Martin, "Resistive-pulse sensing - From microbes to molecules," *Chemical Reviews,* vol. 100, pp. 2575-2594, Jul 2000.

[60]   S. M. Bezrukov, "Ion channels as molecular Coulter counters to probe metabolite transport," *Journal of Membrane Biology,* vol. 174, pp. 1-13, Mar 1 2000.

[61]   S. M. Bezrukov, I. Vodyanoy, and V. A. Parsegian, "Counting Polymers Moving through a Single-Ion Channel," *Nature,* vol. 370, pp. 279-281, Jul 28 1994.

[62]   R. DeBlois, Mayyasi, SA, Schidlov, G, Wesley, R, Wolff, JS, "Virus Counting and Analysis by Resistive Pulse (Coulter Counter) Technique," *PROCEEDINGS OF THE AMERICAN ASSOCIATION FOR CANCER RESEARCH* vol. 15, pp. 104-104, 1974.

[63]   R. W. Deblois and C. P. Bean, "Counting and Sizing of Submicron
         Particles by Resistive Pulse Technique," *Review of Scientific Instruments,*
         vol. 41, pp. 909-&, 1970.

[64]   R. W. Deblois, C. P. Bean, and R. K. A. Wesley, "Electrokinetic
         Measurements with Submicron Particles and Pores by Resistive Pulse
         Technique," *Journal of Colloid and Interface Science,* vol. 61, pp. 323-
         335, 1977.

[65]   D. Fologea, M. Gershow, B. Ledden, D. S. McNabb, J. A. Golovchenko,
         and J. L. Li, "Detecting single stranded DNA with a solid state nanopore,"
         Nano Letters, vol. 5, pp. 1905-1909, Oct 2005.

[66]   A. P. Han, G. Schurmann, G. Mondin, R. A. Bitterli, N. G. Hegelbach, N.
         F. de Rooij, and U. Staufer, "Sensing protein molecules using
         nanofabricated pores," *Applied Physics Letters,* vol. 88, Feb 27 2006.

[67]   J. Y. Han, J. P. Fu, and R. B. Schoch, "Molecular sieving using
         nanofilters: Past, present and future," *Lab on a Chip,* vol. 8, pp. 23-33,
         2008.

[68]   E. A. Heins, Z. S. Siwy, L. A. Baker, and C. R. Martin, "Detecting single
         porphyrin molecules in a conically shaped synthetic nanopore," *Nano
         Letters,* vol. 5, pp. 1824-1829, Sep 2005.

[69]   J. B. Heng, C. Ho, T. Kim, R. Timp, A. Aksimentiev, Y. V. Grinkova, S.
         Sligar, K. Schulten, and G. Timp, "Sizing DNA using a nanometer-
         diameter pore," *Biophysical Journal,* vol. 87, pp. 2905-2911, Oct 2004.

[70]   R. R. Henriquez, T. Ito, L. Sun, and R. M. Crooks, "The resurgence of
         Coulter counting for analyzing nanoscale objects," *Analyst,* vol. 129, pp.
         478-482, 2004.

[71]   C. Ho, J. Heng, G. Timp, and S. G. Sligar, "Biosensing in a functional
         nanoscale device: Protein tranlocation through nanometer-diameter pores,"
         Abstracts of Papers of the American Chemical Society, vol. 229, pp.
         U141-U141, Mar 13 2005.

[72]   T. Ito, L. Sun, and R. M. Crooks, "Observation of DNA transport through
         a single carbon nanotube channel using fluorescence microscopy,"
         Chemical Communications, pp. 1482-1483, 2003.

[73]   T. Ito, L. Sun, R. R. Henriquez, and R. M. Crooks, "A carbon nanotube-based Coulter nanoparticle counter," *Accounts of Chemical Research,* vol. 37, pp. 937-945, Dec 2004.

[74]   J. J. Kasianowicz, "Nanopores - Flossing with DNA," *Nature Materials,* vol. 3, pp. 355-356, Jun 2004.

[75]   A. Meller, L. Nivon, E. Brandin, J. Golovchenko, and D. Branton, "Rapid nanopore discrimination between single polynucleotide molecules," *Proceedings of the National Academy of Sciences of the United States of America,* vol. 97, pp. 1079-1084, Feb 2000.

[76]   C. A. Merchant, K. Healy, M. Wanunu, V. Ray, N. Peterman, J. Bartel, M. D. Fischbein, K. Venta, Z. T. Luo, A. T. C. Johnson, and M. Drndic, "DNA Translocation through Graphene Nanopores," *Nano Letters,* vol. 10, pp. 2915-2921, Aug 2010.

[77]   J. J. Nakane, M. Akeson, and A. Marziali, "Nanopore sensors for nucleic acid analysis," *Journal of Physics-Condensed Matter,* vol. 15, pp. R1365-R1393, Aug 2003.

[78]   J. P. Novak, E. S. Snow, E. J. Houser, D. Park, J. L. Stepowski, and R. A. McGill, "Nerve Agent Detection Using Networks of Single-Walled Carbon Nanotubes," *Applied Physics Letters,* vol. 83, pp. 4026-4028, 2003.

[79]   M. Rhee and M. A. Burns, "Nanopore sequencing technology: research trends and applications," *Trends in Biotechnology,* vol. 24, pp. 580-586, Dec 2006.

[80]   Y. H. Sen and R. Karnik, "Investigating the translocation of lambda-DNA molecules through PDMS nanopores," *Analytical and Bioanalytical Chemistry,* vol. 394, pp. 437-446, May 2009.

[81]   E. M. Nestorovich, C. Danelon, M. Winterhalter, and S. M. Bezrukov, "Designed to penetrate: Time-resolved interaction of single antibiotic molecules with bacterial pores," *Proceedings of the National Academy of Sciences of the United States of America,* vol. 99, pp. 9789-9794, Jul 23 2002.

[82]   E. M. Nestorovich, T. K. Rostovtseva, and S. M. Bezrukov, "Residue ionization and ion transport through OmpF channels," *Biophysical Journal,* vol. 85, pp. 3718-3729, Dec 2003.

[83]   T. K. Rostovtseva, A. Komarov, S. M. Bezrukov, and M. Colombini, "Dynamics of Nucleotides in VDAC channels: Structure-specific noise generation," *Biophysical Journal,* vol. 82, pp. 193-205, Jan 2002.

[84]   T. K. Rostovtseva, E. M. Nestorovich, and S. M. Bezrukov, "Partitioning of differently sized poly(ethylene glycol)s into OmpF porin," *Biophysical Journal,* vol. 82, pp. 160-169, Jan 2002.

[85]   I. Szabo, G. Bathori, F. Tombola, M. Brini, A. Coppola, and M. Zoratti, "DNA translocation across planar bilayers containing Bacillus subtilis ion channels," *Journal of Biological Chemistry,* vol. 272, pp. 25275-25282, Oct 1997.

[86]   I. Szabo, G. Bathori, F. Tombola, A. Coppola, I. Schmehl, M. Brini, A. Ghazi, V. De Pinto, and M. Zoratti, "Double-stranded DNA can be translocated across a planar membrane containing purified mitochondrial porin," *Faseb Journal,* vol. 12, pp. 495-502, Apr 1998.

[87]   D. Mijatovic, J. C. T. Eijkel, and A. van den Berg, "Technologies for nanofluidic systems: top-down vs. bottom-up - a review," *Lab on a Chip,* vol. 5, pp. 492-500, 2005.

[88]   P. Abgrall and N. T. Nguyen, "Nanofluidic devices and their applications," *Analytical Chemistry,* vol. 80, pp. 2326-2341, Apr 1 2008.

[89]   C. Dekker, "Solid-state nanopores," *Nature Nanotechnology,* vol. 2, pp. 209-215, Apr 2007.

[90]   J. J. Kasianowicz, E. Brandin, D. Branton, and D. W. Deamer, "Characterization of individual polynucleotide molecules using a membrane channel," *Proceedings of the National Academy of Sciences of the United States of America,* vol. 93, pp. 13770-13773, Nov 1996.

[91]   T. Schenkel, V. Radmilovic, E. A. Stach, S. J. Park, and A. Persaud, "Formation of a few nanometer wide holes in membranes with a dual beam focused ion beam system," *Journal of Vacuum Science & Technology B,* vol. 21, pp. 2720-2723, Nov-Dec 2003.

[92]   J. M. Song, C. Midson, E. Blachly-Dyson, M. Forte, and M. Colombini, "The topology of VDAC as probed by biotin modification," *Journal of Biological Chemistry,* vol. 273, pp. 24406-24413, Sep 1998.

[93]   L. Z. Song, M. R. Hobaugh, C. Shustak, S. Cheley, H. Bayley, and J. E. Gouaux, "Structure of staphylococcal alpha-hemolysin, a heptameric transmembrane pore," *Science,* vol. 274, pp. 1859-1866, Dec 13 1996.

[94]   M. Akeson, D. Branton, J. J. Kasianowicz, E. Brandin, and D. W. Deamer, "Microsecond time-scale discrimination among polycytidylic acid, polyadenylic acid, and polyuridylic acid as homopolymers or as segments within single RNA molecules," *Biophysical Journal,* vol. 77, pp. 3227-3233, Dec 1999.

[95]   H. Wang, J. E. Dunning, A. P. H. Huang, J. A. Nyamwanda, and D. Branton, "DNA heterogeneity and phosphorylation unveiled by single-molecule electrophoresis," *Proceedings of the National Academy of Sciences of the United States of America,* vol. 101, pp. 13472-13477, Sep 2004.

[96]   Y. Astier, O. Braha, and H. Bayley, "Toward single molecule DNA sequencing: Direct identification of ribonucleoside and deoxyribonucleoside 5 '-monophosphates by using an engineered protein nanopore equipped with a molecular adapter," *Journal of the American Chemical Society,* vol. 128, pp. 1705-1710, Feb 2006.

[97]   S. Howorka, S. Cheley, and H. Bayley, "Sequence-specific detection of individual DNA strands using engineered nanopores," *Nature Biotechnology,* vol. 19, pp. 636-639, Jul 2001.

[98]   J. Sanchez-Quesada, A. Saghatelian, S. Cheley, H. Bayley, and M. R. Ghadiri, "Single DNA rotaxanes of a transmembrane pore protein," *Angewandte Chemie-International Edition,* vol. 43, pp. 3063-3067, 2004.

[99]   J. L. Li, M. Gershow, D. Stein, E. Brandin, and J. A. Golovchenko, "DNA molecules and configurations in a solid-state nanopore microscope," *Nature Materials,* vol. 2, pp. 611-615, Sep 2003.

[100]   D. Fologea, J. Uplinger, B. Thomas, D. S. McNabb, and J. L. Li, "Slowing DNA translocation in a solid-state nanopore," *Nano Letters,* vol. 5, pp. 1734-1737, Sep 2005.

[101] R. M. M. Smeets, A. J. Storm, D. Krapf, U. F. Keyser, T. van der Heijden, N. H. Dekker, and C. Dekker, "Translocation of dsDNA structures through solid-state nanopores," *Biophysical Journal,* vol. 88, pp. 352A-352A, Jan 2005.

[102] A. J. Storm, J. H. Chen, X. S. Ling, H. W. Zandbergen, and C. Dekker, "Fabrication of solid-state nanopores with single-nanometre precision," *Nano Letters,* vol. 2, pp. 537-540, 2003.

[103] A. J. Storm, J. H. Chen, X. S. Ling, H. W. Zandbergen, and C. Dekker, "Electron-beam-induced deformations of SiO2 nanostructures," *Journal of Applied Physics,* vol. 98, Jul 2005.

[104] A. P. Han, N. F. de Rooij, and U. Staufer, "Design and fabrication of nanofluidic devices by surface micromachining," *Nanotechnology,* vol. 17, pp. 2498-2503, May 28 2006.

[105] O. A. Saleh and L. L. Sohn, "An artificial nanopore for molecular sensing," *Nano Letters,* vol. 3, pp. 37-38, Jan 2003.

[106] B. Hille, *Ion Channels of Excitable Membranes, Third Edition*: Sinauer Associates, Inc,, 2001.

[107] M. Mayer, J. K. Kriebel, M. T. Tosteson, and G. M. Whitesides, "Microfabricated Teflon Membranes for Low-Noise Recordings of Ion Channels in Planar Lipid Bilayers," *Biophysical Journal,* vol. 85, pp. 2684-2695, 2003.

[108] S. J. Wilk, M. Goryll, G. M. Laws, S. M. Goodnick, T. J. Thornton, M. Saraniti, J. Tang, and R. S. Eisenberg, "Teflon (TM)-coated silicon apertures for supported lipid bilayer membranes," *Applied Physics Letters,* vol. 85, pp. 3307-3309, Oct 11 2004.

[109] S. J. Wilk, L. Petrossian, M. Goryll, G. M. Laws, S. M. Goodnick, T. J. Thornton, J. Tang, and R. S. Eisenberg, "Integrated Platform for Ion Channel Sensing," in *IEEE Sensors 2005*, Irvine, CA, 2005.

[110] C. Danelon, M. Lindemann, C. Borin, D. Fournier, and M. Winterhalter, "Channel-forming membrane proteins as molecular sensors," *Ieee Transactions on Nanobioscience,* vol. 3, pp. 46-48, Mar 2004.

[111] J. Schmidt, "Stochastic sensors," *Journal of Materials Chemistry,* vol. 15, pp. 831-840, 2005.

[112] H. Wang and D. Branton, "Nanopores with a spark for single-molecule detection," *Nature Biotechnology,* vol. 19, pp. 622-623, Jul 2001.

[113] D. W. Deamer and D. Branton, "Characterization of nucleic acids by nanopore analysis," *Accounts of Chemical Research,* vol. 35, pp. 817-825, Oct 2002.

[114] J. B. Heng, A. Aksimentiev, C. Ho, P. Marks, Y. V. Grinkova, S. Sligar, K. Schulten, and G. Timp, "The electromechanics of DNA in a synthetic nanopore," *Biophysical Journal,* vol. 90, pp. 1098-1106, Feb 2006.

[115] H. Chang, S. M. Iqbal, E. A. Stach, A. H. King, N. J. Zaluzec, and R. Bashir, "Fabrication and characterization of solid-state nanopores using a field emission scanning electron microscope," *Applied Physics Letters,* vol. 88, Mar 6 2006.

[116] J. B. Heng, A. Aksimentiev, C. Ho, P. Marks, Y. V. Grinkova, S. Sligar, K. Schulten, and G. Timp, "Stretching DNA using the electric field in a synthetic nanopore," *Nano Letters,* vol. 5, pp. 1883-1888, Oct 2005.

[117] U. F. Keyser, B. N. Koeleman, S. Van Dorp, D. Krapf, R. M. M. Smeets, S. G. Lemay, N. H. Dekker, and C. Dekker, "Direct force measurements on DNA in a solid-state nanopore," *Nature Physics,* vol. 2, pp. 473-477, Jul 2006.

[118] U. F. Keyser, D. Krapf, B. N. Koeleman, R. M. M. Smeets, N. H. Dekker, and C. Dekker, "Nanopore tomography of a laser focus," *Nano Letters,* vol. 5, pp. 2253-2256, Nov 2005.

[119] Z. Siwy, P. Apel, D. Baur, D. D. Dobrev, Y. E. Korchev, R. Neumann, R. Spohr, C. Trautmann, and K. O. Voss, "Preparation of synthetic nanopores with transport properties analogous to biological channels," *Surface Science,* vol. 532, pp. 1061-1066, Jun 10 2003.

[120] Z. Siwy, D. Dobrev, R. Neumann, C. Trautmann, and K. Voss, "Electro-responsive asymmetric nanopores in polyimide with stable ion-current signal," *Applied Physics a-Materials Science & Processing,* vol. 76, pp. 781-785, Mar 2003.

[121] A. Mara, Z. Siwy, C. Trautmann, J. Wan, and F. Kamme, "An asymmetric polymer nanopore for single molecule detection," *Nano Letters,* vol. 4, pp. 497-501, Mar 2004.

[122] L. Sun and R. M. Crooks, "Single carbon nanotube membranes: A well-defined model for studying mass transport through nanoporous materials," *Journal of the American Chemical Society,* vol. 122, pp. 12340-12345, Dec 2000.

[123] B. Zhang, Y. H. Zhang, and H. S. White, "The nanopore electrode," *Analytical Chemistry,* vol. 76, pp. 6229-6238, Nov 2004.

[124] J. B. Heng, A. Aksimentiev, V. Dimitrov, Y. Grinkova, C. Ho, P. Marks, K. Schulten, S. Sligar, and G. Timp, "Stretching DNA using an artificial nanopore," *Biophysical Journal,* vol. 88, pp. 659A-659A, Jan 2005.

[125] J. Li, D. Stein, C. McMullan, D. Branton, M. J. Aziz, and J. A. Golovchenko, "Ion-beam sculpting at nanometre length scales," *Nature,* vol. 412, pp. 166-169, Jul 2001.

[126] D. M. Stein, C. J. McMullan, J. L. Li, and J. A. Golovchenko, "Feedback-controlled ion beam sculpting apparatus," *Review of Scientific Instruments,* vol. 75, pp. 900-905, Apr 2004.

[127] S. Garaj, W. Hubbard, A. Reina, J. Kong, D. Branton, and J. A. Golovchenko, "Graphene as a subnanometre trans-electrode membrane," *Nature,* vol. 467, pp. 190-U73, Sep 2010.

[128] M. L. Brongersma, E. Snoeks, T. van Dillen, and A. Polman, "Origin of MeV ion irradiation-induced stress changes in SiO2," *Journal of Applied Physics,* vol. 88, pp. 59-64, Jul 2000.

[129] T. Mitsui, D. Stein, Y. R. Kim, D. Hoogerheide, and J. A. Golovchenko, "Nanoscale volcanoes: Accretion of matter at ion-sculpted nanopores," *Physical Review Letters,* vol. 96, Jan 2006.

[130] M. B. Stern, M. W. Geis, and J. E. Curtin, "Nanochannel fabrication for chemical sensors," *Journal of Vacuum Science & Technology B,* vol. 15, pp. 2887-2891, Nov-Dec 1997.

[131] P. Chen, T. Mitsui, D. B. Farmer, J. Golovchenko, R. G. Gordon, and D. Branton, "Atomic layer deposition to fine-tune the surface properties and diameters of fabricated nanopores," *Nano Letters,* vol. 4, pp. 1333-1337, Jul 2004.

[132] R. G. Gordon, D. Hausmann, E. Kim, and J. Shepard, "A kinetic model for step coverage by atomic layer deposition in narrow holes or trenches," *Chemical Vapor Deposition,* vol. 9, pp. 73-78, Mar 2003.

[133] D. M. Hausmann, E. Kim, J. Becker, and R. G. Gordon, "Atomic layer deposition of hafnium and zirconium oxides using metal amide precursors," *Chemistry of Materials,* vol. 14, pp. 4350-4358, Oct 2002.

[134] D. Ho, B. Chu, J. J. Schmidt, E. K. Brooks, and C. D. Montemagno, "Hybrid protein-polymer biomimetic membranes," *Ieee Transactions on Nanotechnology,* vol. 3, pp. 256-263, Jun 2004.

[135] Z. Siwy and A. Fulinski, "Fabrication of a synthetic nanopore ion pump," *Physical Review Letters,* vol. 89, Nov 4 2002.

[136] Z. Siwy, E. Heins, C. C. Harrell, P. Kohli, and C. R. Martin, "Conical-nanotube ion-current rectifiers: The role of surface charge," *Journal of the American Chemical Society,* vol. 126, pp. 10850-10851, Sep 8 2004.

[137] H. Schmid and B. Michel, "Siloxane polymers for high-resolution, high-accuracy soft lithography," *Macromolecules,* vol. 33, pp. 3042-3049, Apr 2000.

[138] G. K. Celler and S. Cristoloveanu, "Frontiers of silicon-on-insulator," *Journal of Applied Physics,* vol. 93, 2003.

[139] R. F. Probstein, *Physicochemical Hydrodynamics*. Hoboken, New Jersey: John Wiley & Sons., 2003.

[140] A. A. Ayón, R. Braff, C. C. Lin, H. H. Sawin, and M. A. Schmidt, "Characterization of a Time Multiplexed Inductively Coupled Plasma Etcher," *Journal of The Electrochemical Society,* vol. 146, pp. 339-349, 1999.

[141] P. F. Man, B. P. Gogoi, and C. H. Mastrangelo, "Elimination of post-release adhesion in microstructures using conformal fluorocarbon coatings," *Journal of Microelectromechanical Systems,* vol. 6, pp. 25-34, Mar 1997.

[142] B. K. Smith, J. J. Sniegowski, G. LaVigne, and C. Brown, "Thin Teflon-like films for eliminating adhesion in released polysilicon micro structure," *Sensors and Actuators a-Physical,* vol. 70, pp. 159-163, Oct 1 1998.

[143] M. J. Madou, *Fundamentals of Microfabrication: The science of Miniaturization.* Boca raton, FL: CRC Press Ltd., 2002.

[144] J. H. Lee, G. Y. Yeom, J. W. Lee, and J. Y. Lee, "Study of shallow silicon trench etch process using planar inductively coupled plasmas," *Journal of Vacuum Science & Technology A,* vol. 15, pp. 573-578, May-Jun 1997.

[145] R. Sherman-Gold, *The Axon Guide for Electrophysiology and Biophysics: Laboratory Techniques*. Foster City, CA: Axon Instruments, 1993.

[146] V. Atanasov, N. Knorr, R. S. Duran, S. Ingebrandt, A. Offenhausser, W. Knoll, and I. Koper, "Membrane on a chip: A functional tethered lipid bilayer membrane on silicon oxide surfaces," *Biophysical Journal,* vol. 89, pp. 1780-1788, Sep 2005.

[147] M. A. Burns, B. N. Johnson, S. N. Brahmasandra, K. Handique, J. R. Webster, M. Krishnan, T. S. Sammarco, P. M. Man, D. Jones, D. Heldsinger, C. H. Mastrangelo, and D. T. Burke, "An integrated nanoliter DNA analysis device," *Science,* vol. 282, pp. 484-487, Oct 1998.

[148] A. M. Dupuy, S. Lehmann, and J. P. Cristol, "Protein biochip systems for the clinical laboratory," *Clinical Chemistry and Laboratory Medicine,* vol. 43, pp. 1291-1302, Dec 2005.

[149] A. Gadre, M. Kastantin, S. Li, and R. Ghodssi, "An Integrated {BioMEMS} Fabrication Technology," in *Internat. Semiconductor Device Research Symposium {(ISDRS)}*, 2001, pp. 1-4.

[150] M. Goryll, S. Wilk, G. M. Laws, T. Thornton, S. Goodnick, M. Saraniti, J. Tang, and R. S. Eisenberg, "Silicon-based ion channel sensor," *Superlattices and Microstructures,* vol. 34, pp. 451-457, Sep-Dec 2003.

[151] M. Goryll, S. Wilk, G. M. Laws, T. Thornton, S. Goodnick, M. Saraniti, J. Tang, and R. S. Eisenberg, "Integrated Sensor Design Using Ion Channels Inserted into Lipid Bilayer Membranes," in *Nanotechnology, 2004. 4th IEEE Conference on*, Munich, Germany, 2004, pp. 302-304.

[152] N. Malmstadt, M. A. Nash, R. F. Purnell, and J. J. Schmidt, "Automated formation of lipid-bilayer membranes in a microfluidic device," *Nano Letters,* vol. 6, pp. 1961-1965, Sep 13 2006.

[153] Y. Y. Peng, A. Pallandre, N. T. Tran, and M. Taverna, "Recent innovations in protein separation on microchips by electrophoretic methods," *Electrophoresis,* vol. 29, pp. 157-178, Jan 2008.

[154] T. Sata, *Ion Exchange Membranes: Preparation, Characterization, Modification, and Application* Royal Society of chemistry, 2004.

[155] H. Strathmann, *Ion-Exchange Membrane Separation Processes* vol. 9: Elsiever, 2004.

[156] S. H. Behrens and D. G. Grier, "The charge of glass and silica surfaces," *Journal of Chemical Physics,* vol. 115, pp. 6716-6721, Oct 8 2001.

[157] A. Smolyanitsky and M. Saraniti, "Silicon nanopores as bioelectronic devices: a simulation study," *Journal of Computational Electronics,* vol. 8, 2009.

[158] P. M. Dove and C. M. Craven, "Surface charge density on silica in alkali and alkaline earth chloride electrolyte solutions," *Geochimica Et Cosmochimica Acta,* vol. 69, pp. 4963-4970, Nov 2005.

[159] R. F. Pierret, *Semiconductor Device Fundamentals* Addison Wesley, 1996.

[160] D. Constantin and Z. S. Siwy, "Poisson-Nernst-Planck model of ion current rectification through a nanofluidic diode," *Physical Review E (Statistical, Nonlinear, and Soft Matter Physics),* vol. 76, p. 041202, 2007.

[161] D. R. Lide, *CRC Handbook of Chemistry and Physics*, 89th Edition ed., 2008.